2023

Probing Signal-Based Data-Driven Modeling of Power Electronics Smart Converter Dynamics Using Power Hardware-In-The-Loop

Nischal Guruwacharya

PROBING SIGNAL-BASED DATA-DRIVEN MODELING OF POWER ELECTRONICS SMART CONVERTER DYNAMICS USING POWER HARDWARE-IN-THE-LOOP

BY

NISCHAL GURUWACHARYA

A dissertation submitted in partial fulfillment of the requirements for the

Doctor of Philosophy

Major in Electrical Engineering

South Dakota State University

2023

DISSERTATION ACCEPTANCE PAGE
Nischal Guruwacharya

This dissertation is approved as a creditable and independent investigation by a candidate for the Doctor of Philosophy degree and is acceptable for meeting the dissertation requirements for this degree. Acceptance of this does not imply that the conclusions reached by the candidate are necessarily the conclusions of the major department.

Reinaldo Tonkoski
Advisor Date

George Hamer
Department Head Date

Nicole Lounsbery, PhD
Director, Graduate School Date

I dedicate this work to my grandmother, Krishna Kumari Guruwacharya, my father, Shyam Raj Guruwacharya, my late mother, Keshbadan Guruwacharya, my brother, Nirmal Guruwacharya, and my sisters, Parbati Amatya and Nisha Rajbhandari. None of this may have been possible without their love and invaluable moral support during my study and research.

"Coming together is a beginning; keeping together is progress; working together is success."

Edward Everett Hale

ACKNOWLEDGMENTS

I would like to express my sincere gratitude towards my research advisor Dr. Reinaldo Tonkoski for his continuous guidance and encouragement during my Ph.D. I would like to acknowledge him for conceptualizing and funding this work. This work would not be possible without his support, motivation, and enthusiasm. Besides my advisor, I would like to thank my committee members, Dr. Timothy M. Hansen and Dr. Robert Fourney, from South Dakota State University (SDSU), Dr. Marco Ciarcia from Colorado State University, Dr. Fabio Andrade from University of Puerto Rico at Mayagüez, and graduate faculty representative Dr. Hossien Moradi Rekabdarkolaee from SDSU for their participation and interest in my work.

During my Ph.D., I have been fortunate to have the support of all my peers and colleagues in the Electrical Engineering and Computer Science Department. I express special thanks to Niranjan Bhujel, Sunil Subedi, Manisha Rauniyar, and Ujjwol Tamrakar for their useful suggestions and assistance. I would like to thank all the graduate students who were present here during my courses for their help and support in providing constructive feedback on my work. I would also like to thank Mr. Dan Flaskey for all the initial help in setting up lab experiments throughout my Ph.D. program.

This work was supported by the U.S. Department of Energy (DoE) Office of Science (OoS), Office of Electricity Microgrid R&D Program, and Office of Energy Efficiency and Renewable Energy Solar Energy Technology Office under the EPSCoR grant number DE-SC0020281. This work made use of the Opal-RT real-time simulator purchased as part of the National Science Foundation (NSF) grant number MRI-1726964.

I would also like to acknowledge the Advanced Research Projects Agency-Energy (ARPA-E) for supporting data-driven grid-forming inverter research through the project titled “Rapidly Viable Sustained Grid” via grant no. DE-AR0001016. This work was authored in part by the National Renewable Energy Laboratory, managed and operated by Alliance for Sustainable Energy, LLC, for the U.S. Department of Energy (DOE) under Contract No. DE-AC36-08GO28308. I am thankful to National Renewable Energy Laboratories (NREL) for hosting me as an intern during my Ph.D. I am grateful to Dr. Govind Saraswat, Dr. Kumaraguru Prabakar, Er. Soham Chakraborty, Mr. Gregory Martin, Dr. Michael Blonsky, Dr. Rui Yang, Dr. Rob Hovsapian, Dr. Mayank Panwar, and Dr. Adarsh Nagarajan, for their help at NREL for completing this work.

CONTENTS

ABBREVIATIONS

CDPS	Converter-Dominated Power System
CVS	Controllable Voltage Source
DERs	Distributed Energy Resources
DPM	Dynamic Phasor Model
EMT	Electromagnetic Transient
EPS	Electric Power Systems
FPE	Final Prediction Error
FSI	Fronius Symo Inverter
GFL	Grid-following
GFM	Grid-forming
GoF	Goodness of fit
GSFs	Grid Support Functions
IBRs	Inverter-based Resources
IEEE	Institute of Electrical and Electronics Engineers
IP	Internet Protocol
IV	Instrument Variable
LVRT	Low Voltage Ride Through
NRMSE	Normalized Root-mean-square Error
PC	Personal Computer
PCC	Point of Common Coupling

PECs	Power Electronic Converters
PHIL	Power Hardware-in-the-loop
PLL	Phase-locked-loop
PSM	Positive-sequence Model
PV	Photovoltaic
PWM	Pulse Width Modulation
RTS	Real-time Simulator
SAS	Solar Array Simulator
SNR	Signal-to-noise ratio
SysId	System Identification
TCP	Transmission Control Protocol
TF	Transfer Function

LIST OF FIGURES

LIST OF TABLES

ABSTRACT

PROBING SIGNAL-BASED DATA-DRIVEN MODELING OF POWER ELECTRONICS SMART CONVERTER DYNAMICS USING POWER HARDWARE-IN-THE-LOOP

NISCHAL GURUWACHARYA

2023

The main objective of this dissertation is to develop a generalized simulation and modeling framework for extracting dynamics of power electronic converters (PECs) with grid support functions (GSFs) and validate model accuracy through experimental comparison with physical measurements. The dynamic models obtained from this modeling framework aim to facilitate accurate dynamic analysis of a highly integrated power system comprising inverter-based resources (IBRs), specifically for stability assessment. These dynamic models helped in reducing simulation time and computational complexity, thereby enhancing efficiency. Moreover, it provides valuable insights for utilities and grid operators involved in effective system planning, operation, and dispatch.

The dynamics of the current power grid are poised to undergo substantial changes due to the replacement of traditional generators and the integration of distributed energy resources (DERs) based on PECs equipped with advanced GSFs. The utilization of these smart PECs is expected to increase in the future, primarily because they conform to the voltage and frequency support requirements outlined in the Institute of Electrical and Electronics Engineers (IEEE) 1547-2018 standard. However, the dynamic behavior of PECs, particularly when providing various ancillary services, is attributed to the adoption

of modern control algorithms. Consequently, the system exhibits more stochastic and nonlinear dynamics, posing significant challenges to power system stability and control. Accurate modeling of these underlying nonlinear dynamics is required to ensure the stability and reliability of converter-dominated power system (CDPS). However, the proprietary nature and unknown parameters of the PECs control systems, coupled with the increasing system size, using a traditional modeling approach to obtain full dynamics becomes increasingly challenging and computationally expensive. Therefore, new modeling techniques are needed to accurately extract the PECs dynamics.

This dissertation presents a data-driven modeling technique to obtain the dynamics of PECs as it does not require detail knowledge of PECs physical topology, the complex models of the various voltage/current control loops, the models of the phase-locked-loop (PLL), the protection-scheme employed, etc. Data-driven modeling is an approach that constructs models based on data rather than predefined equations or theoretical assumptions. The underlying theory behind data-driven modeling is rooted in the idea that the data itself contains valuable information about the system or process being modeled. It involves data collection (time domain input-output data) and dataset is then divided into training and testing datasets. The training dataset is passed into a system identification (SysId) algorithm which uses Instrument Variable (IV) method to process the training dataset such that least-square error is minimized for each data point and estimates the parameters. From the estimated parameters, a transfer function (TF) is obtained. The testing dataset is then used to validate the TF obtained. Finally, GoF based on normalized root-mean-square error (NRMSE) is calculated to check the accuracy of the TF.

In data-driven modeling, it is essential to excite PECs with well-designed probing

signals, as they serve as input data during SysId and allow a deeper understanding of system behavior. However, it is imperative to adhere to design constraints set by both power system requirements and SysId theory before using any signal as a probing signal, ensuring its alignment with the desired frequency band. Considering potential variations in system time constants, square and rectangle signals are highly suitable for accurate time constant estimation and effective emphasis on specific frequency ranges based on signal frequency. Square and rectangle signals are non-sinusoidal periodic waveforms characterized by alternating amplitudes between defined minimum and maximum values at a constant frequency. Based on this, four different probing signals (i.e., logarithmic square-chirp, square, sine, and logarithmic sine-chirp) are used and the results show that the logarithmic square-chirp probing signal adequately excites the PECs to fit a data-driven dynamic model, achieving a goodness-of-fit (GoF) exceeding 90%.

Data-driven modeling techniques have also emerged as valuable tools for capturing the dynamic behavior of advanced control strategies for grid-forming inverters (GFM). This dissertation further investigates the application of a data-driven dynamic modeling technique for a GFM inverter using Power Hardware-in-the-Loop (PHIL) experiments to generate the data required. SysID is then used on collected data to obtain the dynamic model of GFM inverter. The effectiveness of the data-driven models is cross-validated with the model obtained from the analytical approach. GoF for analytical approach and data-driven approach are calculated to be 87.45% and 86.35%. Hence, both approaches are shown to accurately capture the dynamic response of GFM inverters under different loading conditions.

CHAPTER 1 Introduction

1.1 Background

The generation profile of power systems is undergoing a fundamental shift towards converter-based resources and reductions in large synchronous generation. Since it has become clear that intermittent renewable energy sources will be responsible for a large amount of power generation, the existing methods for power systems reliability assessments will need to be modernized to account for the dynamics of wind, solar, storage, and other grid edge devices [1]. This shift introduces modeling challenges for traditional transient planning and operation and reliability practices [2], [3]. These modeling challenges include the need for electromagnetic transient (EMT) simulations and accurate PEC models appropriate for the application of interest. Traditionally, positive-sequence simulators and phasor-based models of devices were adequate for assessing transient stability issues due to the dominance of synchronous generation. In systems with increasing and/or dominating amounts of converter-based generation, numerous stability issues arise that can only be accurately captured with EMT models and simulation [4], [5]. Additionally, numerous types of EMT models exist, each appropriate for specific stability issues. Examples of specific stability issues which become present in CDPS, where converter-based generation exists at both distribution and transmission levels, includes but is not limited to: a high rate of change of frequency due to low inertia [2], [6], [7], limited fault current contribution impacting protection coordination [2], [8]–[10], bi-directional power flow impacting damping of inter-area modes and transient stability margins [11]–[13], harmonic instability due to converter inner control loops [13],

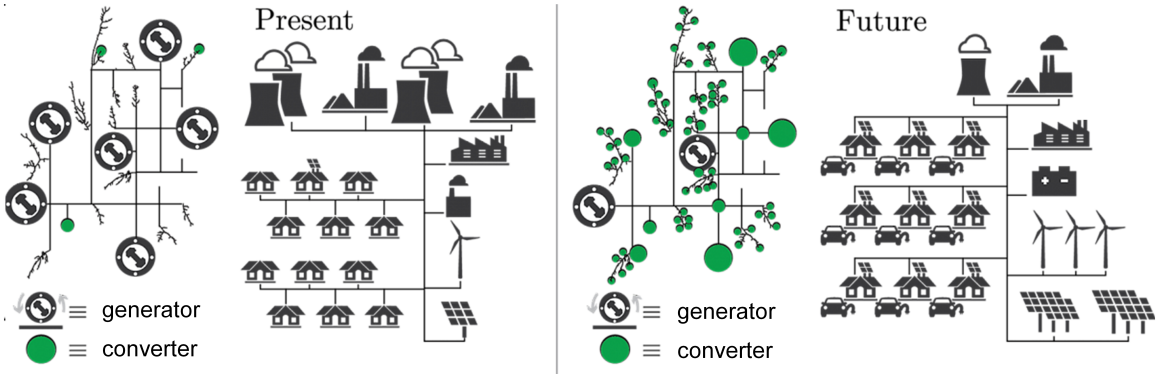

Figure 1.1. The transition from a traditional power system dominated by synchronous generators to a CDPS [19].

[14], interactions between multiple grid-connected converters [13], [15], [16], and lower frequency oscillations introduced by the phase-locked-loop (PLL) , particularly in weak grids with short circuit ratios less than 2 [13], [17]. An excellent review of these converter-based generation stability issues is provided in [2], [13], [14], [18].

In response to the growing electric demand, a significant amount of inverter-based generation, including PV , wind, and energy storage systems, is being integrated into the bulk electric power grid. These distributed energy resources (DERs) equipped with inverters play a vital role in supporting the voltage and frequency control of the power system. As the integration of inverter-based generation increases in the modern grid, it becomes crucial to accurately assess power system dynamics due to their distinct characteristics compared to traditional generation. This is particularly important when these resources also provide voltage and frequency support to the grid. The Institute of Electrical and Electronics Engineers (IEEE) 1547-2018 standard, for instance, recommends that DERs offer grid support functions (GSFs). These GSFs encompass various services, such as volt-watt, volt-var, frequency-watt, voltage or frequency

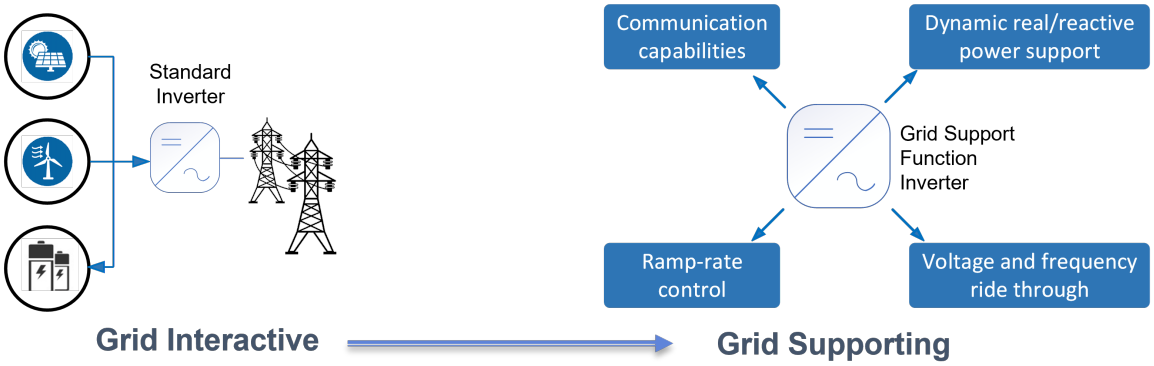

Figure 1.2. Transitioning PEC from Grid Interactive to Grid Supporting Control Strategies.

ride-through, communication capabilities, and ramp-rate control. To ensure the efficient and reliable operation of the modern grid with the integration of inverter-based generation, it is essential to employ accurate models that capture the dynamics and capabilities of these resources. By doing so, we can maximize the benefits and potential of renewable energy sources while maintaining grid stability.

In the past, a significant number of transmission system failures have caused substantial losses of Photovoltaic (PV) resources, leading to stability and reliability concerns for the PECs. One example of such an event was the “South Australia Blackout” [20]. The South Australia blackout of 2016 was a major power outage that affected the entire state of South Australia. Approximately 1.7 million people were affected by the outage, including households, businesses, and critical infrastructure. The blackout was triggered by a severe storm that hit South Australia. Severe storm damages the transmission and distribution assets resulting voltage disturbances. Moreover, the blackout was exacerbated by inadequate modeling and simulation of wind farms and their PECs. These PECs were sensitive to variations in grid voltage, activating low voltage ride through (LVRT) protection scheme which ultimately contributed to the disruption of

power supply. The LVRT protection scheme was set to withstand a pre-set number of voltage dips within a two-minute period.

Another event is Canyon 2 fire [21] which started on October 9, 2017. The Canyon 2 Fire caused two transmission system faults near Anaheim Hills, California resulting voltage disturbances which resulted in a reduction of 900 MW of solar PV resources. The Canyon 2 Fire incident also revealed issues with inverter-based resources (IBRs) improper setting of LVRT. Many solar PV resources temporarily shut down when voltage levels fall below 0.9 per unit, resulting in a chain reaction contributing to more disruption of power supply. This loss of generation caused a frequency deviation in the Western Interconnection, with the system frequency reaching a low point of 59.878 Hz approximately 3.3 seconds after the fault occurred.

Grid operators and researchers depend on computational tools and simulations for conducting stability analysis. The tools like MATLAB, PSCAD, PowerWorld Simulator, etc. provide essential capabilities for assessing the stability of power systems, analyzing the dynamic behavior of various components, and predicting the system's response under different operating conditions. By utilizing computational tools and simulations, grid operators and researchers can gain valuable insights into the stability of the grid, identify potential issues, and design effective control strategies to maintain a reliable and secure power supply.

The recent rapid deployment and advances of converter-based generation have also lead to the development of new models to represent these devices in various contexts. Model development has been driven from two perspectives of opposite scales: the device-centric power electronic perspective and the bulk power centric power systems

perspective. From a device-centric perspective, highly detailed EMT converter models have been developed, called switching models, that simulate the power electronic components down to the level of detail of the pulse width modulation (PWM) signal in the order of hundreds of kHz. Switching models accurately represent the physical behavior of semiconductor switches used to build PECs and are extensively used to analyze switching times, switching transients, switching losses, switching faults, and instantaneous voltage and current dynamics. Due to the small (micro-second) time-step needed for simulations with switching models, there is significant computational burden to scale these models to larger systems. Switching model is typically simulated in systems with only one or a few converters due to this reason.

Levels of simplifications and linearizations are made to create more computationally efficient models, such as average models. Both small- and large-signal average models have been developed to assess small and large disturbances respectively [22], [23]. Applicability of the small-signal models are limited to specific scenarios where large variations or disturbances are not present. Further, positive-sequence models (PSM) used in positive-sequence simulators make additional simplifications based on the assumptions of a balanced system, and that the system operates around the fundamental frequency. PSMs have been the modeling approach from the bulk power perspective, due to their application in commonly used positive-sequence simulators for transient analysis [24]–[27]. However, the increase of in front and behind the meter converter-based generation in bulk power systems has been shown to invalidate those assumptions [28]. Numerous studies have indicated the need to incorporate EMT models of converters in large-scale power system studies either through co-simulation with positive-sequence

simulators or directly in EMT simulations [14], [24], [25].

To bridge the gap between high-fidelity EMT converter models and simplified phasor-based models, recent developments have been made with phasor models for converters, such as dynamic phasor models (DPM) and data-driven models. DPM uses simplified representations of power system components and assumes steady-state sinusoidal behavior [29]. Therefore, DPMs make it possible to model both faster dynamics than the traditional phasor models. This simplification may not capture the full complexity and dynamics of the system, leading to inaccuracies in certain scenarios. Moreover, DPM requires detailed knowledge of the system parameters, including component characteristics and network topology. This makes it less flexible in handling changes or uncertainties in the system.

Data-driven modeling involves creating models of an unknown system based on input and its corresponding output data. It doesn't necessitate in-depth understanding of system physical topology or complex models of voltage/current control loops, PLL, protection schemes, and related aspects. Data-driven models can adapt to changing system conditions, such as varying load profiles or the integration of renewable energy sources. They can be trained on updated data to capture evolving system dynamics without requiring explicit knowledge of component parameters or network topology. So, data-driven modeling exhibits flexibility and adaptability. Moreover, data-driven models can capture the nonlinear behavior and transient response of the system, making them suitable for analyzing complex system. Hence, data-driven models replace the structure of previous models with mathematical equations derived from input and output signals [30]. However, data-driven modeling requires high-quality and representative data. Due to the

advances in better hardware equipment to conduct experiments, high-quality data can be obtained.

1.2 Objectives

The primary objective of this dissertation is to develop a generalized simulation and modeling framework for extracting dynamics of PECs with GSFs and validate model accuracy through experimental comparison with physical measurements.

1.3 Contributions

Following contributions from this work are aimed to improve the existing state-of-art in power system research:

The key contributions of this dissertation are:

- Developed a methodology to experimentally collect data by exciting grid-following (GFL) and grid-forming (GFM) inverter with designed probing signals and extract their dynamics by implementing data-driven modeling approach,
- Investigated the modeling of inverters equipped with GSFs which supports grid voltage and frequency and maintain the value within an acceptable range.

1.4 Dissertation Outline

Chapter 2 provides a comprehensive study of the current state-of-the-art dynamic and transient modeling of PECs in CDPS. In Chapter 3, the development of a detailed model for studying data-driven modeling of inverters with GSFs is presented. In Chapter 4, a data-driven modeling framework for extracting PECs dynamics using a designed probing signal is presented. Chapter 5 delves into the development of testing

procedures for the application of system identification (SysId) algorithm to facilitate data-driven modeling of GFL inverters. The validation of data-driven modeling for GFL inverter with GSFs is presented. Furthermore, the experimental validation of the impact of varying irradiance on the dynamic modeling of GFL inverters using a real-time digital simulator is discussed. Chapter 6 outlines the data-driven modeling approach for GFM inverter dynamics using power hardware-in-the-loop (PHIL) techniques. Finally, Chapter 7 concludes by summarizing the development of a generalized simulation and modeling framework for extracting the dynamics of PECs with GSFs, limitation of this modeling approach, and the future work.

CHAPTER 2 State-of-the-Art and Challenges in the CDPS Dynamic Modeling

When modeling IBRs, it is essential to choose the right PEC model type, select component values, and to estimate the converter's response under different scenarios. This chapter provides a concise overview of the current state-of-the-art modeling technique employed in CDPS and a review of PEC model types used to analyze CDPS dynamic stability issues.

2.1 Switching Models

The switching model of a PEC includes power electronic switching devices, such as insulated-gate bipolar transistors. PWM techniques are used to control the gates of these switching devices to create sinusoidal current and voltage waveforms. The control structures to create this modulation and generate these waveforms are also included in switching models. The higher levels of control structures that maintain power sharing balance and voltage and frequency restoration can also be included in these models, as illustrated in the generic diagram of a switching model in Fig. 2.1. However, due to the computational demand associated with this highly detailed model, such higher level controls are rarely simulated with these types of models.

Switching models are also commonly presented in the literature as a benchmark to compare the accuracy of average models [22], [26], [27], [35]–[40], many of which are discussed in greater detail in the next section. In [41], a comparison of average models

This work was performed jointly with the full list of co-authors available in [31].This work is supported by the U.S. Department of Energy Office of Science, Office of Basic Energy Sciences, EPSCoR Program; Office of Electricity, Microgrid R&D Program; and Office of Energy Efficiency and Renewable Energy, Solar Energy Technology Office under EPSCoR grant number DE-SC0020281.

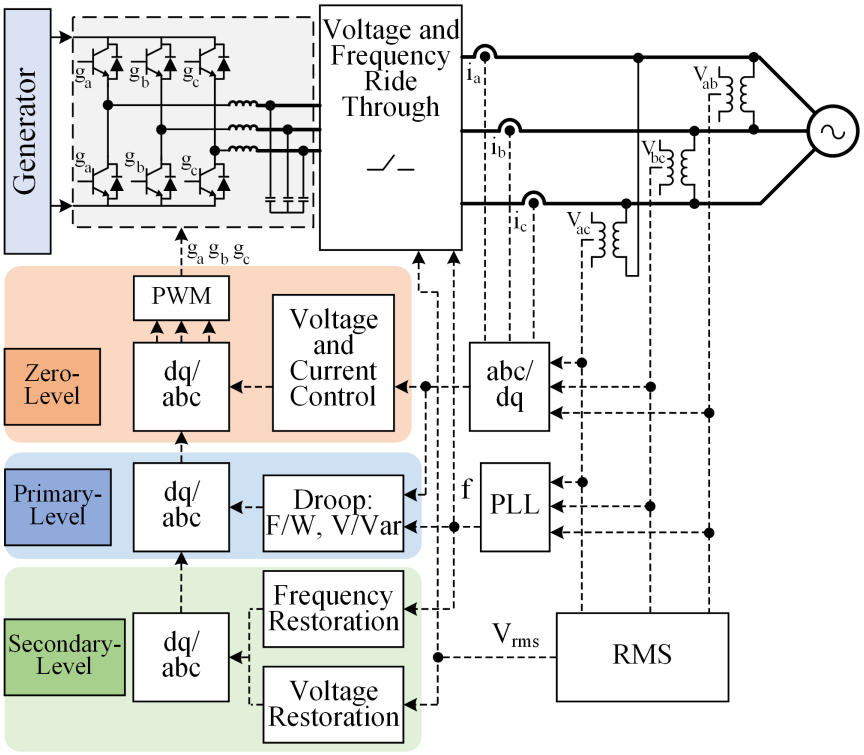

Figure 2.1. Generic switching PEC model representing major control groups [32]–[34].

and switching models determined that average models adequately simulate and capture common dynamic stability issues, including fault response, except in the case of prediction of harmonic distortion and electromagnetic interference. Contrarily, the research presented in [42] indicated it was necessary that high frequency switching and DC link dynamics are included in inverter models to accurately capture GFM and supporting modes [42], fault conditions [43], significantly unbalanced load conditions [42], and high frequency switching ripples [40], [44].

As seen by the recent discussion, there is not complete consensus of when a switching level model is necessary, as often average models are adequately comparable and much more computationally efficient. Regardless of the adequacy of switching models in comparison to average models for capturing specific dynamics, the high

computational burden involved in the simulation of switching models makes them impractical for use in system-level studies or even studies with more than one or two IBRs. However, the higher level of detail and accuracy are critical for examining modulation strategies, switching losses, and potentially other fast time scale dynamics.

2.2 Average Models

Average PEC models focus on capturing the low-frequency behavior of the PEC without accounting for high-frequency variations due to circuit switching. This modeling method transforms the original discontinuous model into a continuous model that provides the best representation of the system's macroscopic behavior by averaging the converter state variables (state-space averaging) or averaging the switch network terminal waveforms (average switch modeling). A generic PEC averaged switch model is shown in Fig. 2.2, which captures the general components that are included in average models. Average models are also divided into small-signal and large-signal models used to study small-signal and large-signal dynamics respectively. The following subsections discuss small-signal and large-signal average models.

2.2.1 Small-Signal Models

Small-signal analysis is the study of deviations from the operating point for a system subject to small disturbances. One of the main advantages of small-signal models is that they can be used to perform classical stability and performance analysis methods such as Bode/Singular-value plots, Nyquist plots, eigenvalue analysis, superposition-based analysis, and transient response analysis. However, these methods lose accuracy when the system is highly non-linear or in the presence of large disturbances [46]. The modeling of

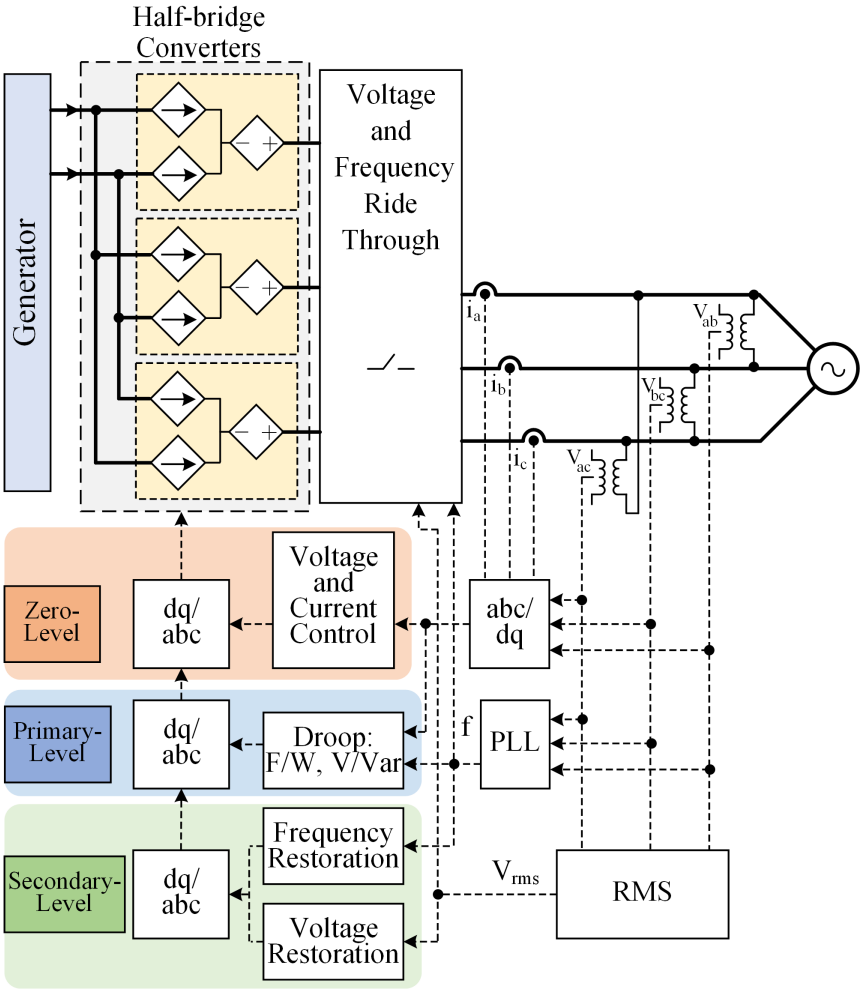

Figure 2.2. Generalized power electronic model with average equivalent circuit of inverter [32]–[34], [45].

CDPS is comprised of multiple dynamics and interactions that may or may not be linear. For example, voltage and current dynamics inside the converter are typically considered to be linear under nominal reference values. However, some variables such as active/reactive power, frequency, or DC-bus voltage can generate products between two or more state variables, discontinuities, or exponential/trigonometric calculations that can affect the accuracy of the small-signal model. Small-signal models can have inaccuracies when operating far from the linearization point. They struggle with describing switching dynamics due to their continuous assumptions. Additionally, implementing harmonics

within a linear framework proves complex. These limitations highlight the need for more sophisticated modeling approaches in dynamic systems with nonlinearity, switching, and harmonics.

2.2.2 Large-Signal Models

Large-signal models employ non-linear mathematical functions to describe non-linear components without linearization [47]. The large-signal model is important for analysis when PEC non-linearity is significant and when the response to large perturbations causes deviations that are substantially different from the response predicted by the small-signal model. Large-signal models have been used to perform numerous types of stability studies, including capturing shorter timescale output voltage dynamics and active power sharing dynamics. These models are beneficial for these short time scale stability analyses in comparison to switching models due to their increased computational efficiency gained through intelligent and validated averaging methodologies. However, compared to small-signal models, these models are computationally more burdensome. They remain unable to effectively describe switching dynamics due to their continuous nature. The trade-off between computational complexity and capturing system dynamics must be carefully considered when choosing the appropriate modeling approach.

2.3 Positive-Sequence Models

Efforts have been made to obtain models for IBRs so that power system simulations for transmission planning and operation could be implemented. Bulk power system dynamic analysis has historically focused on electro-mechanical dynamics with dynamic stability issues that typically range on the order of milliseconds to seconds.

Examples of such dynamic stability issues include inter-area oscillations, transient voltage, frequency stability, and protection relay settings. PSMs are representative of the dynamics of bulk power system devices in the range of 0.1 to 3 Hz, and up to 15 Hz for control systems [48]. These models assume the bulk power grid is operated under three-phase balanced conditions and that system frequency deviations from nominal are very small. On this time scale, PSMs are widely utilized in time-domain simulations applied for assessment of many power systems stability problems, including transient and small-signal stability [49] due to their accuracy at those time steps and computation efficiency for large transmission systems.

Sequence component analysis of power systems allows the representation of one three-phase unbalanced power system as three balanced systems. Under balanced conditions, the negative and zero-sequence phasors are negligible. Therefore, those two components are usually not of interest in transmission stability studies, which can often be represented by their positive-sequence network alone [50]. As a result, a simpler single-phase positive-sequence network can be used to represent the three-phase circuit, which is very useful for the simulation of large-scale three-phase systems.

In time-domain simulations for transmission stability assessment, it is considered that transients within the transmission network decay very fast and their dynamics can be ignored. Therefore, the transmission network and static loads can be represented by a positive-sequence network. In the same context, it is considered that the the dynamics of devices such as generators and their governor and excitation systems dominate transient (rotor angle) and small-signal stability problems. Therefore, those devices are represented by differential equations [50].

Modern positive-sequence analysis tools include generic open-source models of IBRs, such as those developed by the Western Electricity Coordinating Council (WECC) [51], and wind turbine models developed by the International Electrotechnical Commission (IEC) [52]. Models of converter interfaces were developed for Type 1 through 4 wind turbine generators with building blocks generic enough to also be applied to model inverters for solar PV power and even battery systems [53]–[55]. In North America, the development of these models was driven by the North American Electric Reliability Corporation (NERC), who recognized the need and called for standardized, non-confidential, and generic IBR models for positive-sequence based power flow and stability analysis to assist power system planning studies [56]. These models should be generic enough so that with adequate parameterization they could be capable of representing any converter-based resource in commercial software for power flow and stability analysis of bulk power systems [48].

Positive-sequence representations, however, prove overly simplistic in many cases. It is found that the assumptions regarding PSMs are violated in simulations that either contain power electronic devices such as flexible alternating current (AC) transmission systems and HVDC links or model fast transients, responses to faults, harmonics, or phase imbalance [57]–[59]. Good representation of the response to faults of unbalanced loads such as single-phase induction motors usually require more detailed models than PSMs [60], [61].

2.4 Dynamic Phasor Models

Variables of interest, such as voltages and currents, in power systems and PECs are typically periodic in steady-state. Phasor-based models utilize complex values to provide a convenient mathematical representation of those variables and circuit parameters such as the electrical network circuits' impedances and elements. In the literature, the phasor model can encompass both static and dynamic phasors [29]. Static phasor modeling assumes that the changes in fundamental frequency can be neglected; thus, it results in a simpler model that is well-suited for steady-state analysis and modeling transmission lines and loads in large power systems to which slow dynamics are attributed. From the point of view of dynamic analysis, it is important to model how those deviate from the steady-state [23]. DPMs are capable of modeling harmonics, and they provide a more accurate model for representing variations of phasors over time. However, DPM shows difficulties in performing classical small-signal stability assessment methods [62].

2.5 Data-driven Models

Data-driven modeling, in contrast to physics-based modeling, uses data to derive a model or parameters of a specific system. Physics-based modeling is performed through laws of physics that govern the components of the system. Physics-based modeling requires detailed knowledge of the system that makes it difficult for complex systems. However, data-driven modeling requires no or partial information about the system. The relationship between input and output is inferred from data. The models developed from this approach are called data-driven models. These models rely upon computational intelligence, classical statistics (ordinary least square or maximum likelihood estimation),

machine learning, etc., assuming the data contains sufficient information to describe the modeled system's physics [63]. Examples of data-driven algorithms include artificial neural network (ANN), support vector machines, random forest, etc. These models capture the dynamics with no or incomplete prior knowledge of the system's physical behavior.

Data-driven modeling can determine the structure, parameters, and temporal behaviors of a system or component of the system such as a PEC. Generally, the modeling of a dynamic system is classified into two approaches: first principle modeling and data-driven modeling [64]. First principle modeling utilizes the system's physics to derive the mathematical representation using established equations of the system or component. When the system is complex, model derivation using first principle modeling can be complicated due to the many components that may need to be modeled and parameters obtained. Additionally, preliminary information about the system or component may be unknown. Data-driven modeling is used to extract the model and/or parameters from the collected data without any prior knowledge or partial knowledge of the system. There are three types of data-driven models, which are classified in terms of known parameters and structured as a black-box, grey-box, or white-box model as shown in Fig. 2.3 ranging from the unknown structure/parameter to known structure/parameter of the underlying system respectively [65].

To effectively train data-driven model, substantial datasets are essential, emphasizing the significance of data availability. Their applicability is confined to systems possessing operational field data, restricting data-driven modeling use in scenarios lacking such information. Furthermore, the precision of data-driven models is intricately tied to

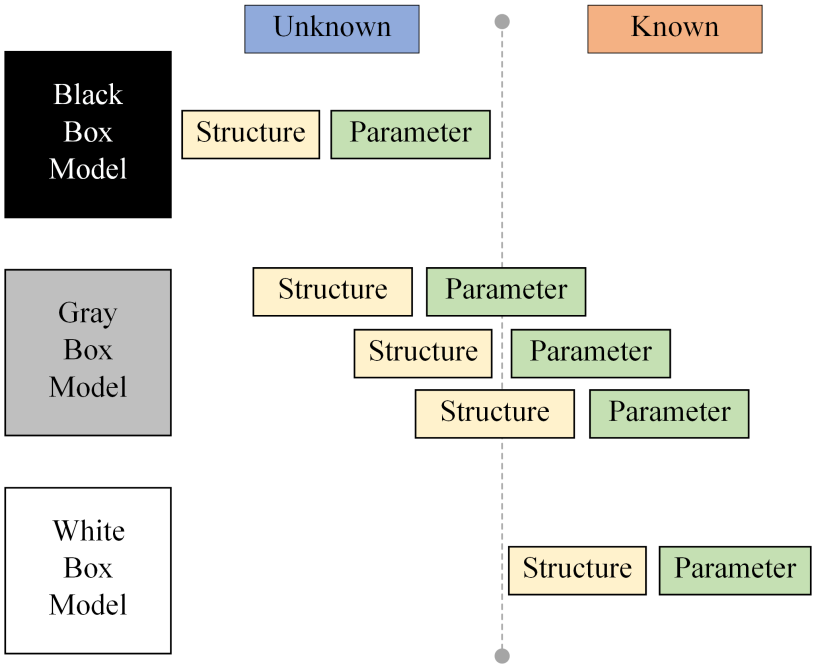

Figure 2.3. Comparison of different types of data-driven models. Adapted from [64].

the time-step granularity of the collected data. Ensuring a suitable time-step becomes crucial, as it directly influences the model's ability to deliver accurate and reliable predictions.

2.6 Challenges in Modeling of CDPS

Conventional transient planning, operation, and reliability techniques are encountering modeling challenges, potentially falling short in comprehending the intricate dynamics of the CDPS. These complexities entail the necessity for precise PECs models tailored to the intended application to capture intricate nonlinear dynamics. Earlier methods, such as positive-sequence and phasor-based models, sufficed for understanding power system dynamics within balanced and near-fundamental frequency conditions, primarily applicable to generator-dominated systems [3], [66]. In contrast, in CDPS, frequency deviations may arise due to rapid switching and induced harmonics from high PECs penetration, necessitating comprehensive models and simulations capable of

encompassing diverse power system phenomena for an accurate portrayal of CDPS dynamics.

As per the IEEE 1547-2018 standard for DERs, along with the advancement in grid codes, PECs equipped with several GSFs are responsible for providing several voltage and frequency ancillary services, which can be implemented in a variety of ways depending on the manufacturer and even under identical operating conditions [67]. Although, smart PECs with such functions are intended to aid in the integration of more converter-based DERs to regulate grid voltage and frequency, maintain grid stability, and increase grid dependability, their specific design and controls actions are proprietary and unknown and hence, adds another layer of complexity in modeling these PECs. This can lead to errors in power system modeling and simulation, as well as PECs dynamics, resulting in inaccurate results and analysis. In addition, depending on the activation of states, there is variation of power system dynamics as well. State in the context of the research means the operation of the converter when it is providing one of the ancillary services. So, these reveals dynamics of PECs depends on various factors like manufacturer's– physical topology, complex model of voltage/current control loops, models of PLL as well as different GSFs features. Due to the inclusion of the aforementioned factors, non-linearity exists in the manufacturers' most accurate PECs models, leading to complex mathematical models that are computationally intractable for real-time control. Thus, there's a growing necessity to investigate and accurately depict PECs incorporating GSFs within CDPS.

CHAPTER 3 Modeling Inverters with Grid Support Functions for Power System Dynamics Studies

With the increase in inverter-based generation integration in the electric grid and their different dynamics compared to traditional generation, power system dynamics needs to be assessed using accurate models. This becomes of particular importance when they also provide voltage and frequency support to the grid. For instance, the IEEE 1547-2018 standard recommends DERs provide GSFs [67]. These GSFs are capable of providing a number of grid services such as volt-watt, volt-var, frequency-watt, and/or voltage/frequency ride through. These functions aim to help increase the penetration capacity for renewable energy sources in electric power systems (EPS) [68], [69].

3.1 Chapter Objective

The main objective of this chapter is to present the development of a MATLAB/Simulink-based model to study EPS dynamics with GSF DERs. The simulation model of an inverter with GSFs is validated by comparing the simulation results obtained from the developed simulation model with the reference characteristic curve obtained from the IEEE 1547-2018 standard. Then, a study comparing DERs with only normal function and the GSFs is presented to study power systems dynamics as a sample of how the model can be used. The results demonstrated that upon implementing GSFs feature into inverters, they support grid voltage and frequency, ensuring the value remained within an acceptable range.

The chapter is organized as follows: an overview of different features of GSFs defined by the IEEE 1547-2018 standard is presented in Section 3.2. In Section 3.3, the

theoretical background on the dynamic modeling of power systems is provided. Validation of the GSFs implemented in the simulation model of inverter is illustrated in Section 3.4. The results are presented in Section 3.5 followed by the conclusion in Section 3.6.

3.2 Overview of GSFs from IEEE 1547-2018 Standard

The IEEE 1547-2018 standard [67] specifies that DER systems shall have the capability to regulate voltage and frequency of the grid and ride-through voltage/frequency during abnormal conditions. Voltage regulation is achieved by controlling either the active or reactive power output of the DER. Reactive power is controlled by any one of the following mutually exclusive modes: i) constant power factor mode, ii) voltage-reactive power mode (volt-var), iii) active power-reactive power mode (watt-var), and iv) constant reactive power mode. Among these modes to control reactive power, the default mode that shall be enabled is constant power factor mode and the value of power factor is set to unity (but can be operated at any power factor). Additionally, voltage-active power mode (volt-watt) is also used to regulate the voltage and by default this mode is disabled. To regulate grid frequency, frequency-droop mode (frequency-watt) is enabled. If both volt-watt and frequency-watt modes are enabled, minimum power obtained from any of these two modes will take precedence. If the grid voltage and frequency is outside normal operating range, DER activates the voltage/frequency ride-through for the minimum time as specified in the IEEE 1547-2018 standard beyond which DER ceases to supply power to EPS. An overview of some of the GSFs modeled in this chapter is presented below.

3.2.1 Voltage Ride-through Function

When the system voltage (V) is outside normal operating range (V_L = 0.88 p.u. — V_H = 1.10 p.u.) then this mode is activated. If the system voltage is less than the under-voltage threshold limit (V_u = 0.30 p.u.) or greater than the over-voltage threshold limit (V_o = 1.20 p.u.), then the DER ceases to energize the Area EPS and trips within a specified clearing time. Under and over-voltage tripping thresholds and clearing times are adjustable over the ranges of allowable settings specified in the updated IEEE 1547-2018 standard. Within that clearing time, DER shall inject power to the grid.

3.2.2 Frequency Ride-through Function

This mode is activated only when the system frequency (f) is out of normal operating range (f_L = 58.80 Hz — f_H = 61.20 Hz). If the system frequency is less than low-frequency tripping threshold (f_u = 57 Hz) or greater than high-frequency threshold (f_o = 62 Hz), then DER ceases to energize the Area EPS and trips within the respective clearing time. High and low-frequency tripping limits and clearing times are adjustable over the ranges of allowable settings specified in the updated IEEE 1547-2018 standard. Within that clearing time, DER shall inject power to the grid.

3.2.3 Voltage-reactive Power Function or Volt-var Mode

If the volt-var function is enabled, DER shall actively control its reactive power (Q) output to support the voltage of the grid. When the reference voltage (V_{ref}) falls further from the adjustable deadband (region beyond which GSFs activate), the inverter begins to inject reactive power (+var) and as the voltage rises above the deadband, reactive power is consumed. The voltage-reactive piecewise linear characteristics are shown in

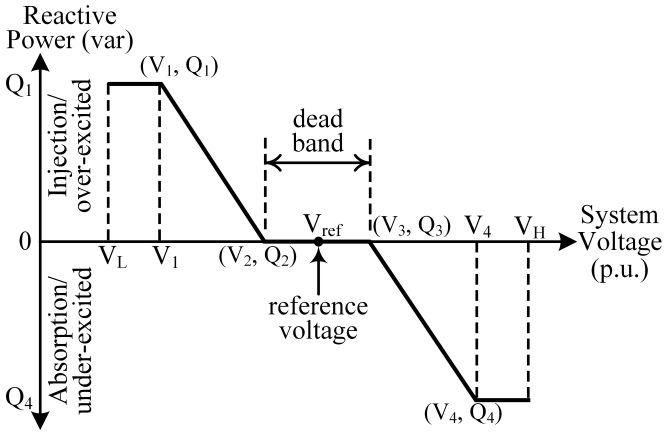

Figure 3.1. Example voltage-reactive power characteristic.

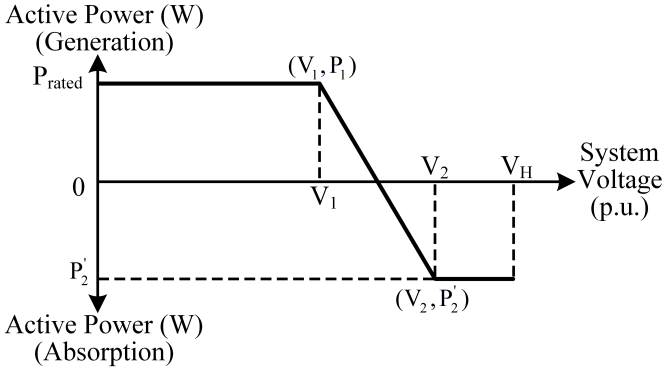

Figure 3.2. Example voltage-active power characteristic.

Fig. 3.1, where V_1, V_2, V_3, and V_4 are voltage parameters and Q_1, Q_2, Q_3, and Q_4 are reactive power parameters that are configured in accordance with the default parameter values specified in the updated IEEE 1547-2018 standard if not specified by area EPS operator.

3.2.4 Voltage-active Power Function or Volt-watt Mode

The updated IEEE 1547-2018 standard states that when the volt-watt function is enabled, DER shall actively limit the DER maximum active power (P) as a function of the voltage following a voltage-active power piecewise linear characteristic. Reduction in power for volt-watt mode occurs in the grid voltage ranging from V_1 to V_2 where V_1 varies

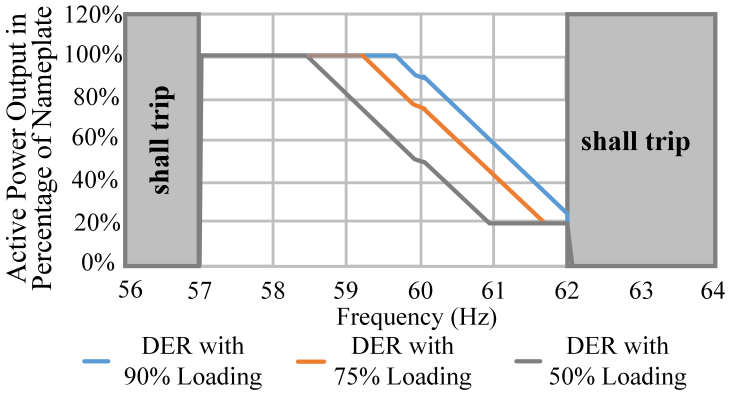

Figure 3.3. Example frequency-droop characteristic.

from 1.05 p.u. to 1.09 p.u. and V_2 varies from V_1 + 0.01 p.u. to 1.10 p.u. Fig. 3.2 shows a characteristic of a renewable DER system which can inject and absorb active power, where P_1 is the maximum active power that is injected by the DER, i.e., P_{rated}, and P_2' is the maximum amount of active power that can be absorbed by the DER and can vary from 0 to $-P_{rated}$.

3.2.5 Frequency-droop Function or Frequency-watt Mode

DERs shall have the capability of mandatory operation with frequency-droop during low and high-frequency ride-through. When frequency deviates from the adjustable deadband due to temporary frequency disturbances, but is still between the trip settings, this function is activated and the DER adjusts the active power output based on the system frequency following piecewise linear characteristic as shown in Fig. 3.3. The adjustable frequency deadband is between 17 mHz to 1 Hz; by default it is set to 36 mHz. Also, the frequency droop shall be between 3% and 5%, with a default value of 5%.

3.3 Basic Concepts of Dynamic Modeling

In this subsection, the dynamic modeling of a grid-connected inverter operating in current control mode is introduced. Among several PECs, grid-connected inverters are

widely used for the interconnection of batteries and PV; this chapter focuses discussion on this particular converter. This is followed by a simulation setup used to validate the GSFs.

3.3.1 Dynamic Modeling of GFL Inverter

A schematic diagram of a grid-connected inverter system operating in current control mode is shown in Fig. 3.4(a). The inverter is connected to the electric grid through a low-pass filter with inductance L_f; the inductance and resistance of the grid are represented by L_g and R_g, respectively. A phase locked loop (PLL) is used to track the phase-angle (θ_{PLL}) and frequency (f) of the grid. The voltage at point of common coupling (PCC) is denoted by V_c. I_f and I_g are the inverter current and current supplied to the grid respectively.

The inverter is operated either in the grid-feeding mode (normal inverter) or in grid-supporting mode. In grid-feeding mode, the inverter injects/absorbs constant active and reactive power (P^*_{nor} and Q^*_{nor}) to/from the grid, whereas in grid-supporting mode, the active and reactive power (P^*_{gsf} and Q^*_{gsf}) injected/absorbed by the inverter is changed so as to minimize the voltage and frequency variations in the system. The reference active and reactive power (P^* and Q^*) are obtained either from the normal function or from the GSFs as shown in Fig. 3.4(b). P^* and Q^* are fed to the current reference generator. Reference current (I^*) thus obtained is fed to current control loop.

The dynamics of this inverter system depend on the operation power level, DC voltage, and the parameters of the current controller and PLL. The dynamic response of the grid current depends largely on the control system employed. The current controller can be implemented using different control approaches such as a hysteresis band

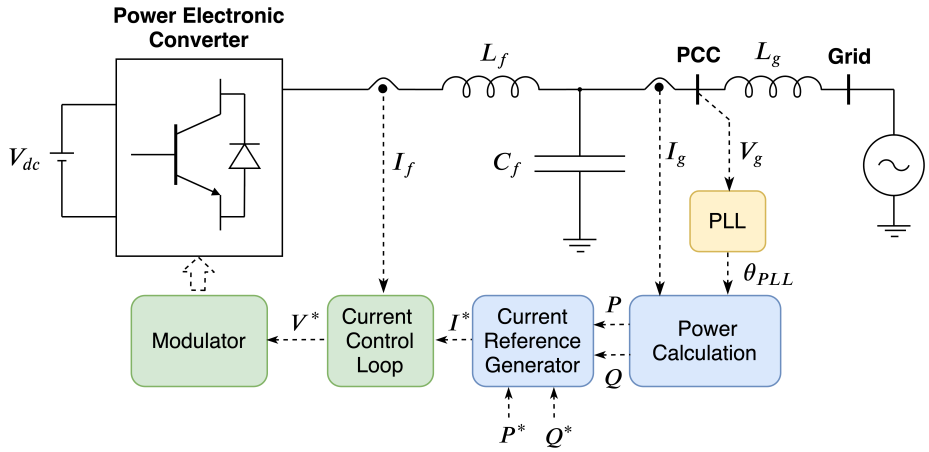

Figure 3.4. Schematic diagram of the various components and control loops in a grid-connected inverter system with both normal and GSFs.

controller or a PI or a PR controller among various other possibilities [70] which will also affect the dynamic behavior of the current response. In this chapter, hysteresis band controller is employed to control the current injected into the grid.

3.3.2 Simulation Setup

MATLAB/Simulink was used to develop models of grid-connected inverter with both normal and GSFs. The simulation setup is shown in Fig. 3.4. The simulation parameters are summarized in Table 3.1. The system considered is a 6 kVA inverter capacity and 20 kVA, 208 V microgrid system. To test volt-var and frequency-watt mode, the reference active power set during normal operation is 0.7 p.u. Changes in the resistive load connected at the PCC can be utilized to cause voltage and frequency deviations. Initially, a 10 kW load is connected at PCC. A 5 kW load is then added at the simulation time of 20 s, followed by a 5 kW load decrease at 35 s. During testing of frequency-watt mode, the volt-watt mode is disabled.

Similarly, to test volt-watt mode, there should be a condition of over-voltage in the system (V $\geq$ 1.05 p.u.). To meet this condition, the generator reference voltage is set to

1.02 p.u. Up to 25 s, battery injects 0.7 p.u. active power. To study the volt-watt mode operation, the DER active power is ramped up at the rate of 0.05 p.u./s from a simulation time of 25 s to 30 s, where it reaches a final value of 0.95 p.u. This leads to over-voltage in the system and the volt-watt mode in the DER is activated. Next, to study the dynamic operation of the volt-watt mode, initially a 15 kW load is connected at PCC. A 10 kW is then disconnected at the simulation time of 20 s. During testing of volt-watt mode, frequency-watt mode is disabled.

Table 3.1. Simulation parameters

Parameters	Values	Parameters	Values
R_g	0.106 Ω	L_f	7.40 mH
L_g	56.18 μH	V_g	208.00 V line
kVA rating of inverter	6.00 kVA	K_p of PLL	180.00
kVA rating of generator	20.00 kVA	K_i of PLL	3200.00
Band of HBCC	1.00 %	K_d of PLL	1.00

To study the dynamic model of the grid connected inverter, three cases were simulated and evaluated:

- Case I: Switch S_1 is opened, i.e., inverter power is not injected into grid
- Case II: Switch S_1 is closed and S_2 is opened, i.e., the inverter is connected to the grid with only the normal functions activated
- Case III: Switches S_1 and S_2 are closed, i.e., normal function along with GSFs of the inverter are enabled

3.4 Validation of the Inverter GSFs

To validate the simulated model of the inverter with GSFs, we compare the simulation results obtained from the developed simulation model with the characteristic

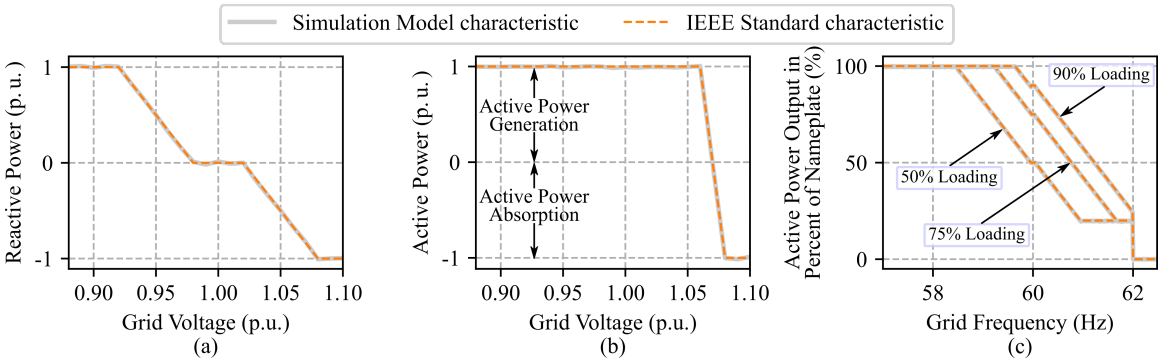

Figure 3.5. Validation of a) volt-var characteristic, b) volt-watt characteristic, and c) frequency-watt characteristic.

curve of the IEEE 1547-2018 standard, which is configured in accordance with the default parameter values for different GSFs. Based on the simulation data and that from the IEEE 1547-2018 standard characteristic curve, the fit of the model is calculated using the NRMSE [71] defined in 3.1:

$$NRMSE = \frac{\|y(t) - \hat{y}(t)\|}{\|y(t) - \text{mean } y(t)\|} \tag{3.1}$$

where $y(t)$ is the data obtained from the developed simulation model with the characteristic curve of IEEE 1547-2018 standard, and $\hat{y}(t)$ is the data obtained from the simulated model of the inverter with GSFs.

For the verification of GSFs, the generator in Fig. 3.4(a) was replaced by a controllable voltage source (CVS). For volt-watt and volt-var modes, the voltage input to the CVS was changed in steps of 0.01 p.u. at every 0.05 s interval for normal operating range by keeping the frequency constant at 60 Hz. Similarly, the frequency of the CVS was changed for frequency-watt mode by keeping the voltage constant at 1 p.u. During this process, all other parameters are kept constant and the simulation output of the inverter model is recorded.

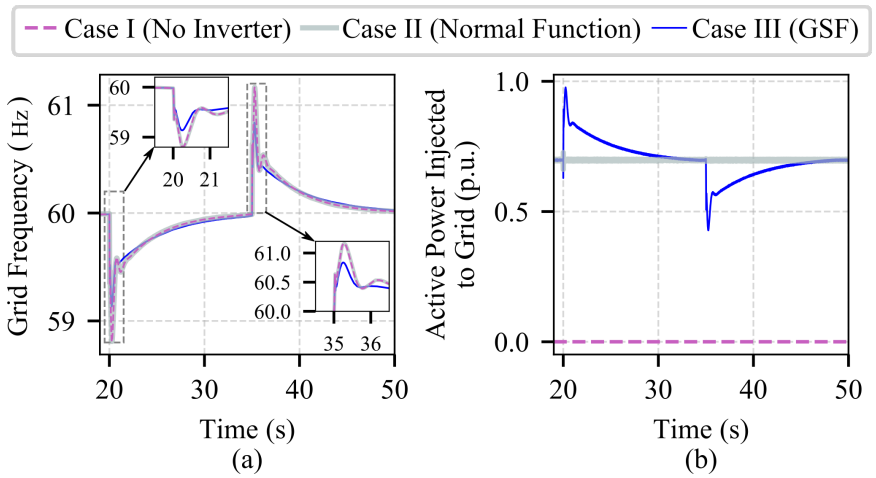

Figure 3.6. Comparison of grid frequency and active power injected to grid for Case I, II, and III. In Case III, frequency-watt mode is activated.

The reactive power injected/absorbed by DER to support the grid voltage is plotted in Fig. 3.5(a). The simulation results of developed model and characteristic curve from the IEEE 1547-2018 standard are consistent and the NRMSE obtained in this case was 1.25%. As seen in Fig. 3.5(b), the active power injected/absorbed by DER was reduced based on the system voltage. Simulation results match the characteristic curve from the IEEE 1547-2018 standard with a NRMSE 1.09%. Fig. 3.5(c) depicts the behavior when frequency-watt regulation was activated. Simulations were performed for three power outputs (50%, 75%, and 90%) of the nominal inverter power. Validation of the model was performed from 57 Hz, because below that frequency level, the protection setting of the frequency ride-through mode will be activated. The NRMSE obtained in those cases were 0.79%, 0.85%, and 0.93% for the 50%, 75%, and 90% of the nominal inverter power, respectively, and indicates that the developed model has acceptable levels of accuracy.

3.5 Results and Analysis

The simulation model of the inverter with GSFs were validated in subsection 3.4. The developed model is then used to study power systems dynamics under various

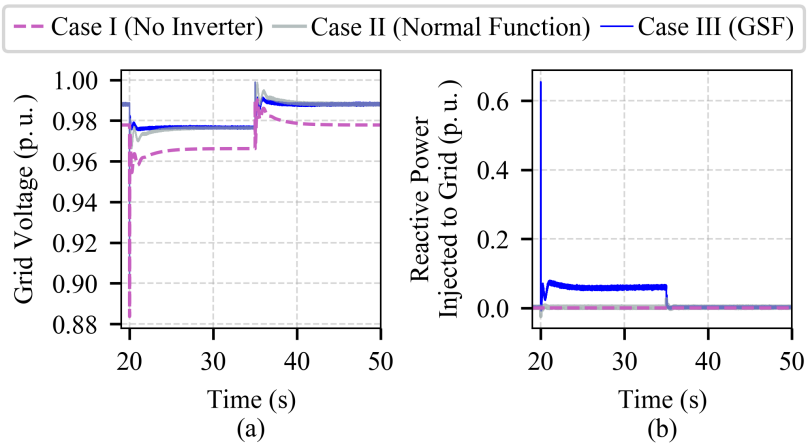

Figure 3.7. Comparison of grid voltage and reactive power injected to grid for Case I, II, and III. In Case III, volt-var mode is activated.

operating conditions. A comparison of DERs with normal function and GSFs features implemented in inverters are performed, and the results obtained by modeling inverters in MATLAB/Simulink with normal and GSFs to study power systems dynamics are presented and analyzed in this section.

3.5.1 Frequency-watt Mode

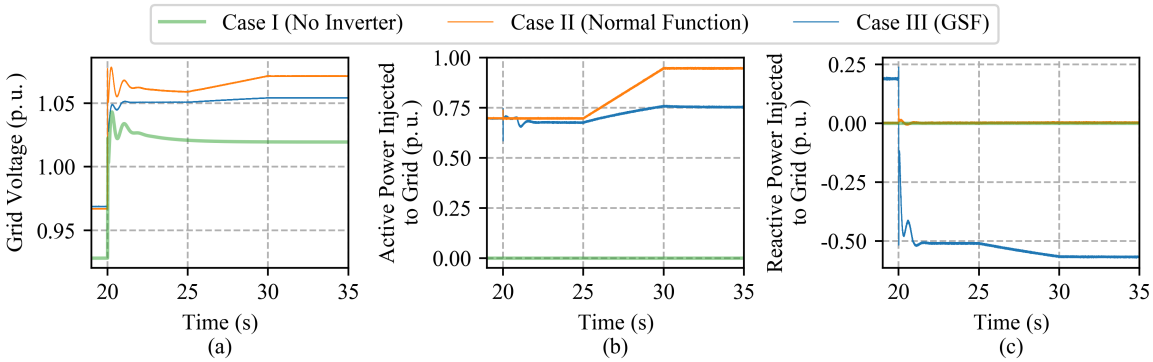

Figure 3.8. Comparison of grid voltage, active power, and reactive power injected to grid for Case I, II, and III. In Case III, both volt-watt mode and volt-var mode are activated simultaneously.

Fig. 3.6 shows the comparison of grid frequency and active power injected to grid for Cases I, II, and III. The simulation setup described in Section 3.3.2 was used to study

the frequency-watt mode of operation. After 20 s, a 5 kW load was added in the system which caused the grid frequency to drop as shown in Fig. 3.6(a). The frequency nadir in Cases I and II was 58.8 Hz, because in these cases no function for frequency support was active. However, for Case III, when the GSF was enabled the frequency nadir was reduced to 59.2 Hz because additional active power is injected to the grid due to the frequency-watt function. Fig. 3.6(b) shows that as the system frequency decreases, the active power injected by DER to the grid increases. Similarly, when a 5 kW load was disconnected at 35 s the system frequency increases in all three cases. However, the frequency increase for Case III was lower compared to the other two cases due to the frequency-watt function being active.

3.5.2 Volt-var Mode

Fig. 3.7 shows the comparison of grid voltage and reactive power injected to grid for Cases I, II, and III. The simulation setup described in Section 3.3.2 was used to study the volt-var mode of operation. When a 5 kW load was added after 20 s to the system, the voltage dropped below 0.98 p.u. as shown in Fig. 3.7(a). The lower set point to activate the volt-var mode was set to 0.98 p.u. while the upper set point was 1.02 p.u. [67]. From 20 s to 35 s, the voltage dropped below 0.98 p.u. for Cases I and II. For Case III, when the volt-var function is active, the DER injected reactive power to support the voltage as shown in Fig. 3.7(b). After 35 s, a 5 kW load was disconnected which caused the voltage to rise but the voltage did not cross the upper voltage set point for volt-var function. In this case, the volt-var mode was not active and no reactive power was injected by DER to the grid.

3.5.3 Volt-watt Mode

Fig. 3.8 shows the comparison of grid voltage, active, and reactive power injected to the grid for Cases I, II, and III. The simulation setup described in Section 3.3.2 was used to study the volt-watt mode of operation. After 20 s, a 10 kW load was disconnected which causes a rise in the grid voltage as shown in Fig. 3.8(a). When only the normal function was enabled, the voltage reaches 1.08 p.u., but when the GSFs are enabled the voltage rise was limited to 1.05 p.u. This is due to the activation of the volt-watt mode and volt-var mode simultaneously. Voltage support from the volt-watt mode leads to 0.02 p.u. reduction in active power output from DER as shown in Fig. 3.8(b) and that from volt-var mode requires 0.7 p.u. absorption of reactive power Fig. 3.8(c) by the DER. This is because of droop parameters.

After 25 s, the power output from the DER was increased with constant ramp-rate of 0.05 p.u./s. In this condition, when only normal function was activated, the DER injected the reference active power and ultimately, the grid voltage was further increased. When GSFs were activated the active power did not increase in the same way, as the voltage tends to increase, volt-watt mode function was activated and reduced the output active power. Curtailment in active power helped to maintain the grid voltage around 1.05 p.u. Moreover, volt-var mode also supports the voltage to maintain the grid voltage around 1.05 p.u.

3.6 Chapter Conclusions

This chapter presents a MATLAB/Simulink model for a PECs with the GSFs introduced in the IEEE 1547-2018 Standard. The models were developed to investigate

whether data-driven models could exhibit a behavior consistent with the expected model. GSFs implemented in the simulation model of inverter were validated by comparing developed simulation model characteristic curve with the IEEE 1547-2018 standard characteristic curve. The NRMSEs obtained for volt-var, volt-watt, and frequency-watt mode were less than 2%. Furthermore, the sample dynamic study of a power system activating the different GSFs modes was simulated and analyzed. Under various operating conditions, results show the improvement on grids' frequency and voltage profile using frequency-watt mode, and, volt-var and volt-watt modes respectively. This confirms that the GSFs model have dynamic behavior, establishing that data-driven models can capture the dynamic behavior of PECs.

CHAPTER 4 Modeling Framework for Extracting Power Electronic Converter Dynamics Using Designed Probing Signals

System identification has gained significant importance within the realm of power grids due to the growing complexity of the system. The evolving landscape of power system infrastructure, driven by the integration of renewable energy resources, controllable loads, and innovative power electronics technologies, presents new operational and control challenges. Traditional modeling approaches for power systems are insufficient given the intricate nature of IBRs and the lack of physics-based models. This necessitates a shift towards SysId techniques. SysId encompasses techniques utilized to describe a system through a suitable mathematical model, utilizing the system's input and/or output data. In SysId, deliberately designed input signals are used to probe the system under study. The resulting input-output data sets are then utilized to construct an appropriate model of the systems. Perturbing the systems with correctly designed probing signals plays a vital role. The probing signals used have a significant impact on the data that is measured and allow for accurate estimation of system parameters and identification of linear model to capture the system dynamics [72].

4.1 Chapter Objective

The main objective of this chapter is to develop a data-driven modeling framework for extracting PECs dynamics using a designed probing signals.

4.1.1 System Identification of PECs

System identification is a process to derive a mathematical model of an unknown system through observations of the input and corresponding output data. Using system identification tools, a mathematical model of a power electronic system that represents the dynamics of interest can be designed without knowledge of the underlying control structure and/or the control parameters. The dynamics of the converter will change based on different operating conditions. Several linear models for each operating condition can be developed and combined through a suitable mechanism [73]. Fig. 4.1 illustrates the basic concepts of a system identification process. The input signal $u(t)$ and the output signal $y(t)$ are first measured from the unknown dynamic process to be identified and dataset is then divided into training and testing datasets. 70% of the dataset is allocated for training purposes, while the remaining 30% is designated for testing. This split is chosen to ensure a substantial sample size, enabling accurate estimation and validation of the parameters.

The dataset is then fed into a system identification algorithm. SysId algorithm uses Instrument Variable (IV) method to process the training dataset such that least-square error is minimized for each data points and estimates the parameters of the system model $\hat{G(s)}$.

The relationship between the input and output that can be defined as:

$$y(t) + a_1 y(t-1) + \cdots + a_n y(t-n) = b_1 u(t-1) + \cdots + b_m u(t-m) \quad (4.1)$$

where n and m represent the number of poles and zeros of the system respectively.

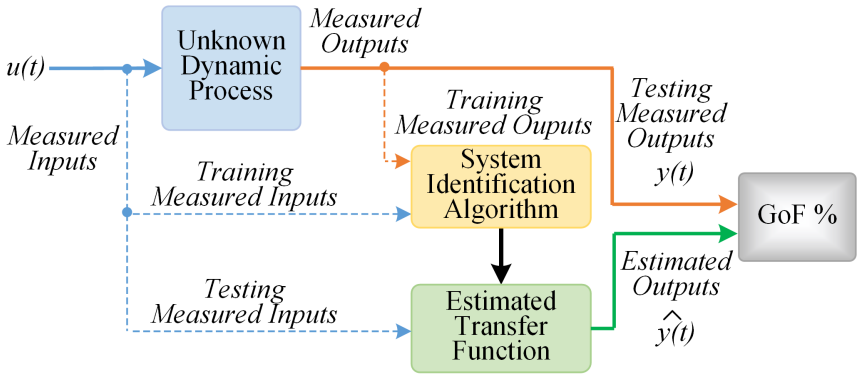

Figure 4.1. The fundamental concept of SysId. To identify the unknown dynamic process, the SysId method utilizes input and output measurements. The GoF is then calculated by comparing the actual outputs and estimated outputs.

Similarly, a_n and b_m represents the parameters of the difference equation of (4.1) or the coefficients of the equivalent transfer function (TF). Then in general, a dynamic system can be represented as:

$$\hat{y}(t \mid \theta) = [\phi(t)]^T \theta. \tag{4.2}$$

In (4.2), θ represents the set of the unknown parameters/coefficients of the system, and $\phi(t)$ represents the set of inputs $u(t)$ and outputs $y(t)$ of the dynamic system defined as follows:

$$\theta = [a_1, \ldots, a_n, b_1, \ldots, b_m]^T \tag{4.3}$$

$$\phi(t) = [-y(t-1) \cdots - y(t-n)\ u(t-1) \ldots u(t-m)]^T \tag{4.4}$$

Now, if we define Z^N as the set of known measurements and N is overall input-output data in the time interval $1 \leq t \leq N$:

$$Z^N = \{u(1), y(1), \ldots, u(N), y(N)\} \tag{4.5}$$

then the unknown parameters of the system, θ, can be estimated by employing a least-squares method utilizing the following cost-function [74]:

$$\underset{\theta}{\text{minimize}}\, V_N\left(\theta, Z^N\right). \tag{4.6}$$

where

$$V_N\left(\theta, Z^N\right) = \frac{1}{N}\sum_{t=1}^{N} \|y(t) - \hat{y}(t \mid \theta)\|^2 \tag{4.7}$$

Based on the collected input-output data, a set of models with different numbers of poles and zeros can be fitted to the data. The goodness of fit (GoF) of the model can be calculated using a metric such as the normalized root-mean-square error fitness value defined as [75]:

$$\text{GoF} = 100 \times \left(1 - \frac{\|y(t) - \hat{y}(t)\|_2}{\|y(t) - \text{mean}\, y(t)\|_2}\right) \tag{4.8}$$

where, $\|.\|_2$ indicates 2-norm vector.

Furthermore, to compare different models based on the GoF and complexity of the model the Akaike's Final Prediction Error (FPE) can be used, defined as [76]:

$$FPE = \det\left(\frac{1}{N}\sum_{t=1}^{N}\left(e(t,\hat{\theta_N})\right)\left(e(t,\hat{\theta_N})\right)^T\right)\left(\frac{1+\frac{d}{N}}{1-\frac{d}{N}}\right) \tag{4.9}$$

where $e(t)$ represents the prediction errors and d is the number of estimated parameters. A lower FPE represents a more accurate model of the system.

4.1.2 Design of Probing Signals for the data-driven Modeling

In data-driven modeling, perturbing the PECs with properly designed probing signals - which act as input data during SysId - plays an important role as it is the only method to influence the process and learn more about system behavior [77]. But before employing any signal as a probing signal the design constraints imposed by the power system and the SysId theory (the concept is to position the content of the probing signal in the frequency band of interest by the application) need to be strictly followed [72]. In addition, the system could have different time constants. So, for accurately estimating time constant and for emphasizing a frequency range based on signal frequency, rectangular/square are ideally suited for identification [77] square and rectangle signals are non-sinusoidal periodic waveforms in which the amplitude alternates between defined minimum and maximum values at a constant frequency. Relying on the aforementioned theory, four different probing signals (i.e., logarithmic square chirp, square, sine, and logarithmic sine chirp) are compared in [78], which concludes that logarithmic square chirp outperformed other signals in model accuracy based on GoF to extract dynamics of inverters. Logarithmic square chirp-where logarithmic sweeping of frequency of a square wave signal occurs-will, therefore, be used as a probing signal for perturbing the system. The signal that is used in the research has the following fundamental explanation:

$$x(t) = A \text{ square}(wt) \tag{4.10}$$

Here, $x(t)$ is the square wave signal, A is the peak amplitude of the square wave and wt is the phase which is updated according to the trapezoidal method indicated in the following

Eqn. 4.11.

$$(wt)_k = (wt)_{k-1} + \frac{t_k - t_{k-1}}{2} \times 2 \times \pi \times (f_{(t_k)} + f_{(t_{k-1})}) \tag{4.11}$$

where, at discrete time instant k (and $k-1$ represents the previous time instant), $(wt)_{k-1}$ and $(wt)_k$ represent previous and current time instant phase angle, t_{k-1} and t_k are the time at discrete instant $k-1$ and k, $f_{(t_k)}$ and $f_{(t_{k-1})}$ are the frequency at t_{k-1} and t_k respectively. Similarly, the frequency $f_{(t_k)}$ is defined as in :

$$f(t_k) = f_0 \times \frac{f_0}{f_1}^{(\frac{1}{T})^{t_k}} \tag{4.12}$$

where f_0, f_1, and T represent the starting frequency, final frequency, and time length of the chirp signal respectively.

4.1.3 Design Criteria of Chirp Signal

Based on the fundamental explanation of the signal, the design criteria of the chirp signal presented in this chapter are f_0, f_1, T, and A.

4.1.3.1 Final Frequency (f_1)

f_1 is the final frequency of a chirp signal. In other words, it is the frequency at which the designed signal will have minimum hold time T_h (i.e., the shortest period of time for which the signal stays constant). However, T_h of the signal should neither be chosen too small nor too large. It means, if it is selected too small, the process will have no time to settle and the model identified from such data will not be able to describe the static behavior well. Similarly, if it is selected too large, it would overemphasize low frequencies, but, much worse, it would leave large areas of the input space (scatter plot of

input data and output data) uncovered with data, and thus the model might not properly capture the process behavior in these regions as the data simply contains no information on them. Hence, it is reasonable to choose the minimum T_h approximately equal to the time constant (τ_{system}) of the system [77]. Hence, the final frequency of the signal can be obtained as :

$$f_1 \approx \frac{1}{2 \times T_h} \approx \frac{1}{2 \times \tau_{system}}$$

Here, the multiplication of 2 in the above equation is carried out for considering the total ON and OFF time of the signal. Furthermore, for knowing τ_{system}, step input is given to the system and the settling time (t_s) of the system is calculated. Depending on tolerance band considered, τ_{system} can be calculated as [79]:

$$\tau_{system} = \frac{t_s}{3} \quad \text{(for 5\% tolerance band)}$$

$$\tau_{system} = \frac{t_s}{4} \quad \text{(for 2\% tolerance band)}$$

4.1.3.2 Starting Frequency (f_0)

f_0 is the minimum frequency of a chirp signal. It is selected in an iterative manner and needs to get updated in each iteration until the time constant of the predicted model (τ_{model}) matches τ_{system} as indicated in Algorithm 1.

4.1.3.3 Time Length of Signal (T)

T of the signal is the time length of the chirp signal and is expressed as the time between two particular instantaneous frequencies f_0 and f_1 and is expressed as [80]:

$$T = \frac{1}{D\% \times f_0 \times log(\frac{f_1}{f_0})}$$

where D is the percentage rate of exponential change in the frequency of the signal.

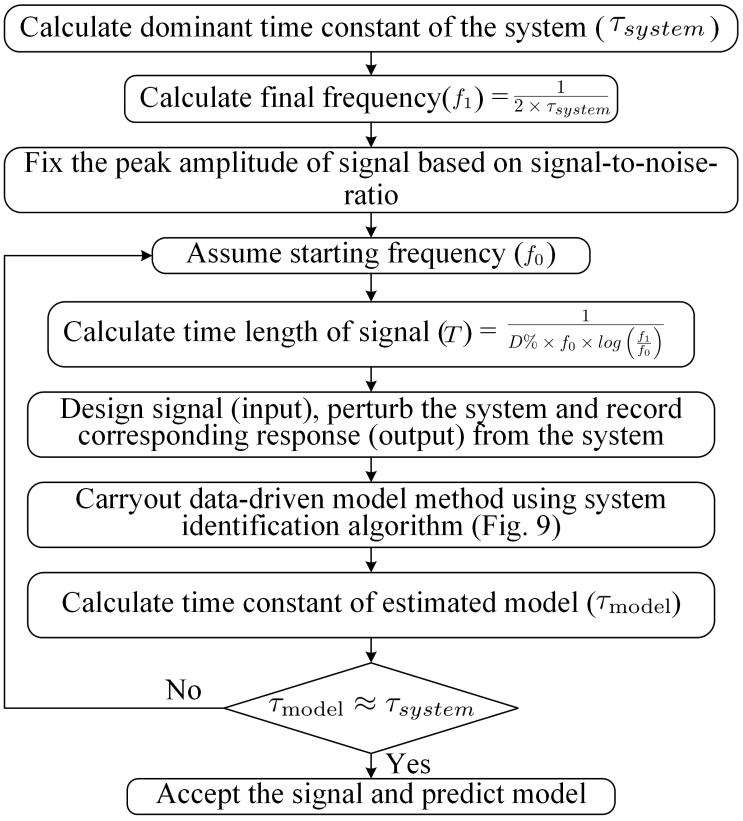

Figure 4.2. Flowchart to design probing signal for SysId.

4.1.3.4 Peak Amplitude of Signal (A)

A is the peak amplitude of the square chirp signal and should be chosen considering the signal-to-noise ratio (SNR) [81]; it varies depending on the system. It should be carefully chosen so that, after perturbing the system with designed signals, the output signal incorporates the least amount of noise possible. Poor selection may necessitate the use of other filters to remove noise, which will be covered in more detail in the results and analysis section. The flowchart for designing the probing signal for data-driven model parameterization is given in Fig. 4.2.

4.2 Methodology to Collect Data for Grid-following and Grid-forming Converter

In this section, the methodology to obtain the the experimental data for both GFL and GFM inverter is presented. Firstly, GFL inverter is excited by designed probing signal to identify the TF of GFL inverter. The amplitude of probing signal must fall within the range of 0.88 p.u. to 1.1 p.u. so as to operate GFL inverter in a normal condition and to represent under- and over- voltage conditions. Then, voltage amplitude (measured inputs) at the PCC and current injected by the GFL inverter to the grid (measured outputs) are logged through the Opal-RT system, and thus, collected data are split into different regions. Then, the data is filtered using the mean filter to smooth the array of sampled data. Furthermore, the mean of both voltage and current measurements are eliminated to obtain a more accurate model. This allows SysId to focus on the real variations caused by the probing signals rather than undesirable data trends. The dataset is separated into two parts for cross-validation: a training set for computing unknown poles and zeros, and a validation set for validating the resulting model. Then, the poles and zeroes are swept to generate distinct linearized models that are accurate and computationally efficient, using a SysId technique. Moreover, models with respective poles and zeroes are compared using the Akaike's FPE and the most accurate model with the lowest Akaike's FPE is chosen as the final TF model for each range [82].

Secondly, the flowchart to identify the TF of a GFM inverter from the SysId algorithm is shown in Fig. 4.4. In order to determine the TF of GFM inverter, the measured inputs, including the active and reactive power supplied by the GFM inverter, along with the output frequency and voltage at the terminal of the GFM are logged using

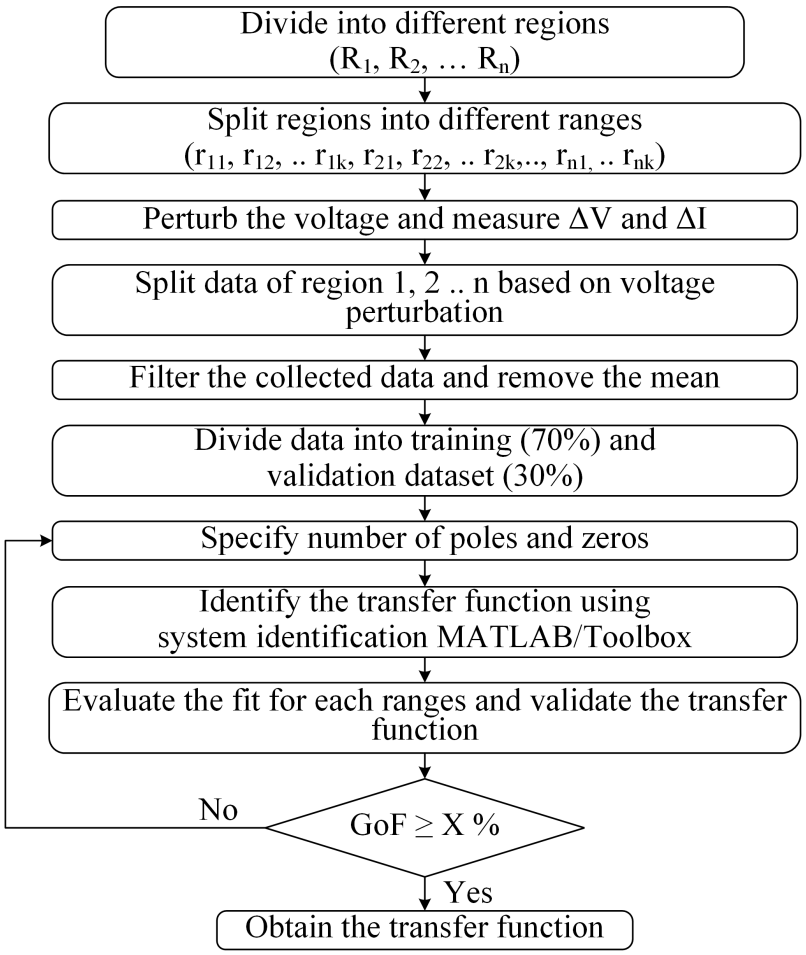

Figure 4.3. Flowchart to identify TF of GFL inverter using SysId algorithm.

the Opal-RT system. The collected data is subsequently divided into distinct ranges for analysis. Then, the data is filtered using the mean filter to smooth the array of sampled data. Furthermore, the mean of both active power and reactive power, and frequency and voltage of GFM measurements are eliminated to obtain a more accurate model. This allows SysId to focus on the real variations caused by the probing signals rather than undesirable data trends. The dataset is separated into two parts for cross-validation: a training set for computing poles and zeros, and a validation set for validating the resulting model. The number of poles and zeroes are chosen based on the finding from analytical approach and generate distinct linearized models that are accurate and computationally

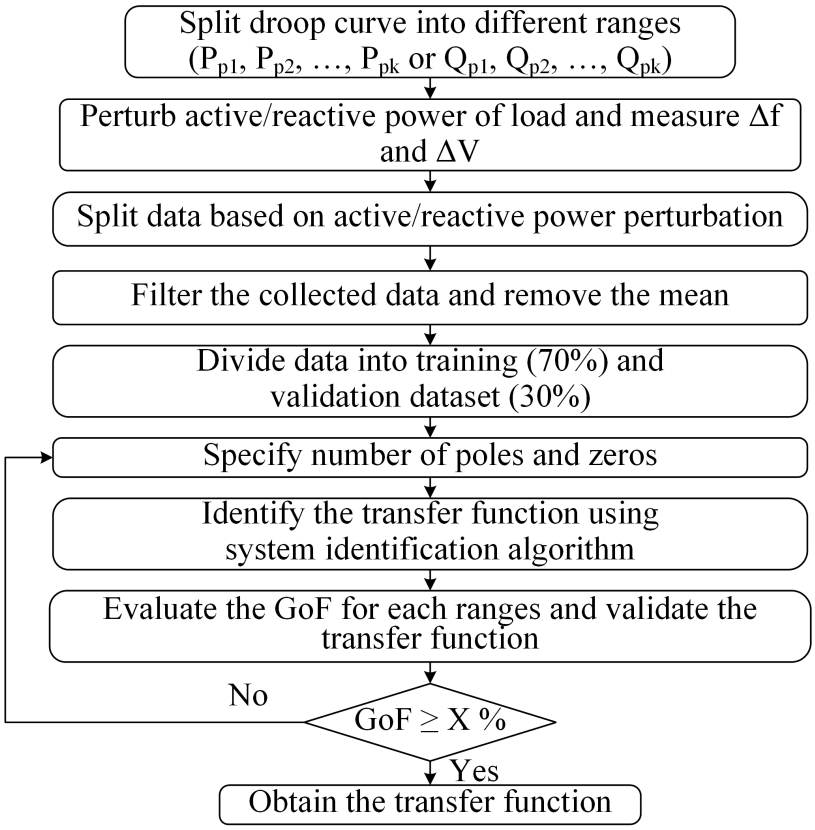

Figure 4.4. Flowchart to identify TF of GFM inverter using SysId algorithm.

efficient using a SysId technique.

4.3 Validation of TF Model Obtained from SysId

Fig. 4.5 depicts a schematic diagram to validate the TF obtained from SysId when inverter is operating in GSFs mode. To validate the accuracy of the TFs, the inverter was excited through the Puissance Plus Power Amplifier with the same probing signal in parallel with its TFs. V_{abc_ref} is the reference voltage amplitude at PCC. The output current injected to the power amplifier by the inverter was passed to $abc-dq0$ block to only obtain quadrature axis current, i_{invq}. Here, V_{abc_ref} was converted to $dq0$ component, and only the d-component (V_d) was used as it is associated with the voltage amplitude. The mean value of V_d was removed before feeding to the TF of different regions. The

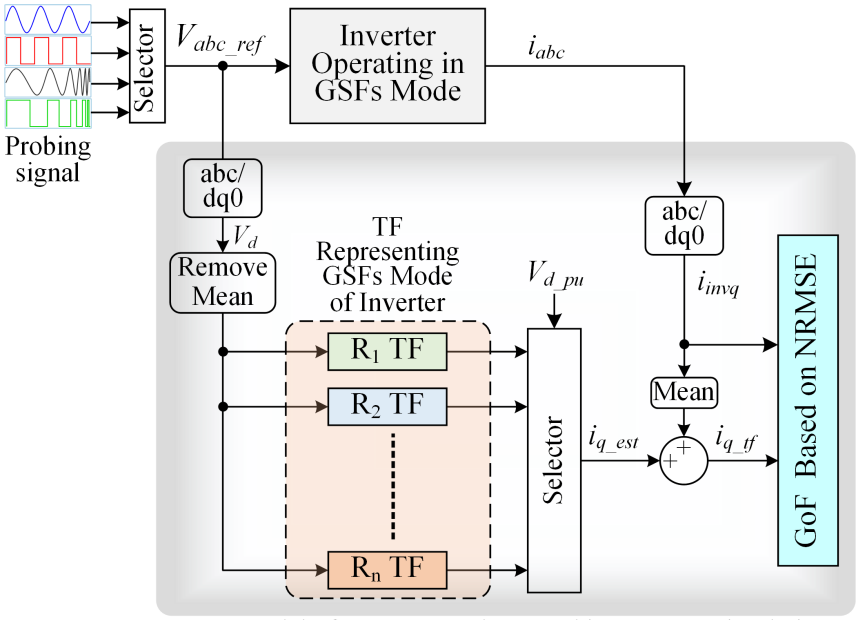

Figure 4.5. Schematic diagram to validate the TF obtained from SysId when inverter is operating in GSFs mode.

output of the TF was the estimated current which was inputted to the selector block. The selector block chose the correct estimated current based on the per-unit value of voltage V_{d_pu}. Mean value of sensed current (i_{invq}) was then added in the estimated current (i_{q_est}) to get actual estimated current (i_{q_tf}) from the TF block. The GoF based on NRMSE was then calculated to compare the fit percent.

4.4 Implementation of TF Model in EMT Simulation

After validating the model, the TF model of an inverter can be integrated into an EMT simulation for dynamic study, as illustrated in Fig. 4.6. In this process, the terminal voltage (v_{abc}) is sensed and subsequently processed by the $abc - dq0$ block to obtain the direct axis voltage (V_d) and quadrature axis voltage (V_q). These V_d and V_q values are then input to the TF model, which has been previously identified using SysId techniques, to

compute the corresponding direct and quadrature axis currents (i_d and i_q). The computed i_d and i_q are then passed through the $dq0 - abc$ block to obtain the reference current, (i_{abc}). This current is then applied to controllable current source to generate the PCC voltage (V_{PCC}).

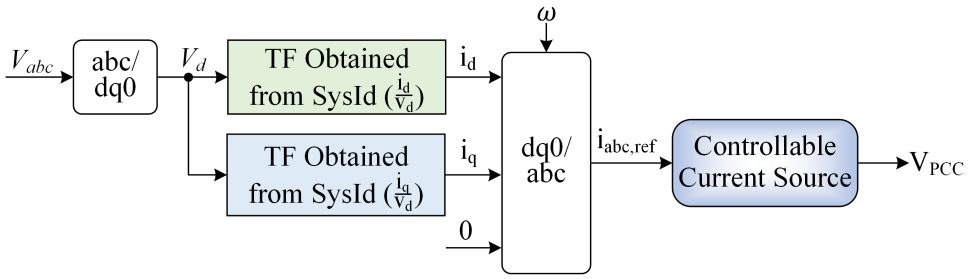

Figure 4.6. Implementation of TF model in EMT simulation for dynamics study.

4.5 Chapter Conclusions

In conclusion, this chapter has highlighted pivotal aspects necessary for data-driven modeling of PECs with a designed probing signals. Firstly, it emphasized in SysId algorithm for obtaining the TFs of PECs. Secondly, it emphasized how to design a probing signals for dynamic modeling of PECs. Thirdly, the methodology to collect data for both GFL and GFM inverter are developed. Lastly, it detailed the essential steps to integrate the derived TFs model into EMT simulations.

CHAPTER 5 Data-driven Modeling of Grid-following Inverter Dynamics Using Power Hardware-in-the-Loop

With the advancement in power electronics technology and grid standards, traditional converters are being supplemented with the new IEEE 1547-2018 standard based GSFs to support power system voltage and frequency. Inverter dynamics in power systems vary with different modes of operation, thus to capture the converter dynamics partitioned-based data-driven modeling of PECs with GSFs is proposed. Partitioned is done based on the operating states of GSFs of PECs. The partitioned operating ranges are represented via simpler linear models utilizing system identification algorithm.

5.1 Chapter Objective

The main objective of this chapter is to derive a dynamic model for the GFL inverter utilizing a data-driven partitioned modeling approach. This involves recording the current output response of the GFL inverter to variations in the PCC voltage, achieved by probing the inverter with various probing signals as designed in Section 4.1.2. The SysId algorithm as explained in Section 4.1.1 is employed to generate the dynamic model of the GFL inverter, and its accuracy is confirmed through validation under the Volt-VAr GSF. The methodology used identifies reduced-order dynamics of the GFL inverter interfaced with the grid. Furthermore, the study analyzes the GoF when the GFL inverter is perturbed with probing signals and indicates which one would estimate an accurate GFL inverter model.

The rest of the chapter is organized as follows. Section 5.2 presents a dynamic modeling of GFL inverter. Section 5.3 provides an explanation of the partitioned modeling

approach applied to Volt-VAr, followed by a detailed description of the probing signal parameters. Section 5.5 presents the experimental setup for identifying the TF of the GFL inverter using different probing signals and the results are presented in Section 5.6. Finally, Section 5.7 concludes the study.

5.2 Dynamic Modeling of GFL Inverters

A schematic of a GFL inverter system operating in current control mode is shown in Fig 5.1. The inverter is connected to the electric grid through a low-pass filter with inductance L_f and capacitance C_f; the inductance of the grid is represented by L_g. The inverter is being operated in the GFL mode injecting the reference active and reactive power commands P^* and Q^* respectively. A PLL is used to track the phase-angle of the grid, θ_{PLL}. Then a current controller (e.g., proportional-integral (PI)/ proportional-resonant (PR) controller) is employed to control the current being injected into the grid.

The dynamics of this inverter system depends on various factors such as operation power level, DC voltage, parameters of the current controller, and the parameters of the PLL. The dynamic response of the grid current, for instance, depends largely on the control system being employed — the design and controller gains will be different among various manufacturers.

5.3 Partitioned Modeling of GSFs From IEEE 1547-2018 Standard

Several GSFs for IBRs are being added for supplementary voltage and frequency services [78]. Volt-Var, Volt-Watt, and Freq-Watt modes of operation of the inverter are explained in this section. However, the methods presented can be extended to other GSFs

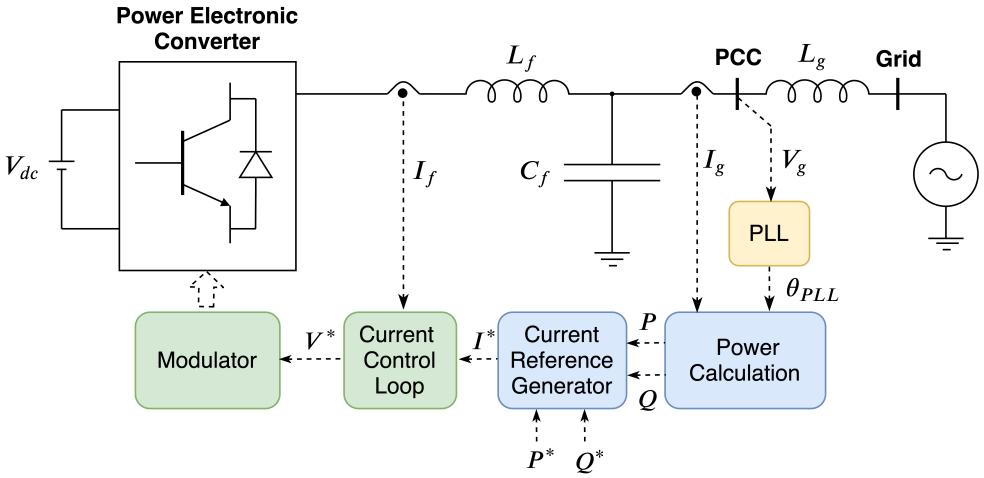

Figure 5.1. Schematic diagram illustrating the various components and control loops in a typical GFL inverter system.

as well.

Due to the presence of nonlinearities in PECs, modeling of PECs with GSFs over diverse operating regions results in intricate dynamic models, and the complex dynamics of the whole operating region are not effectively captured by a single linearized model [83]. Therefore, the inverter operating regions are further divided into multiple linear regions. Each region (represented by R) is separated into several small ranges (represented by r) based on the magnitude of voltage/frequency. A linear TF for each range is determined using the SysId algorithm as explained in Section 4.2. Several regions and ranges of the Volt-VAr, Volt-Watt, and Freq-Watt modes are shown in Fig. 5.2, Fig. 5.3, and Fig. 5.4, respectively.where $r_{11}, r_{12}, .., r_{21}, r_{22}, .., r_{5k}$ are ranges; the first index represents the region and second index represents voltage/frequency amplitude change depending upon different GSFs mode.

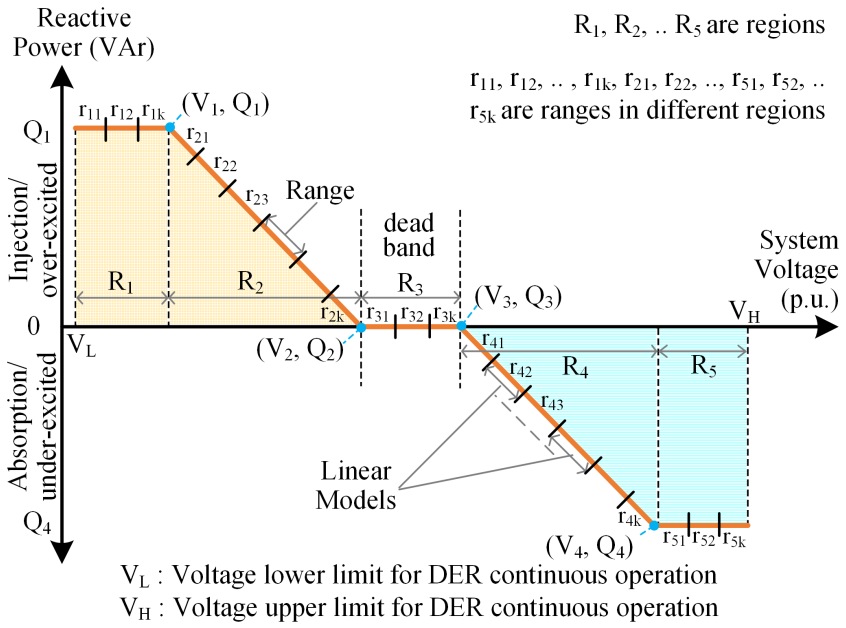

Figure 5.2. The Volt-VAr characteristics curve depicts several regions and ranges.

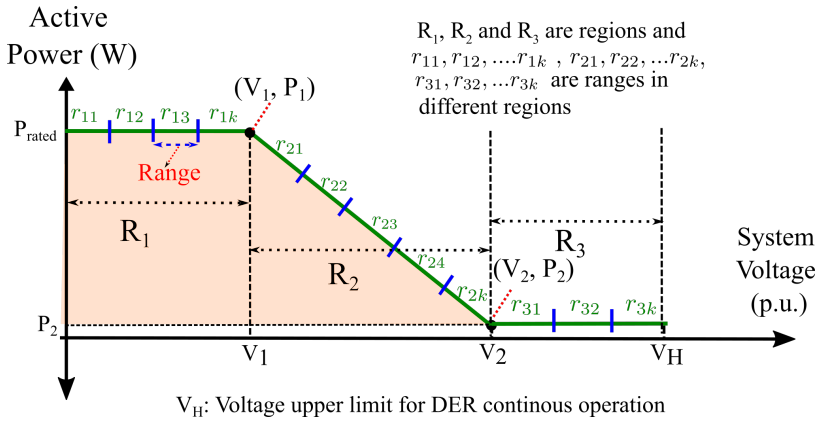

Figure 5.3. The Volt-Watt characteristics curve depicts several regions and ranges.

5.4 Probing Signals

The flowchart to identify the TF of a GFL inverter operating in Volt-VAr mode from the SysId algorithm is shown in Fig. 4.3. Different probing signals (square wave (Sq), sine wave (Sine), logarithmic square chirp (Sq-Chirp), and logarithmic sine chirp (Sine-Chirp) signals) of varying voltage amplitude were used to perturb the GFL inverter. These probing signals are used as they have all the variation in frequency and magnitude

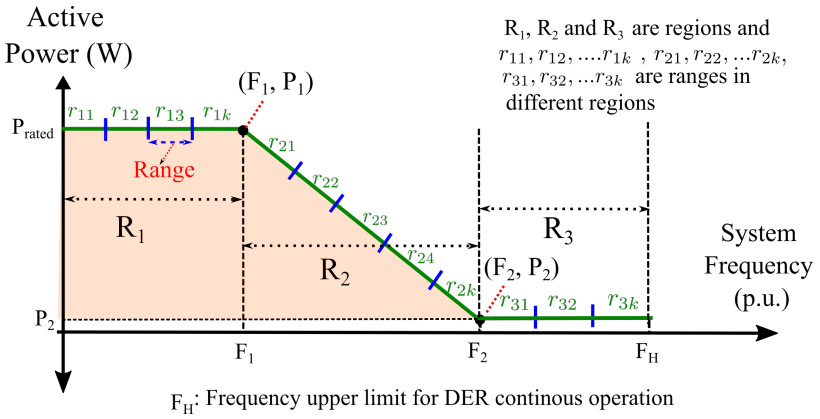

Figure 5.4. The Freq-Watt characteristics curve depicts several regions and ranges.

as described in the Section 4.1.2 and are designed from the standpoint of SysId theory, as well as design restrictions imposed by the power system [72]. The parameters for the probing signals used are shown in Table 5.1. For all probing signals, voltage amplitude is varied from 0.895 p.u. to 0.905 p.u. for 15 sec and then the amplitude is increased by 0.005 p.u. for the next range until amplitude reached 1.095 p.u. Here, 0.01 p.u. step-change is done based on the region 5 voltage range availability on Volt-VAr mode. The frequency for Sine and Sq wave is 1 Hz and that for Sine-Chirp and Sq-Chirp is varied from 1 Hz to 32 Hz. The values of frequency are chosen based on the settling time response parameters of the GFL inverter.

Table 5.1. Parameters of probing signals.

Input Signal	**Voltage Amplitude Variation (p.u.)**	**Step Change (p.u.)**	**Frequency (Hz)**
Sine	0.895-1.095	0.01	1
Sq	0.895-1.095	0.01	1
Sine-Chirp	0.895-1.095	0.01	1-32
Sq-Chirp	0.895-1.095	0.01	1-32

5.5 Experimental Setup

Data-driven modeling for three GFL inverters are conducted: i) 700 W GFL inverter from SMA (Sunny Boy SB 700U) and ii) 10 kW Fronius Symo Inverter (FSI), iii) Two-phase 5 kW SMA inverter.

5.5.1 Experimental Setup for 700W SMA Inverter

The experimental setup used for identifying the dynamics of a GFL inverter is shown in Fig. 5.5. The device under test is a 700 W GFL inverter from SMA (Sunny Boy SB 700U) whose TF is to be determined. A solar array simulator (SAS) was used to emulate the DC output of a PV system and the test device is connected to an Opal-RT which consists of a OP5707 real-time simulator (RTS) combined with a power amplifier from Puissance-Plus. In conjunction with the console PC, the RTS and the power-amplifier unit can emulate grid voltage of varying output magnitude, phase, and frequency. A resistive dump-load is also connected to consume excess power that cannot be consumed by the power amplifier. The nameplate rating of the GFL inverter from SMA is given in Table 5.2.

Table 5.2. SMA GFL Inverter's Nameplate Ratings (Sunny Boy SB 700U).

Nominal voltage	120 V
Voltage Range	106-132 V
Frequency Range	59.3-60.5 Hz
Nominal frequency	60 Hz
MPPT range	75-200 Vdc

To determine the TF of the GFL inverter, the dynamic response of the inverter current is observed when there are perturbations in the grid voltage. This situation may be more common now as the grid becomes susceptible to overvoltage issues and as per IEEE

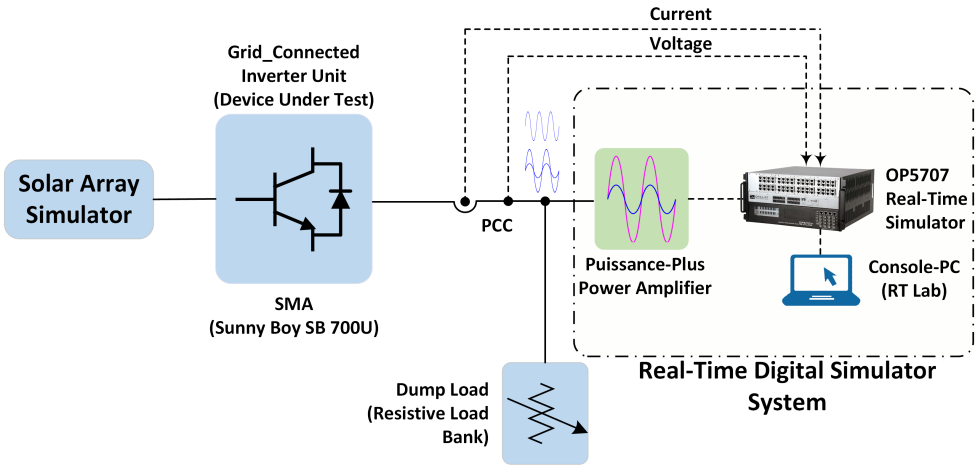

Figure 5.5. Experimental setup for system identification. The GFL inverter is probed through a power amplifier unit controlled through an Opal-RT RTS.

1547 standard the inverters can have voltage ride-through capabilities. To emulate this scenario, the amplitude of the power amplifier's output voltage is varied through the Opal-RT RTS. This emulates over/under-voltage conditions in the grid. The corresponding output voltage at the PCC and the current supplied by the inverter are logged through the Opal-RT system. The voltage and current measurements are fed into the console personal computer (PC), where the dynamics model of the inverter will be identified using SysId algorithm as described in Section 4.2.

5.5.2 Experimental Setup for 10 kW FSI Inverter

A PHIL arrangement can be used to test GFL inverters in a varying voltage conditions. Here, the equipment under test is a commercial three-phase 10 kW FSI which has GSFs, and TF model is to be determined when it is operating in Volt-VAr mode. The experimental setup to identify the dynamics of an FSI with GSFs is shown in Fig. 5.6.

The OP5707 RTS from Opal-RT technology was employed in PHIL. The RTS and power amplifier, in combination with the console PC, were used to emulate grid voltage of

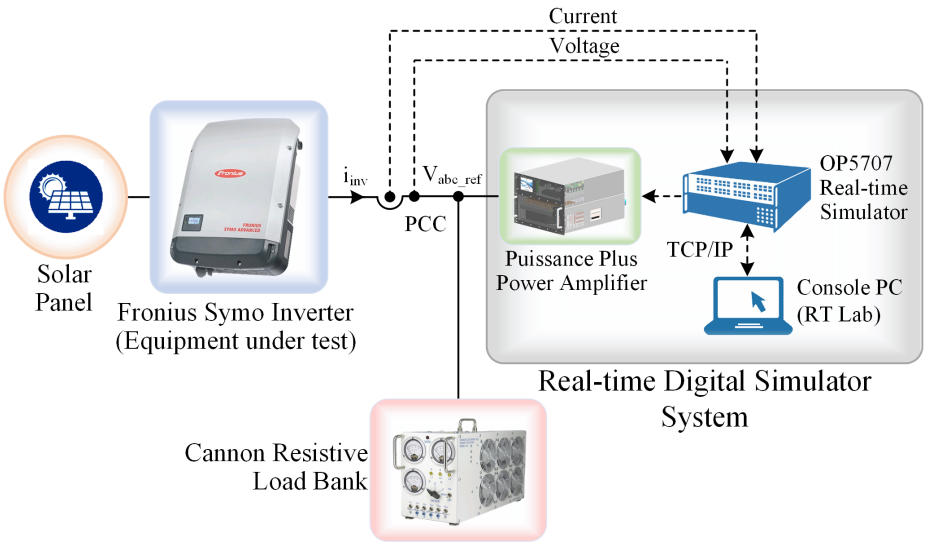

Figure 5.6. Experimental setup to determine TF of FSI operated in Volt-VAr mode. The FSI is probed through a power amplifier unit controlled through an Opal-RT RTS.

varied output magnitude. The voltage amplitude at PCC was perturbed by the power amplifier and the current injected by FSI to the grid was recorded for the complete normal operating range (0.88 p.u. – 1.1 p.u.) to capture the dynamics of Volt-VAr mode. The MATLAB/Simulink model to generate varying voltage amplitude at power amplifier output terminals was designed in the console PC interfaced with OP5707 and was built, compiled, and loaded into OP5707 RTS. Transmission Control Protocol (TCP) and the Internet Protocol (IP) were used to communicate between the console PC and OP5707 RTS. RTS sent the small analog probing signal to the power amplifier input terminals and the amplified probing signal was generated at the output terminals of power amplifier. The DC side of the FSI was powered by a PV system available on the microgrid research lab building at South Dakota State University. A Cannon resistive dump-load was connected at PCC to consume power generated by the PV system and to protect reverse power flow to the power amplifier. The settings of FSI and load are given in Table 5.3.

Table 5.3. Load and FSI Parameters.

Parameter	**Value**
Resistive load	1 kW
FSI Rating	10 kW
Q_1, Q_2, Q_3, and Q_4	3.3, 0, 0, and -3.3 kVA resp.
V_L, V_1, V_2, V_3, V_4, and V_H	0.88, 0.92, 0.98, 1.02, 1.07, and 1.1 p.u. resp.[67]

5.5.3 Experimental Setup for Two-phase 5 kW SMA Inverter

To test inverters under IEEE 1547-2018 standard voltage and frequency settings, a PHIL setup can be used. The test equipment used in this experiment is a commercial two-phase 5 kW SMA inverter, whose dynamic model is to be determined when it is operating in Volt-Watt and Freq-Watt modes. The experimental setup to determine the dynamics of an SMA with GSFs is depicted in Fig. 5.7.

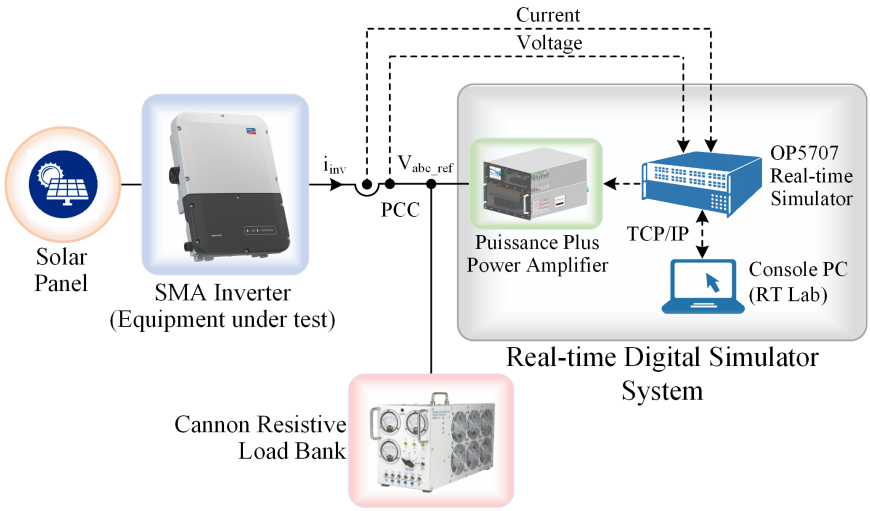

Figure 5.7. Experimental setup to determine TF of SMA operated in Volt-Watt and Freq-Watt mode. The SMA is probed through a power amplifier unit controlled through an Opal-RT RTS.

The experimental setup utilizes a PV system (located on the roof-top of the South Dakota State University (SDSU) microgrid research lab building to supply power to the

inverter DC side), two-phase 5 kW SMA inverter, Puissance Plus Power Amplifier, OP5707 RTS from Opal-RT technology, Cannon Resistive Load Bank and Console PC for testing PHIL experiment. The RTS and power amplifier, in combination with the console PC, is used to perturb the voltage and frequency at the PCC. In addition, at PCC, a Cannon Resistive Load Bank is connected to utilize the PV power while protecting against reverse power flow to the power amplifier.

The console PC is used to design the probing signal for perturbing the voltage and frequency amplitudes at the PCC. The probing signal design is carried out by carefully considering probing signal design criteria. The MATLAB/Simulink model of the probing signal is then built, compiled, and loaded into the OP5707 RTS from the console PC interfaced with the OP5707 for generating variable voltage and frequency amplitude at power amplifier input terminals. The power amplifier, which receives a small analog probing signal from RTS at its input terminals, produces an amplified probing signal at its output terminals. The perturbed voltage and frequency amplitude at PCC by the power amplifier and the current injected by SMA to the grid are recorded for the complete operating range for capturing the dynamics of the inverter. For capturing the dynamics of an inverter operating in either Volt-Watt or Freq-Watt mode, the corresponding mode of an inverter is activated by selecting Volt-Watt or Freq-Watt settings in the inverter. The logged corresponding output voltage/frequency at the PCC and the current injected from the inverter are passed through the Opal-RT system. The SysId algorithm as described in Section 4.2 is used to find the dynamic model of the inverter.

5.6 Results and Analysis

5.6.1 Result and Analysis of 700 W SMA Inverter

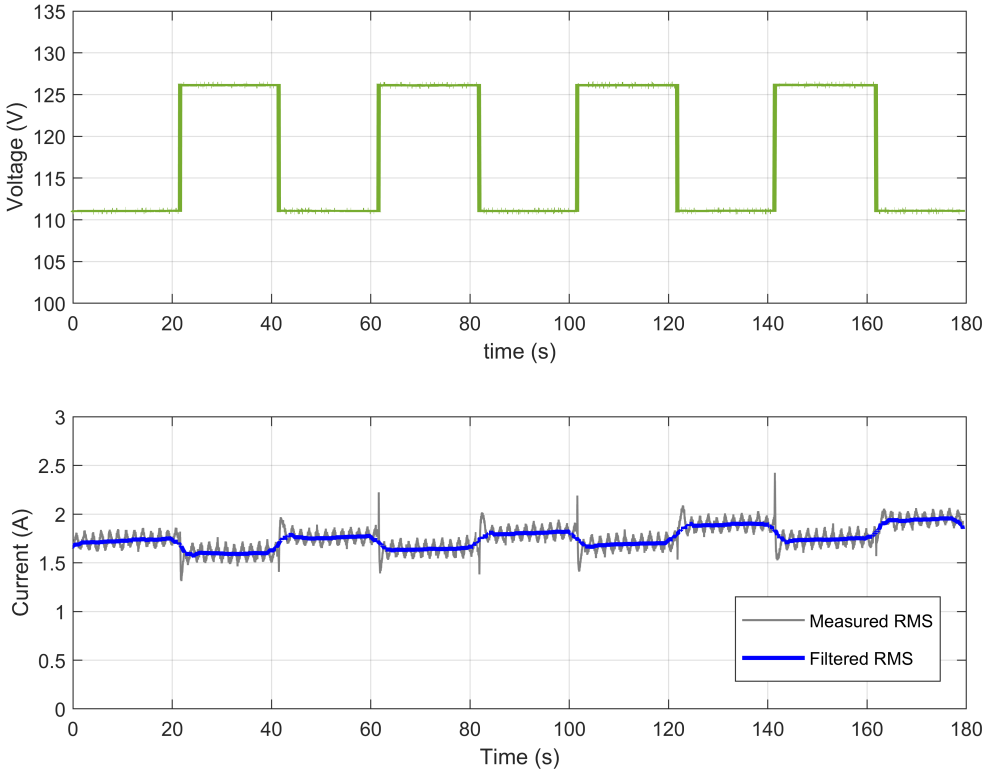

Figure 5.8. Response of inverter output current with step change in grid voltage.

Figure 5.8 shows the response of the SMA inverter to the changes in the grid voltage. The root-mean-square value of both the voltage and current signal is shown. A median filter was applied which works as a non-linear digital filter and smooths the array of sampled data, preserves edges while eliminating unwanted noise signals. Furthermore, to get a more accurate model, mean of both current and voltage measurements are removed. This allows the focus of the identification to be on the actual fluctuations due to the perturbations rather than unwanted trends in the data. For cross-validation purposes, the dataset is split into a training set to compute the unknown poles and zeros and testing

set to validate the derived model. The training dataset obtained after proper pre-processing is illustrated in Fig. 5.9.

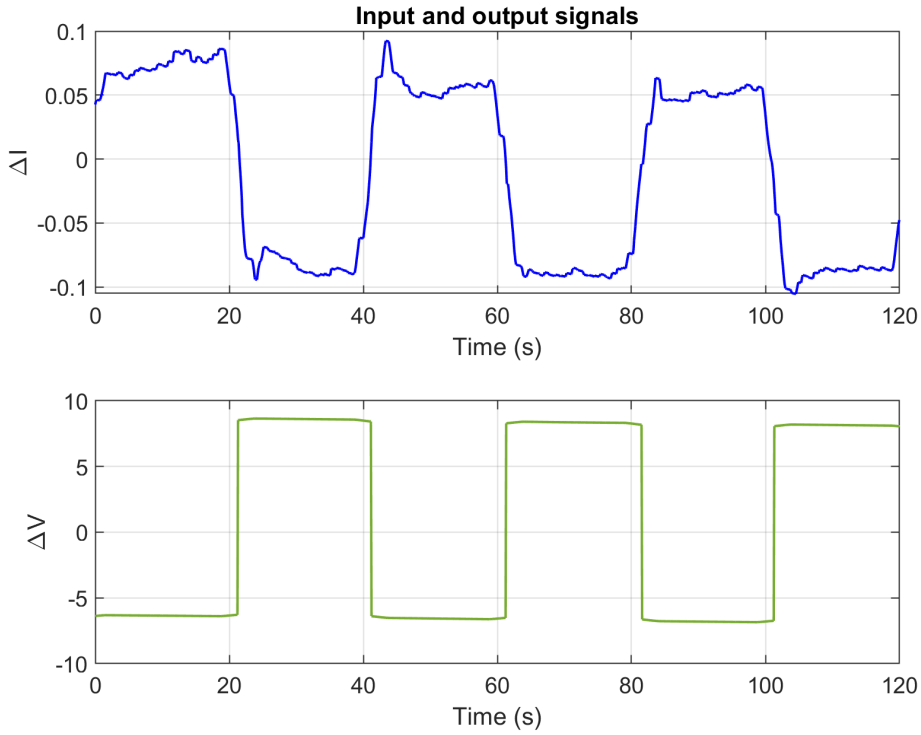

Figure 5.9. Training dataset obtained after pre-processing the measured current and voltage signals.

The possibility of getting a better fit through higher-order models was also explored. For this, a system with 3-poles and 1-zero; and 3-poles and 2-zeros were analyzed. Table 5.4 lists the various models that were fitted along with a metric that demonstrate the GoF for training and testing data. A TF with 2-poles and 1-zero seems to provide the *best* fit. The GoF was highest for this case with both the testing and training dataset. Furthermore, the Akaike's FPE metric is also the least from this case compared to the other two cases. Increasing the number of poles from 2 to 3 in the second case slightly reduced the GoF. Similarly, increasing both poles and zeros as in the third case slightly increases the GoF against the testing dataset. Based on this analysis the following

second-order TF was identified to be suitable:

$$\hat{G(s)} = \frac{\Delta i_{inv}(s)}{\Delta v_g(s)} = \frac{-0.02113s - 9.334 \times 10^{-4}}{s^2 + 2.104s + 0.1133} \tag{5.1}$$

Figure 5.10 illustrates a schematic diagram for implementing the TF model of a 700W SMA inverter in EMT simulation using Opal-RT. The purpose is to validate the TF model obtained through the SysId Toolbox. To assess the accuracy of the TFs, the inverter was probed using a square probing signal in conjunction with the Puissance Plus Power Amplifier. This probing signal was applied in parallel with the inverter's TF. The reference voltage amplitude at the PCC is denoted as V_{abc_ref}. The output current generated by the 700W SMA inverter and injected into the power amplifier was processed through the $abc - dq0$ block to get the quadrature axis current, i_{invq}. Here, V_{abc_ref} was converted into the $dq0$ coordinate system, with only the d-component (V_d) being utilized, as it corresponds to the voltage amplitude. Prior to inputting it into the TF, the mean value of V_d was removed. The output of the TF provided an estimate of the current. The mean value of the sensed current (i_{invq}) was added to the estimated current (i_{q_est}) to obtain the actual estimated current (i_{q_tf}) from the TF block. The fit percent was then calculated, aiming to assess the accuracy of the TF model.

The performance of this model is also illustrated in Fig. 5.11 by comparing the simulated model against the measured data. The simulated model is the response that is computed based on the fitted model, using the test data as the input. Ideally, the simulated model should be very close to the measured data for a good model fit. The fit obtained in this case was 76.77% which is slightly on the lower side. The dotted lines illustrate the

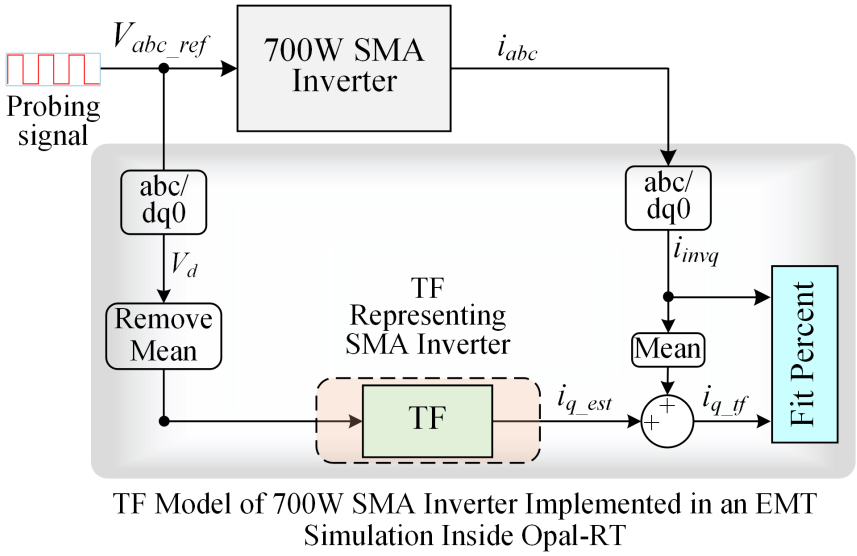

Figure 5.10. Schematic diagram to validate the TF obtained from SysId Toolbox for 700W SMA inverter.

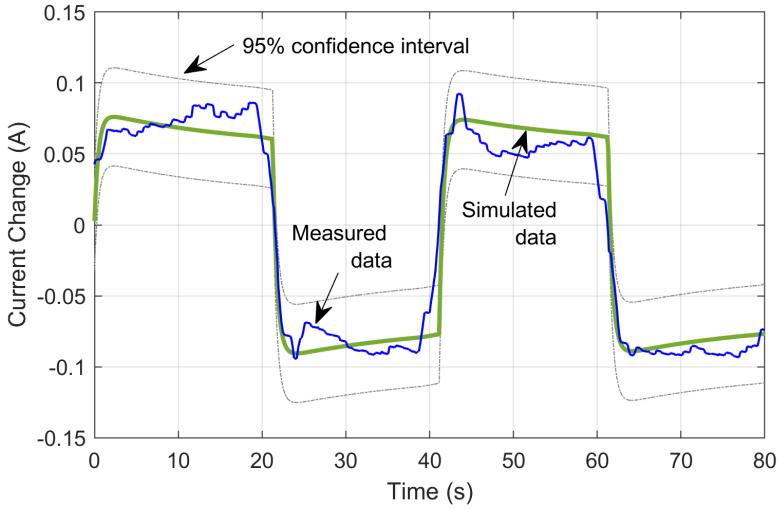

Figure 5.11. Measured versus simulated output of the fitted TF along with the 95% confidence interval of the estimate.

95% confidence interval of the estimates. The confidence interval represents the range of output values having 95% probability of being the true response of the system.

5.6.2 Result and Analysis of 10 kW FSI Inverter

The TF of the FSI which operates in Volt-VAr mode is obtained from the SysId toolbox and the results of the GoF obtained by comparing the actual response of an FSI

Table 5.4. Summary of TF models identified through the SysId Toolbox.

Model Order	Model Coefficients	Fit to Training Data	Fit to Test Data	FPE
$n = 2$ $m = 1$	b_1 = -0.02113 b_0 = -9.334$\times 10^{-4}$ a_2 = 1.000 a_1 = 2.104 a_0 = 0.1133	76.77%	74.24%	3.118$\times 10^{-4}$
$n = 3$ $m = 1$	b_1 = -0.06635 b_0 = 1.6$\times 10^{-4}$ a_3 = 1.000 a_2 = 4.344 a_1 = 6.701 a_0 = 0.012222	74.2%	72.45%	3.85$\times 10^{-4}$
$n = 3$ $m = 2$	b_2 = -0.02651 b_1 = -9.392$\times 10^{-3}$ b_0 = -0.1478 a_3 = 1.000 a_2 = 3.024 a_1 = 6.661 a_0 = 14.69	76.17%	73.92%	3.28$\times 10^{-4}$

and that from the TF are analyzed in this section.

In PHIL test condition, regions R_1, R_2, R_3, R_4, and R_5 were divided into 3, 7, 3, 5, and 2 ranges based on the voltage parameters (listed in Table 5.3) defined for Volt-VAr mode in the updated IEEE 1547-2018 standard. Middle range data $(r_{12}, r_{24}, r_{32}, r_{43})$ were used to obtain the TF for R_1 up to R_4 regions and range 1 data (r_{51}) was used in region R_5 for all four probing signals. Here, the overall dynamics of the FSI were represented using the second-order TF because the GoF for second-order TF was found to fulfill both accuracy and computational complexity requirements.

In contrast to other regions, the Volt-VAr mode is deactivated in the R_3 region, which implies the FSI will not inject/absorb any reactive power to/from the grid, resulting

in no significant GFL inverter dynamics. Hence, region R_3 is not considered in the analysis.

Different probing signals were used in Fig. 5.6 to determine the TFs of FSI operating in Volt-VAr mode. Fig. 5.12 shows the logarithmic Sq-Chirp signal as a reference input probing signal to change the PCC voltage. TF(Sq), TF(Sine), TF(Sq-Chirp), and TF(Sine-Chirp) were the different TFs obtained from the respective probing signals which include TF for each region (except for R_3) resulting in sixteen TFs which is listed in Table 5.5.

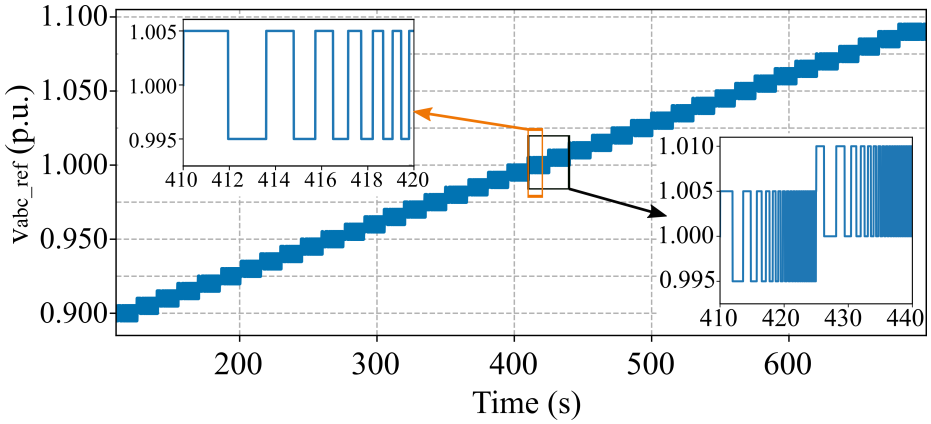

Figure 5.12. Logarithmic Sq-Chirp signal used to perturb the voltage at PCC.

Table 5.5. Summary of TF models for different regions with four different probing signals.

Regions	Transfer Function $(\frac{i_q}{V_d})$			
	TF(Sq)	TF(Sine)	TF(Sq-Chirp)	TF(Sine-Chirp)
R_1	$\frac{-5.8924s+811.87}{s^2+154.6s+9770.2}$	$\frac{-316.36s+12320}{s^2+12.61s+14420}$	$\frac{-4.84s+729.37}{s^2+151.5s+8060.5}$	$\frac{60.10s+1025.70}{s^2+735s+12500}$
R_2	$\frac{-8.96s+593.44}{s^2+32.13s+466.3}$	$\frac{-894.63s+44688}{s^2+2262.2s+32700}$	$\frac{-8.57s+559.64}{s^2+29.98s+461.03}$	$\frac{5.96s+278.09}{s^2+21.169+210.99}$
R_4	$\frac{-12.95s+639.09}{s^2+32.66s+490.65}$	$\frac{-71.29s+5102.6}{s^2+280.76s+3573.6}$	$\frac{-10.77s+615.1}{s^2+32.18s+466.91}$	$\frac{-25.8s+1023.6}{s^2+48.24s+792.67}$
R_5	$\frac{5.88s-787.65}{s^2+239s+13127}$	$\frac{20.87s-2211.5}{s^2+721.48s+36696}$	$\frac{3.07s-648.12}{s^2+163s+10851}$	$\frac{36.4s-5807}{s^2+2440+98199}$

Fig. 5.13 depicts a schematic diagram to implement the TF model of a 10 kW FSI

in EMT simulation inside Opal-RT and validate the TF model acquired via SysId. To validate the accuracy of the TFs, the inverter was excited through the Puissance Plus Power Amplifier with the same probing signal in parallel with its TFs. V_{abc_ref} is the reference voltage amplitude at PCC. The output current injected to the power amplifier by the inverter was passed to $abc-dq0$ block to only obtain quadrature axis current, i_{invq}. Here, V_{abc_ref} was converted to $dq0$ component, and only the d-component (V_d) was used as it is associated with the voltage amplitude. The mean value of V_d was removed before feeding to the TF of different regions. The output of the TF was the estimated current which was inputted to the selector block. The selector block chose the correct estimated current based on the per-unit value of voltage V_{d_pu}. Mean value of sensed current (i_{invq}) was then added in the estimated current (i_{q_est}) to get actual estimated current (i_{q_tf}) from the TF block. The GoF based on NRMSE was then calculated to compare the fit percent.

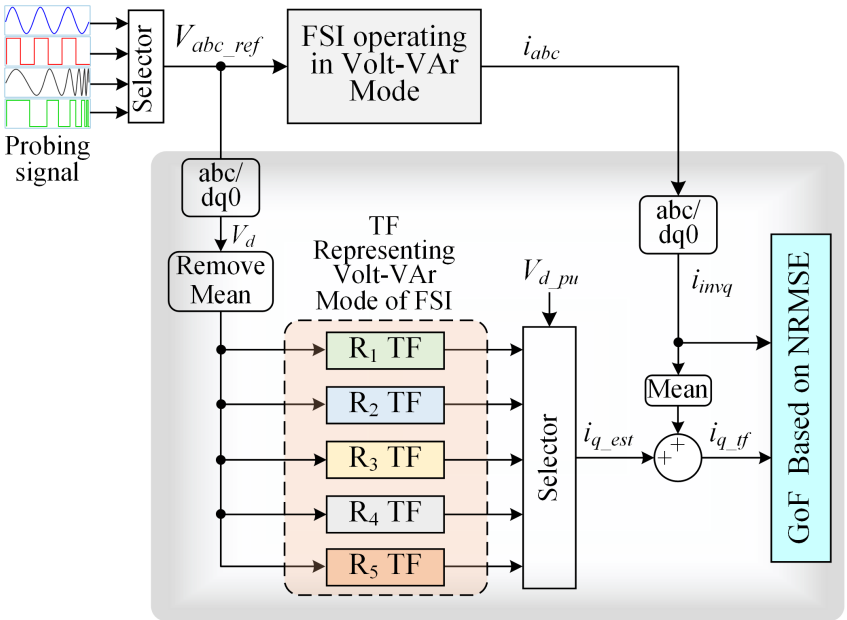

Figure 5.13. Schematic diagram to validate the TF obtained from SysId Toolbox for 10 kW FSI.

The GoF of TF identified from SysId toolbox available in MATLAB for four probing signals at different regions (except R_3) are shown in Fig. 5.14. It shows that for all regions, TF obtained from the Sq-Chirp probing signal performs the best. The reason for the high fit percentage with the Sq-Chirp signal is due to the availability of higher frequency components that can capture the dynamics of FSI.

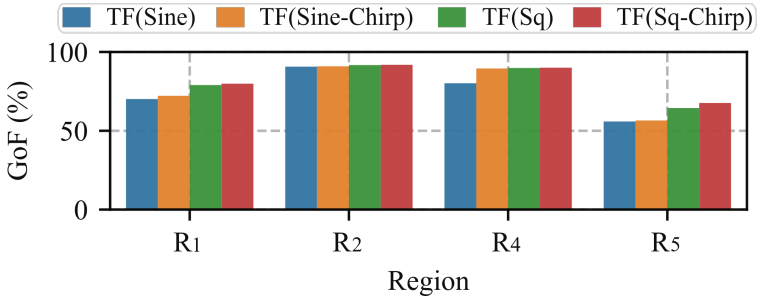

Figure 5.14. GoF of two poles and one zero TF model identified from the SysId toolbox. R_3 is not shown as the GSF is not active in that region.

To cross-validate the performance of the probing signal, we excite the derived TFs by all probing signals. Fig. 5.15 shows the response of an FSI when all the TFs obtained from all probing signal is perturbed by the Sq-Chirp signal. Here, i_{invq} is actual response of an FSI and $i_{invq\_TF(sq)}$, $i_{invq\_TF(sine)}$, $i_{invq\_TF(sq-chirp)}$, and $i_{invq\_TF(sine-chirp)}$ are the output response of the respective TFs. We performed a similar test for all other probing signals but the response is not shown in the chapter, overall fit percent is presented.

Fig. 5.16 shows the performance comparison of all the probing signals when fed to all the TFs. It shows that for the regions TF obtained from Sq-Chirp signal has the highest fit percentage. For R_2 and R_4 fit percentage is greater than 95% and R_1 and R_5 has fit percent greater than 75% and 50% respectively. Lower fit in R_1 and R_5 is due to the activation of Volt-VAr mode saturation i.e PV can only inject/absorb constant reactive power regardless of decrease/increase in voltage (below V_1 or above V_4).

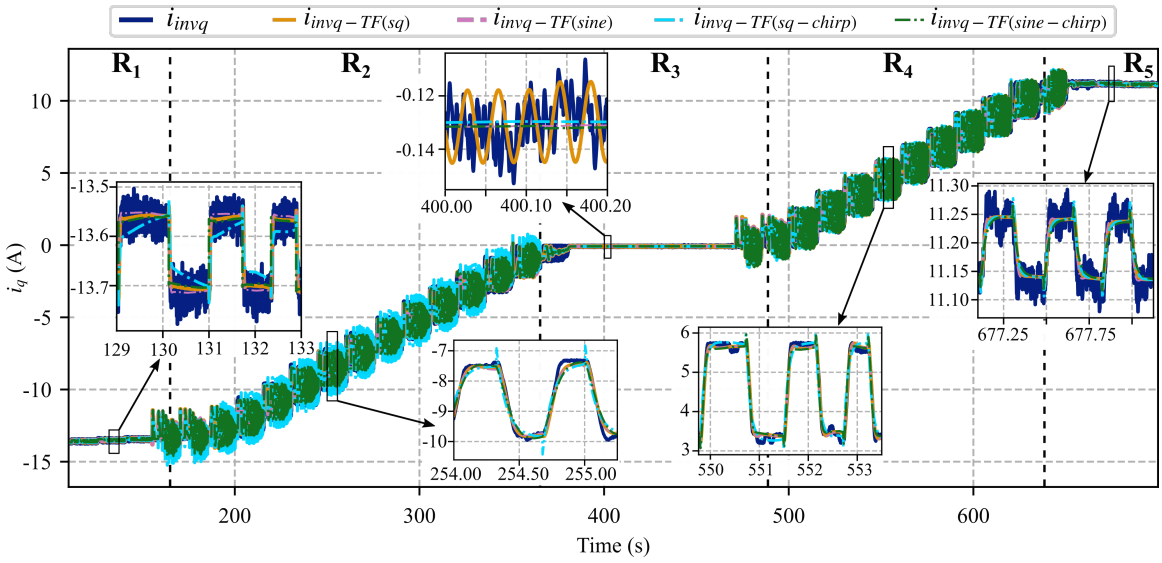

Figure 5.15. Response of an FSI when all the TFs from each signal is perturbed by Sq-Chirp.

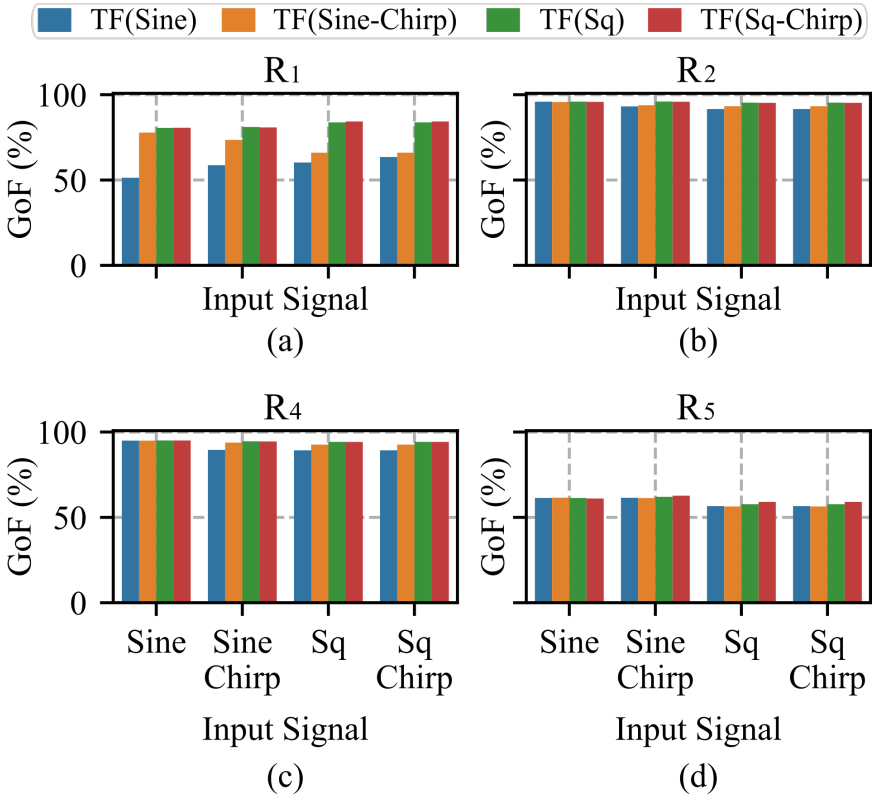

Figure 5.16. Performance comparison of all the probing signals when used to perturb all the TFs.

5.6.3 Result and Analysis of Two-phase 5 kW SMA Inverter

The effect of varying irradiance in the data-driven modeling of inverter dynamics during activation of Volt-Watt and Freq-Watt modes will be analyzed in this section. GoF will be calculated for each case using the NRMSE techniques to validate the analysis outcome. In addition, the second-order TF will be utilized to represent the overall dynamics of the SMA inverter as it can satisfy both accuracy and computing complexity requirements [78].

Case-1: Volt-Watt Mode

Table 5.6. Load and SMA Inverter Parameters.

Parameter	**Value**
Resistive load	1 kW
SMA Rating	5 kW
Volt-Watt Setting	
P_1 and P_2	3, 0, and 0 kW resp.
V_1, V_2, and V_H	1.045, 1.085, and 1.095 p.u. resp.
Freq-Watt Setting	
P_1 and P_2	3, 0, and 0 kW resp.
F_1, F_2, and F_H	1.0083, 1.033, and 1.037 p.u. resp.

The Volt-Watt mode of the SMA inverter is activated according to the Volt-Watt setting specified in Table 5.6. Following the activation, the voltage amplitude at PCC is perturbed by using the logarithmic square chirp signal (Fig. 5.18), which varies the voltage amplitude of PCC from 1 - 1.095 p.u., respectively. The actual response of the inverter (i_{invd}) after perturbation is noted and depicted in Fig. 5.17 (a-c). From the initial time to 230 s, there is a linear decrement of i_d with a slight slope. It is because the inverter is set to operate in constant active power mode, and at the same time, the PCC voltage amplitude is increasing, which leads to a situation of constant power and increasing

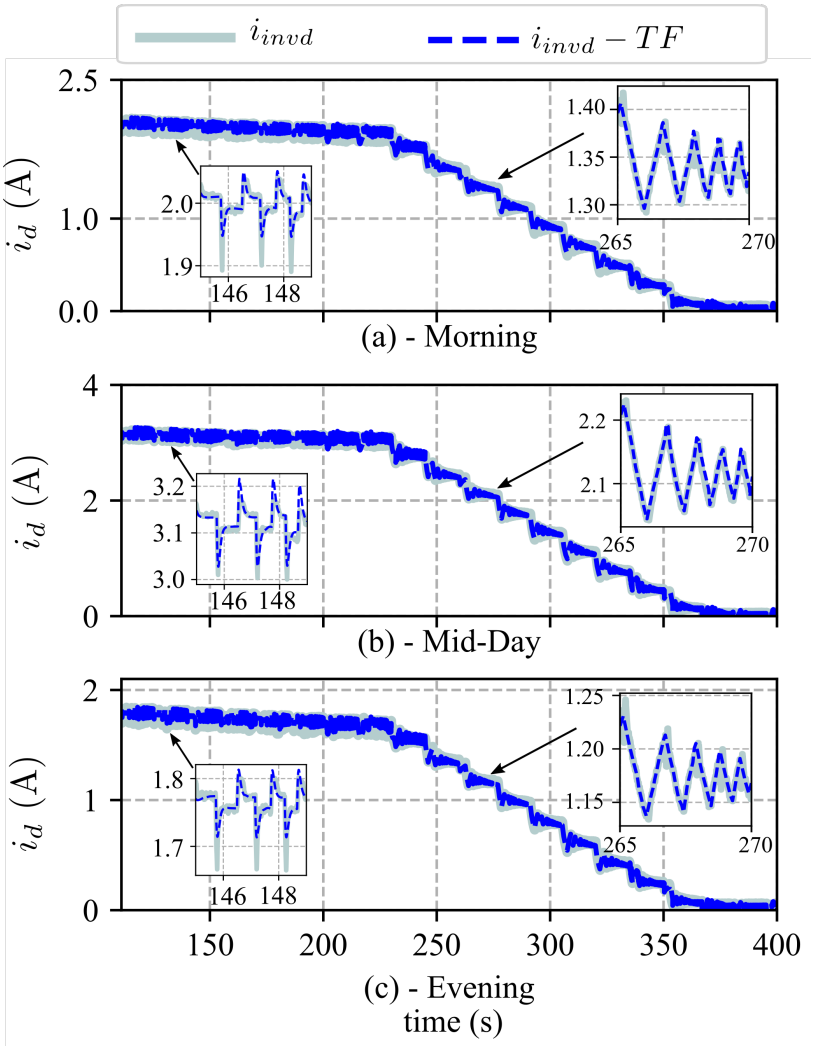

Figure 5.17. i_{invd} from (a)-(c) is the actual response of the inverter when perturbed by a logarithmic signal while activating Volt-Watt mode during three time periods of the day and $i_{invd} - TF$ from (a)-(c) is the response of an SMA inverter when adjusted Morning TF (adjusted Morning TF= $\frac{\text{dc-gain of Morning TF}}{\text{dc-gain of Mid-day TF}} \times$ Mid-day TF), Mid-day TFs and, adjusted Evening TF (adjusted Evening TF= $\frac{\text{dc-gain of Evening TF}}{\text{dc-gain of Mid-day TF}} \times$ Mid-day TF), is perturbed by Sq-chirp signal respectively.

voltage and, accordingly, a decrease in current. At 230 s, the Volt-Watt mode of the inverter gets activated (PCC voltage amplitude exceeds 1.045 p.u.), and the inverter starts reducing the active power injection as per the defined gradient of Volt-Watt mode until 365 s (where PCC voltage amplitude reaches 1.085 p.u.). After 365 s, PCC voltage

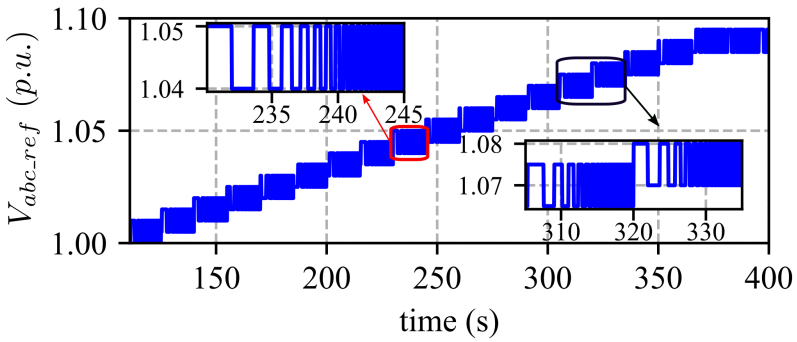

Figure 5.18. Logarithmic Sq-Chirp signal used to perturb the voltage at PCC.

amplitude surpasses 1.085 p.u. and exceeds the specified nominal voltage threshold, leading to zero active power injection from the inverter ($P_2 = 0$).

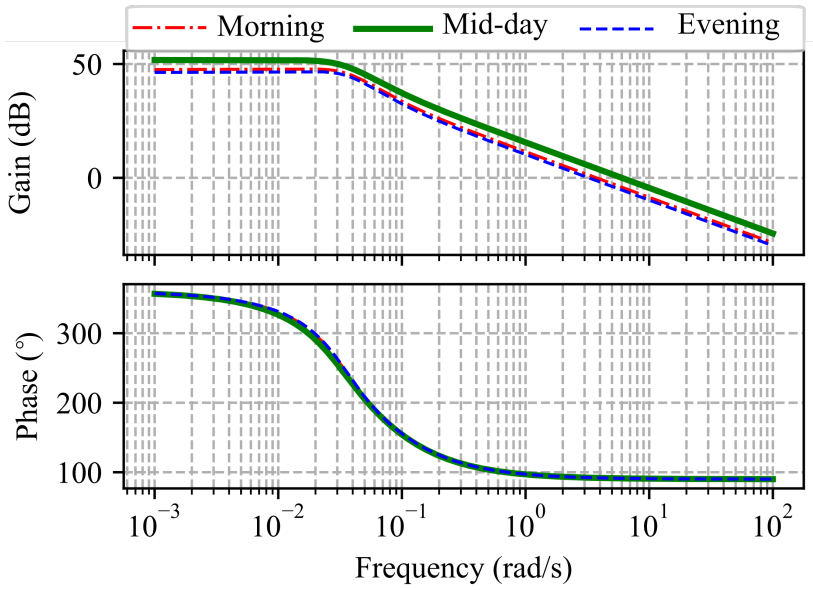

Figure 5.19. Bode response of TF model of R_2 obtained during three different periods of the day while activating Volt-Watt mode before adjusting the DC-gain in TF model of morning and evening.

For modeling inverter dynamics, at first mid-day dataset is used and the concept of partitioned modeling of Volt-Watt as explained in Section 5.3 is employed where based on the voltage settings (listed in the Table 5.6), regions R_1, R_2, and R_3 are divided into 8, 9, and 3 smaller ranges, respectively. The mid-range data, i.e., (r_{13}, r_{24}, and r_{31}) are used to

obtain the TF of the respective regions. The analysis of region R_3 is disregarded in this case as the Volt-Watt mode of the SMA inverter gets turned off in that region, preventing SMA from absorbing/injecting any active power. At first, the SysId algorithm is developed and is employed, which utilizes 70% of (V_{abc_ref} and its corresponding mid-day response i_d) as input and output data, respectively. These data are then utilized to obtain the TF model of the inverter dynamics. Here, mid-day data are utilized to obtain the TF with the presumption that midday irradiance will remain constant and the model obtained will be more accurate- unlike morning and evening, where irradiance gets fluctuated.

DC-gain of the system is defined as the gain of the system when the frequency is zero. The DC-gain of the TF can be determined by comparing the given TF with the standard time constant form which is represented below:

$$G(s) = \frac{K \times (1+s\tau_1)(1+s\tau_2)(1+s\tau_3).....(1+s\tau_n)}{s^n(1+s\tau_1^{'})(1+s\tau_2^{'})(1+s\tau_3^{'}).....(1+s\tau_n^{'})}$$

Here, K is the of the system. τ and $\tau^{'}$ are the time constants of the system and n is the order of the system.

In another way, DC-gain can be obtained as [84]:

$$K = \lim_{s \to 0} \; s^n G(s). \tag{5.2}$$

The mid-day model coefficient of R_1 and R_2 is tabulated in Table 5.7. The obtained TF is then cross-validated by employing the remaining 30% data. The corresponding response ($i_{invd} - TF$) after cross-validation of TF is stacked with the actual

Table 5.7. Summary of TF models of three time periods of the day while activating Volt-Watt mode of inverter

Parts of Day	Model Coefficient of Region-1	Model Coefficient of Region-2
Morning	b_1 = -300.1 b_0 = -706.2 a_2 = 1 a_1 = 39.4 a_0 = 392.6	b_1 = -26.42 b_0 = 11.47 a_2 = 1 a_1 = 0.2852 a_0 = 0.4805
Mid-day	b_1 = -347.6 b_0 = -866.1 a_2 = 1 a_1 = 42.4 a_0 = 383.9	b_1 = -37.69 b_0 = 16.96 a_2 = 1 a_1 = 0.3027 a_0 = 0.4382
Evening	b_1 = -295.9 b_0 = -690.2 a_2 = 1 a_1 = 38.60 a_0 = 397.1	b_1 = -20.35 b_0 = 10.11 a_2 = 1 a_1 = 0.2822 a_0 = 0.4897

response of the inverter as shown in Fig. 5.17 (b), which shows similarity to a great extent. The GoF of the estimated TF is then calculated, which is 87.16% for R_1 and 96.35% for R_2, respectively. The morning and evening datasets are fed into the estimated mid-day TF for analyzing the impact of varying irradiance in inverter dynamics. However, in each case of morning and evening, the output response shows that it requires a certain DC-gain adjustment in the mid-day TF model. For further validation of the DC-gain requirement, the TF model from the morning and the evening dataset is derived following the same procedure as in mid-day for obtaining the DC-gain adjustment value. The model coefficient for each scenario is tabulated in Table 5.7. The bode response of the obtained TF of R_2 for each scenario of the morning, mid-day, and evening are shown in Fig. 5.19. Due to the space constraints and primary emphasis on the slope area of Fig. 5.17, the bode response of R_1 is discarded. Bode's response shows that the model obtained during

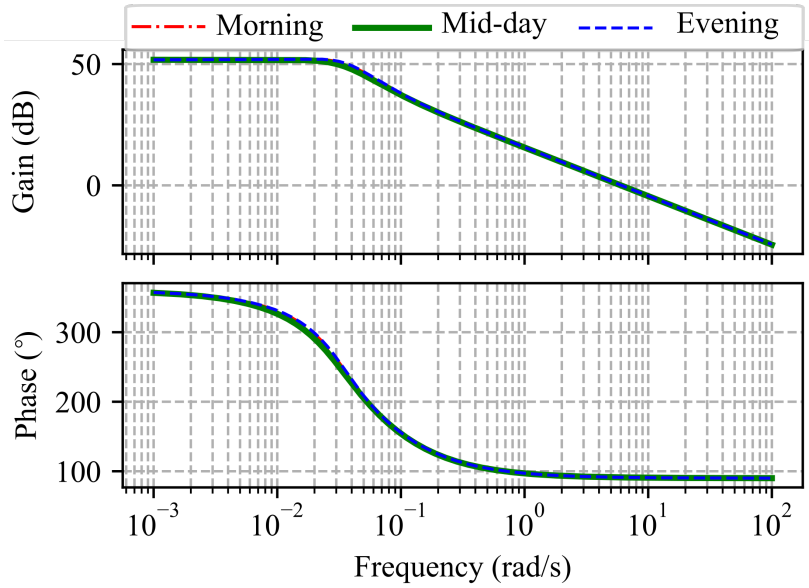

Figure 5.20. Bode response of TF model of R_2 obtained during three different periods of the day while activating Volt-Watt mode after adjusting the DC-gain in TF model of morning and evening.

morning and evening requires certain DC-gain adjustments. The DC-gain of each model is obtained following Equation 5.2 (i.e., $\frac{b_0}{a_0}$) and found to be -1.79, -2.2 and -1.73 for the morning, mid-day, and evening respectively for R_1. Similarly, the DC-gain of R_2 is found to be -23.87, -38.71, and -20.65 for the morning, mid-day, and evening respectively. Taking reference of the mid-day model, the model obtained during the morning is multiplied with ($\frac{-2.2}{-1.79} = 1.23$), and the model obtained during the evening is multiplied with ($\frac{-2.2}{-1.73} = 1.27$) during DC-gain adjustment of a model of R_1. Similarly, taking reference of the mid-day model, the model obtained during the morning is multiplied with ($\frac{-38.71}{-23.87} = 1.62$), and the model obtained during the evening is multiplied with ($\frac{-38.71}{-20.65} = 1.87$) during DC-gain adjustment of the model of R_2. The bode plot of R_2 of each model obtained during the morning, mid-day, and evening after DC-gain adjustment is shown in Fig. 5.20, which coincides with each other. The mid-day model of R_1

multiplied with $\frac{1}{1.23}$ and the mid-day model of R_2 multiplied with $\frac{1}{1.62}$ is employed for feeding the morning data, and the output response is shown in Fig. 5.17 (a) and similarly the mid-day model of R_1 multiplied with $\frac{1}{1.27}$ and mid-day model of R_2 multiplied with $\frac{1}{1.87}$ is employed for feeding the evening data and the output response is shown in Fig. 5.17 (c) respectively. The GoF is then calculated, which is 82.37% and 93.71% for R_1 and R_2, respectively, in the morning scenario and 81.76% and 93.71% for R_1 and R_2 respectively in the scenario of the evening. Here, from this analysis, it can be concluded that the dynamic model of the inverter remains the same throughout the day; however, the dynamic model has to undergo DC-gain adjustment during the morning, mid-day, and evening, and the DC-gain depends on the irradiance (as DC-gain varies over time so do irradiance) and is a function of the irradiance.

Case-2: Freq-Watt Mode

Similar to Case-1, the setting of the Freq-Watt mode of the inverter is made accordingly to the Freq-Watt setting indicated in Table 5.6, and then the frequency at PCC is perturbed by using the logarithmic square chirp signal as a probing signal (Fig. 5.22) at three periods of the day. The actual response of the inverter which is indicated by i_{invd} after perturbation is noted and is depicted in Fig. 5.21 (a-c). It can be revealed that noise is incorporated into the actual response. Due to the range limitation of frequency (60 Hz–62 Hz), the amplitude of the perturbation signal is taken as 0.001 p.u. (i.e., 0.6 Hz), which does not fulfill SNR criteria (as opposed to Volt-Watt mode, where the amplitude of the perturbation signal is 0.01 (1.697 V) and SNR is fulfilled) and results in noise. Hence, the noise frequency, which varies from 119 Hz to 123 Hz, is noted, and a band stop filter that stops the noise in these frequency ranges is designed and implemented. The filtered output

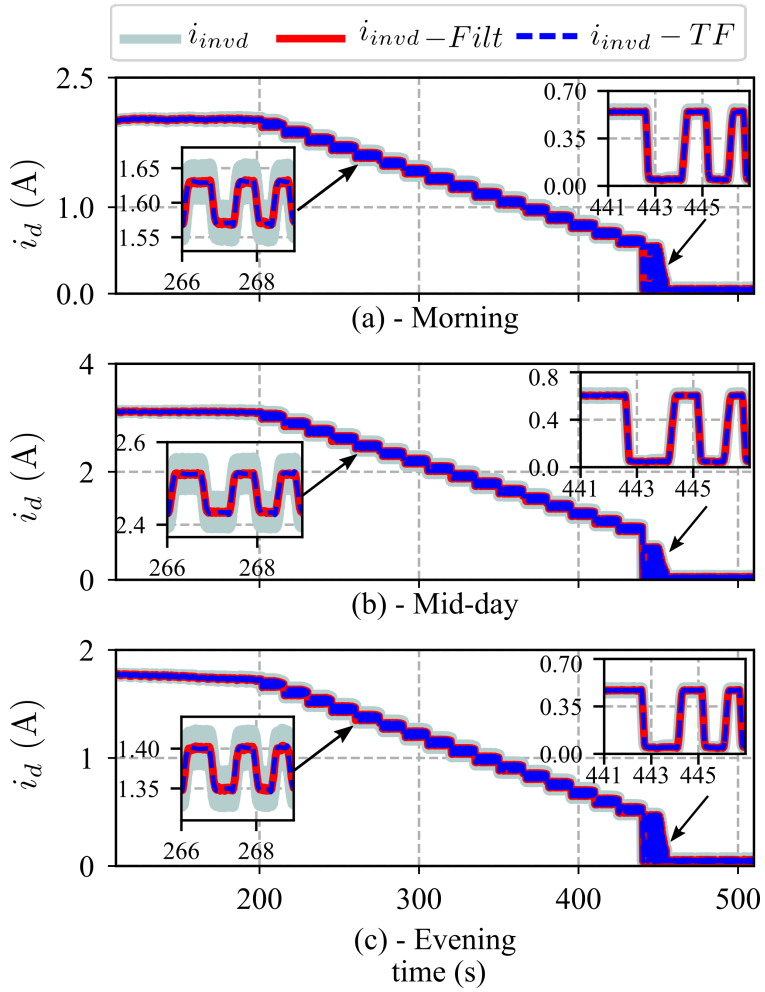

Figure 5.21. i_{invd} from (a)-(c) is the actual response of the inverter when perturbed by a logarithmic signal while activating Freq-Watt mode during three time periods of the day, $i_{invd}-Filt$ from (a)-(c) is the filtered response after incorporating band-stop filter and $i_{invd}-TF$ from (a)-(c) is the response of an SMA inverter when adjusted Morning TF, Mid-day TFs and, adjusted Evening TF, is perturbed by Sq-chirp signal respectively.

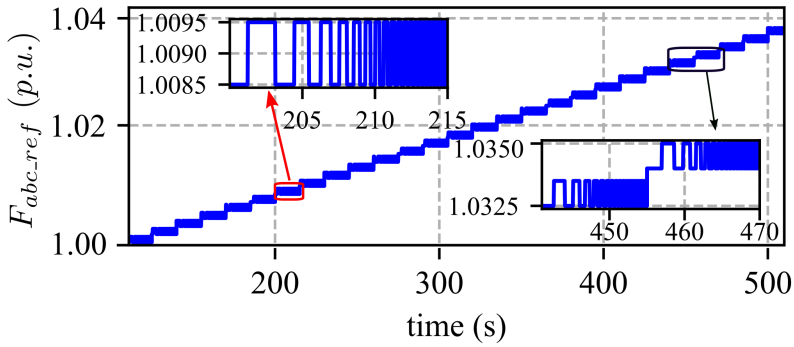

Figure 5.22. Logarithmic Sq-Chirp signal used to perturb the frequency at PCC.

response of the inverter, which is represented as $i_{invd} - Filt$ is depicted in Fig. 5.21 (a-c) respectively. It can be seen that after a time period of 200 s, the Freq-Watt mode of the inverter gets activated (perturbed frequency exceeds 1.008 p.u. (60.5 Hz)). The inverter decreases the active power injection accordingly to the defined gradient of Freq-Watt mode until 455 s (perturbed frequency reaches 1.033 p.u. (62 Hz)). Moreover, after exceeding 455 s, active power injection from the inverter becomes zero ($P_2 = 0$) as the perturbed frequency exceeds 1.033 p.u. (62 Hz) and exceeds the specified nominal frequency threshold [Freq-Watt setting]. There is a sharp transition between 440-455 s, mainly because, as indicated in Fig. 5.22 frequency fluctuates between 1.0325 p.u. (61.95 Hz) and 1.0335 p.u. (62.01 Hz). It means the inverter tries to inject certain active power at 61.95 Hz and zero active power after exceeding 62 Hz, giving rise to that transition where the proposed method of the partitioned modeling approach is applied for the SysId of that region. For modeling of inverter dynamics, based on the frequency settings (listed in the Table 5.6), regions R_1, R_2, and R_3 are divided into 7, 10, and 2 smaller ranges respectively during PHIL test condition. In the case of Freq-Watt mode, the analysis of the regions R_1 and R_3 will be discarded, as the SMA inverter will prevent absorbing/injecting any active power in those regions. To obtain the TF and cross-validate the estimated TF, Freq-Watt mode also incorporates the SysId toolbox, similar to Volt-Watt mode, and utilizes partitioning data into training and validation data. Training data is used to obtain the mid-day model, whose coefficient is tabulated in Table 5.8. The response during cross-validation of mid-day TF, which is indicated by $(i_{invd} - TF(sq-chirp))$ in Fig. 5.21 (b) is stacked with the actual response of the inverter during activation of Freq-Watt mode, which shows similarity to a great extent. The GoF of the estimated TF is then calculated,

which is 95.34%. The morning and evening data are fed into the estimated mid-day TF for analyzing the effect of varying irradiance on inverter dynamics. However, for each case of morning and evening, the output response shows that it requires a certain DC-gain adjustment in the mid-day TF The TF model during morning and evening is derived to obtain the dc-gain value, whose model coefficient is tabulated in Table 5.8. The bode response of the obtained TF of R_2 is shown in Fig. 5.23, which reveals the requirement of DC-gain adjustment.

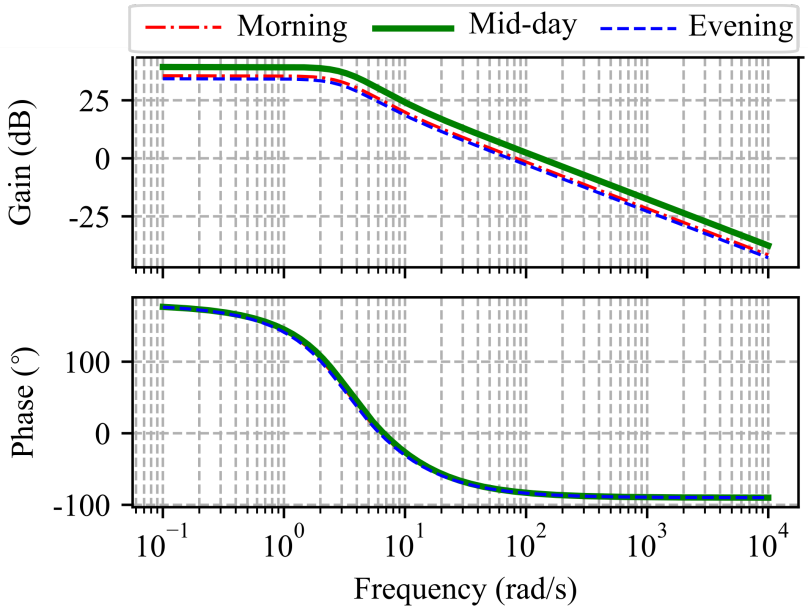

Figure 5.23. Bode response of TF model of R_2 obtained during three different periods of the day while activating Freq-Watt mode before adjusting the DC-gain in TF model of morning and evening.

The DC-gain of each model is calculated using Equation 5.2 (i.e., $\frac{b_0}{a_0}$) and is found to be -60, -90.98, and -51.77 for R_2 in the morning, mid-day, and evening, respectively. Using the mid-day model as a reference, the model obtained in the morning is multiplied by ($\frac{-90.98}{-60} = 1.51$), and the model obtained in the evening is multiplied by ($\frac{-90.98}{-51.77} = 1.757$) during the DC-gain adjustment of the R_2 model. The bode plot of R_2 of

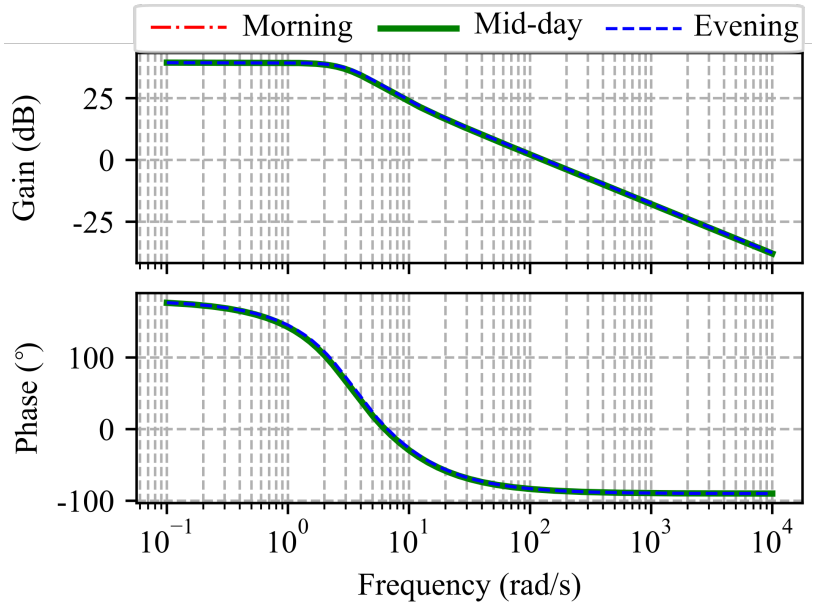

Figure 5.24. Bode response of TF model of R_2 obtained during three different periods of the day while activating Freq-Watt mode after adjusting the DC-gain in TF model of morning and evening.

Table 5.8. Summary of TF models of three time periods of the day while activating Freq-Watt mode of inverter

Parts of Day	Model Coefficient of Region-2
Morning	b_1 = 519.9, b_0 = -21970, a_2 = 1, a_1 = 28.71, a_0 = 365.6
Mid-day	b_1 = 1148, b_0 = -41690, a_2 = 1, a_1 = 32.54, a_0 = 458.2
Evening	b_1 = 452.4, b_0 = -18190, a_2 = 1, a_1 = 28.51, a_0 = 351.3

each model obtained after DC-gain adjustment in the morning, midday, and evening is shown in Fig. 5.24, which coincides with each other. The mid-day model of R_2 multiplied with $\frac{1}{1.51}$ is employed for feeding the morning data, and the output response is shown in Fig. 5.21 (a) and similarly, the mid-day model of R_2 multiplied with $\frac{1}{1.757}$ is employed for feeding the evening data, and the output response is shown in Fig. 5.21 (c), respectively. The GoF is then calculated, which is 93.14% for R_2 in the morning scenario and 91.32% for R_2 in the evening scenario. From this analysis, it can be concluded that the dynamic

model of the inverter remains the same throughout the day; however, the dynamic model undergoes DC-gain adjustment for the morning, mid-day, and evening. The DC gain depends on the irradiance and is a function of the irradiance.

Overall, Case-1 shows that the magnitude of response from the inverter (i.e., i_d) changes with varying irradiance (i.e., morning, mid-day, and evening have dynamics with different magnitudes), but the inverter dynamics remain the same each time period which appears to exhibit the same phenomenon in Case-2 as well. However, Case-1 and Case-2 also reveal that the inverter dynamics changes accordingly with the activation of various operating modes of the COTS inverter (i.e., Volt-Watt and Freq-Watt mode have different nature dynamics). From the above two cases, it can be concluded that the magnitude of the response from the inverter changes with a change in irradiance (active power dependency on irradiance); however, dynamics remain the same throughout the day. Nevertheless, if different modes of the inverter get activated, then the dynamics of the inverter vary accordingly. In addition, the dynamic model obtained has to adjust its DC gain accordingly during different periods and is dependent on irradiance.

Linear dependency of DC-gain of the model with irradiance

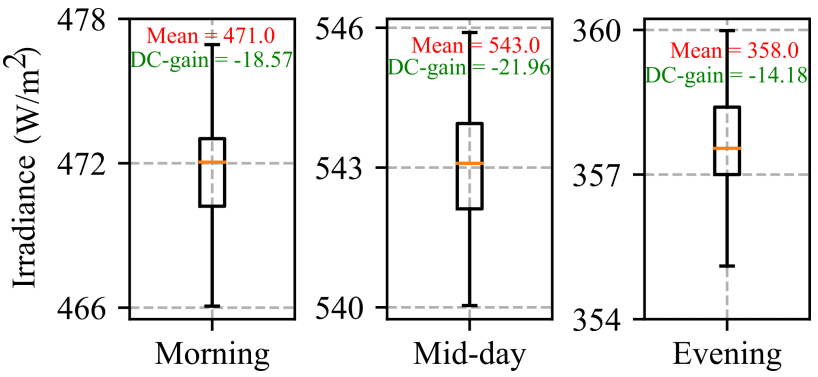

Figure 5.25. Variation of DC-gain of TF of R_2 with irradiance while activating Volt-Watt mode.

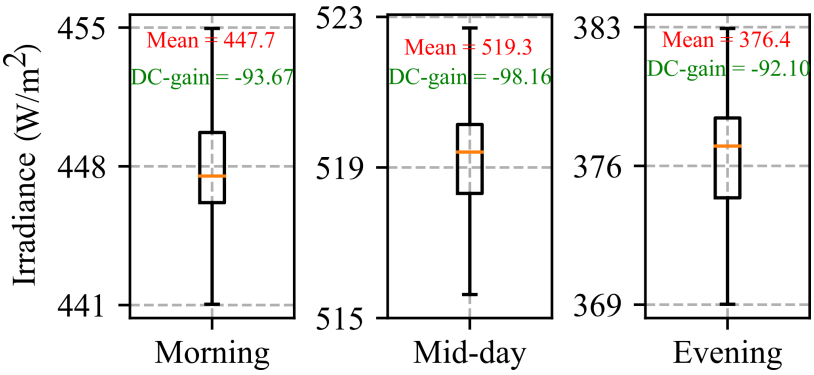

Figure 5.26. Variation of DC-gain of TF of R_2 with irradiance while activating Freq-Watt mode.

The input, output, and irradiance data at three periods of the day (these days considered are different from the previous days considered of result and analysis section) are logged on, and a box plot of irradiance is prepared as depicted in Fig. 5.25 and Fig. 5.26 respectively, and the mean value of irradiance is noted. The model is obtained by the data-driven model parameterization in new input and output datasets. The new DC-gain of each of the models is evaluated in each period of a day and is shown in Fig. 5.25 and Fig. 5.26, respectively. From the irradiance mean, it can be concluded that the DC gain increases with an increase in irradiance and decreases with a decrease in irradiance but with a negative gradient. i.e.,

$$\text{DC-gain} = -\frac{1}{B} \times \text{Irradiance}$$

Here, B is a constant value and varies with the varying modes of activation. In this case, for Volt-Watt mode, the value of B is found to be 25, and for Freq-Watt mode, the value of B is found to be 5. Based on this analysis, it is possible to conclude that each model's DC-gain depends on irradiance and has a negative gradient linear relationship with it. So,

if the TF was obtained based on the mid-day data, then

$$\text{adjusted Morning TF} = \frac{\text{Morning Irradiance}}{\text{Mid-day Irradiance}} \times \text{Mid-day TF and}$$

$$\text{adjusted Evening TF} = \frac{\text{Evening Irradiance}}{\text{Mid-day Irradiance}} \times \text{Mid-day TF}$$

Cross Validation of obtained TF

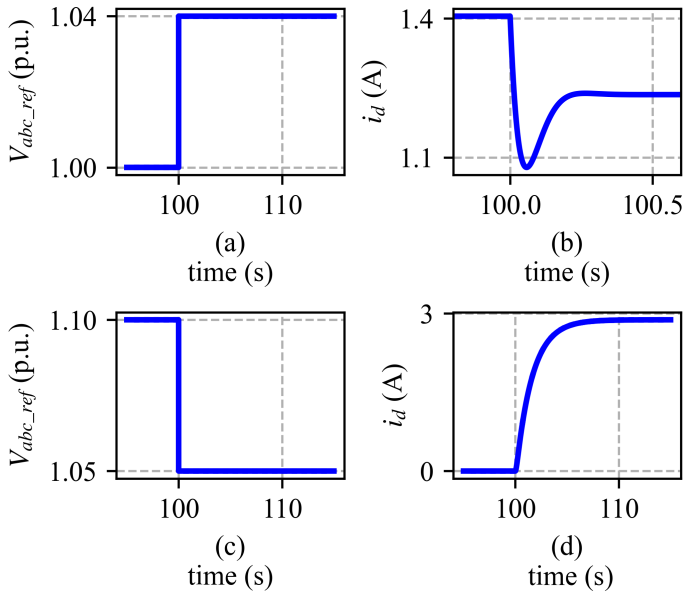

Figure 5.27. Cross-Validation of Obtained TF.

The obtained TF model is cross-validated by comparing the τ of the obtained model with the τ of the actual system. The obtained TF of Volt-Watt mode is taken into consideration for cross-validation. The obtained TF of R_1 is given step input ranging from 1 p.u. to 1.04 p.u., and the corresponding response is shown in Fig. 5.27 (a) and (b) respectively. When the voltage is changed from 1 p.u. to 1.04 p.u., the corresponding $i_d\ (A)$ response from the inverter takes $(100.4\ s - 100\ s = 0.4\ s)$ to settle to its steady state condition, as shown in Fig. 5.27 (b). This time is taken as the settling time, and by considering the 2% tolerance band, ($\tau = 0.1\ s$ of R_1 is calculated, which matches the τ of R_1 of the actual system). Similarly, when the voltage changes from 1.1 p.u. to 1.05 p.u.,

the corresponding $i_d\ (A)$ response from the inverter takes $(107\ s - 100\ s = 7\ s)$ time to get settled to its steady state condition. This time is taken as the settling time, and by considering the 2% tolerance band, the $\tau \approx 1.75\ s$ of R_2 is calculated, which matches the actual τ of R_1.

5.7 Chapter Conclusions

A data-driven modeling approach to extract GFL inverter dynamics with GSFs using designed probing signals was developed. The SysId algorithm was used to create a dynamic model of a GFL inverter, which was then validated using PHIL under the Volt-VAr GSF modes. To accurately capture the dynamics of the GFL inverter, partitioned modeling technique is used in GSFs mode from IEEE 1547-2018 standard. The GoF percentage was used to measure the performance of GFL inverter dynamics when the grid voltage was perturbed with probing signal and described which one would obtain a better model of a GFL inverter. The results show that the logarithmic Sq-chirp signal outperformed in model accuracy based on GoF compared to other probing signals to extract dynamics of GFL inverters. Logarithmic Sq-chirp signal was then used to study the effect of varying irradiance in the data-driven modeling of PV inverter dynamics. The proposed analysis is carried out in two modes of operation of inverter i.e., Volt-Watt and Freq-Watt modes following the IEEE 1547-2018 standard. The results show that magnitude of dynamics varies with varying irradiance in both modes of irradiance; however, the nature of the inverter's dynamics differs depending on the mode of activation. In addition, the dynamic model obtained has to adjust its DC-gain accordingly during different periods and DC-gain has a negative gradient linear relationship with irradiance.

CHAPTER 6 Data-Driven Modeling of Grid-Forming Inverter Dynamics Using Power Hardware-in-the-Loop Experimentation

The increasing interest in renewable energy and batteries has made PECs a critical component of power distribution networks [85]. As converter-based generation meets the future energy demand, it is crucial to have accurate models that represent the interaction between the grid and the converters. The response of converter-based generation involves faster and more stochastic dynamics compared to traditional power systems due to their fast-switching mechanisms [86]. In the past, these dynamics were largely neglected because the percentage of converter-based generation was low, and the converters had a passive role without actively contributing to voltage and frequency control in power systems. This neglect was possible because power system dynamics were primarily governed by large synchronous generators with well-defined models [50].

However, the electrical grid is undergoing a seamless transition where rotating synchronous machines are being replaced by IBRs. This transition introduces a low-inertia system with a novel type of dynamic behavior [87]. IBR control can be categorized into two types: GFL and GFM. GFL inverters, commonly used in grid-connected applications with GFL control, regulate the ac-side current by seamlessly following the phase angle of the existing grid voltage using a PLL mechanism [88], [89]. On the other hand, GFM inverters manage the ac-side voltage and play a crucial role in forming a voltage source grid, allowing them to set the grid's voltage and frequency. They achieve synchronization with the rest of the grid using frequency droop control (typically $P-\omega$ droop), similar to traditional synchronous generators [90]–[92]. Various GFM

control methods have been proposed in the literature, including droop control, virtual synchronous machine, and virtual oscillator controllers [93]–[99]. In the electrical grid, GFL inverters primarily function as current sources and can provide auxiliary services such as droop-based reactive power support [100]. They are commonly used for integrating renewable energy sources like wind and solar energy into power systems due to their straightforward control scheme, established PLL technology, and ability to operate at a specific current. However, the PLL can cause instability issues in the grid, especially when the grid impedance is high [101], [102]. With the increasing replacement of synchronous generators by IBRs, this problem is becoming more prevalent and challenging. Consequently, there is a growing focus on GFM inverters, which exhibit synchronous generator-like characteristics and can operate in weak grids without relying on rigid voltage sources or forming independent grids [90], [92], [103]. Furthermore, GFM inverters can address grid instability issues, including significant frequency fluctuations caused by low inertia and uncertainty in DERs. Hence, the shift towards converter-based generation necessitates accurate PEC models for assessing system dynamics that were previously ignored in conventional power systems. Therefore, modeling GFM inverters plays a vital role in studying system-level dynamics.

For precise modeling of PECs, a comprehensive understanding of multiple aspects of the converter is necessary. This includes knowledge of its physical topology, intricate models of voltage/current control loops, PLL models, employed protection schemes, and more. Despite the known control architecture, these factors and control parameters exhibit significant variations across different manufacturers. This variability can lead to inaccurate modeling and simulation of power systems, resulting in flawed analysis and

erroneous outcomes. The availability of accurate converter models is crucial for predicting system instability, ensuring component compatibility [104], and facilitating proper design of controllers and protection systems.

Modeling converter-based generation is further complicated by the need to comply with grid interconnection requirements and changes in grid codes. Manufacturers can address these requirements by modifying the control structure through software or firmware updates. For example, according to the IEEE 1547 standard, converters can actively contribute to voltage and frequency support through advanced control functions [67], [105]. This introduces an additional layer of complexity in modeling these converter systems. Data-driven models can be employed to address the aforementioned challenges. Recent advancements in data-driven modeling for GFL inverters have been described in the literature for system analysis purposes [104], [106]–[109]. However, there is limited research available on data-driven dynamic modeling of GFM inverters operating in droop control.

6.1 Chapter Objective

The main objective of this chapter is to develop a data-driven modeling approach that utilizes designed probing signals to extract the mathematical model representing the dynamics of a GFM inverter. The SysId algorithm is employed to obtain a dynamic model of the GFM inverter operating in the droop mode. Additionally, an analytical approach is also utilized to derive the dynamic model of the GFM inverter. The obtained dynamic models from both the analytical approach and the data-driven approach are then cross-validated to ensure their power sharing capability.

The main contributions of this paper are as follows:

1. Derived an analytical approach to obtain a mathematical model of GFM inverter dynamics;

2. Developed an experimental power-hardware-in-the-loop (PHIL) methodology to collect data by exciting load connected to GFM inverter with designed probing signals. A DDM approach is designed to extract mathematical models of GFM inverter dynamics. The mathematical model is obtained by collecting output frequency and voltage data from the GFM inverter in response to changes in the active and reactive power of the load at the point of common coupling (PCC).

The rest of the chapter is organized as follows: The theoretical background on the dynamics modeling of GFM inverter is provided in Section 6.2. The analytical approach for modeling a system with two GFM inverter are presented in Section 6.3 and the data-driven approach to access the GFM inverter dynamics in Section 4.2. In Section 6.4, the experimental setup to evaluate the performance of GFM inverter is discussed. The results are presented in Section 6.5 followed by the main conclusions in Section 6.6.

6.2 Dynamic Modeling of GFM Inverter

The dynamic modeling of a GFM inverter with their control mechanism is introduced in this section which is followed by basic concept of system identification to obtain the accurate PECs dynamics.

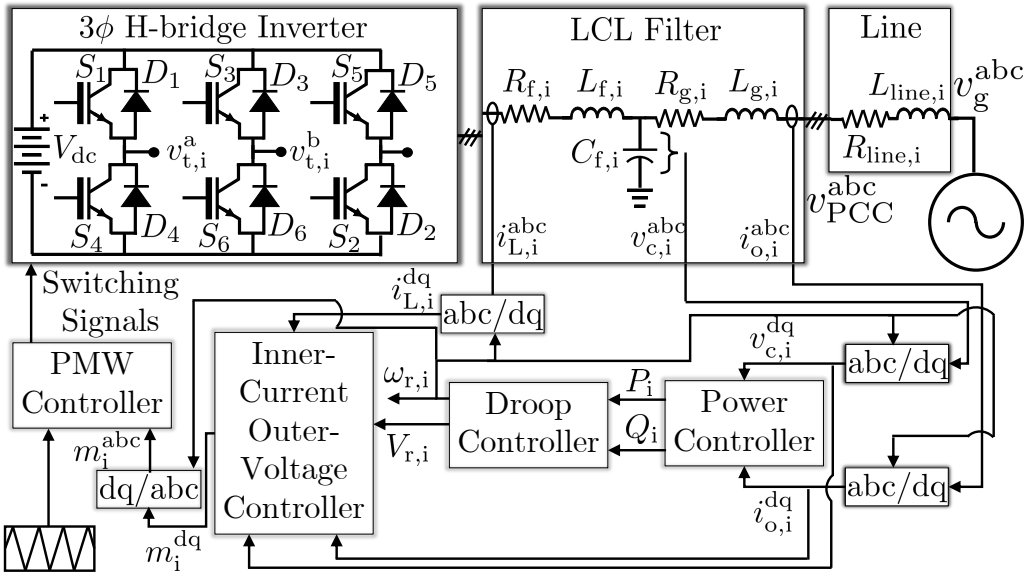

Figure 6.1. Diagram of the power circuit of i^{th} GFM inverters connected to a grid.

6.2.1 Power Circuit of GFM Inverters

The power circuit of i^{th}, 3-ϕ H-bridge GFM inverter consist of six switches distributed among three legs as shown in Fig. 6.1. It is connected to a grid at PCC with voltage, v^{abc}_{PCC}, via an LCL filter ($L_{f,i}$, $C_{f,i}$, $L_{g,i}$) and associated equivalent series resistances ($R_{f,i}$ and $R_{g,i}$ of inductors) and a coupling line with line parameters, $L_{line,i}$, $R_{line,i}$. A dq-frame multi-loop controller is employed that generates modulated voltage vector signal, m^{abc}_i, to PWM controller to generate switching signals resulting in terminal voltages, $v^a_{t,i}$, $v^b_{t,i}$ and $v^c_{t,i}$.

6.2.2 Control of GFM Inverter

The control layers of the GFM inverter are illustrated in Fig. 6.2, depicting the various control mechanisms employed. The following sections provide a description of each control aspect of the GFM inverter.

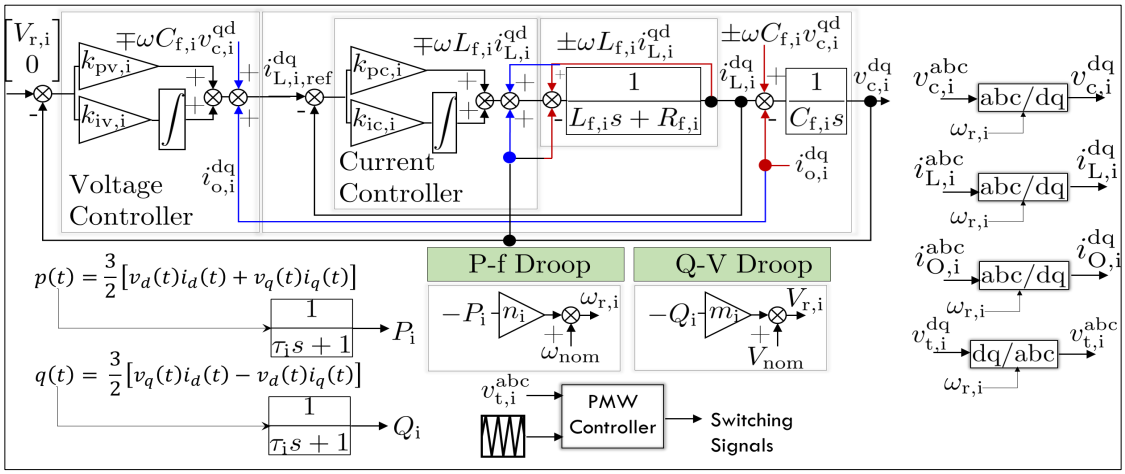

Figure 6.2. Diagram of various control loops of i^{th} GFM inverters connected to a grid.

6.2.3 Power Controller

$v_{\text{c,i}}^{\text{dq}}$, and $i_{\text{o,i}}^{\text{dq}}$ are used to determine p_{i}, and q_{i}. p_{i} and q_{i} are passed through low-pass filters with the time constant, $\tau_{\text{S,i}} \in R_{>0}$, to obtain P_{i} and Q_{i} as described by

$$P_{\text{i}} = [1/(\tau_{\text{S,i}}s+1)]p_{\text{i}},\ Q_{\text{i}} = [1/(\tau_{\text{S,i}}s+1)]q_{\text{i}}, \tag{6.1}$$

where $p_{\text{i}} := 1.5[v_{\text{c,i}}^{\text{d}} i_{\text{o,i}}^{\text{d}} + v_{\text{c,i}}^{\text{q}} i_{\text{o,i}}^{\text{q}}]$, $q_{\text{i}} := 1.5[v_{\text{c,i}}^{\text{q}} i_{\text{o,i}}^{\text{d}} - v_{\text{c,i}}^{\text{d}} i_{\text{o,i}}^{\text{q}}]$.

6.2.4 Droop Controller

A droop controller in GFM inverter is used to regulate the output frequency and voltage of the inverter to match the grid conditions. The droop controller operates by continuously monitoring the grid voltage and frequency and adjusting the inverter's output accordingly. It provides a decentralized control mechanism, allowing multiple inverters to work together and share the load in a coordinated manner. The droop controller employs a droop characteristic, which is a linear relationship between the inverter output frequency

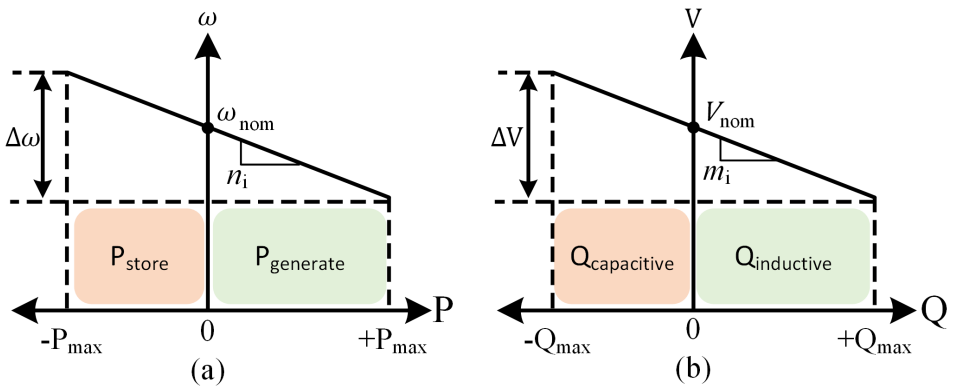

Figure 6.3. Droop control strategies. (a) *P*-ω droop (b) *Q*-*V* droop. *P*-ω droop control adjusts the active power output of a GFM inverter based on changes in frequency, maintaining a stable grid. *Q*-*V* droop control modifies the reactive power output according to variations in voltage, ensuring voltage stability in the grid.

(ω) and the active power output (P) as shown in Fig. 6.3(a), and inverter output voltage (V) and the reactive power output (Q) as shown in Fig. 6.3(b). Typically, the droop characteristic is represented as a slope which determines the rate at which the frequency/voltage changes with respect to active/reactive power variations respectively.

When the grid frequency deviates from its nominal value, the droop controller adjusts the inverter's output frequency by changing the power output. If the grid frequency decreases, the droop controller increases the inverter's power output, causing the frequency to rise back towards its nominal value. Conversely, if the grid frequency increases, the droop controller decreases the power output, bringing the frequency back to the desired level.

The droop controller also regulates the output voltage of the inverter. It monitors the grid voltage and adjusts the inverter's voltage magnitude to maintain synchronization with the grid. By maintaining a stable output voltage and frequency, the droop controller ensures that the GFM inverter operates in harmony with the grid and provides reliable

power supply.

Basically, droop control is a proportional controller with active and reactive power as control variables where the control gains (also the droop gains) dictate the steady–state power sharing of the inverters. The active power, frequency, P-f, droop control is considered here as a proportional controller (with proportional coefficient as n_{i}) with error signal $e_{\mathrm{P,i}} := -P_{\mathrm{i}}$ where P_{i} is the control variable. Whereas, the reactive power, voltage magnitude, Q-V, droop control is considered here as a proportional controller (with proportional coefficients as m_{i}) with error signal $e_{\mathrm{Q,i}} := -Q_{\mathrm{i}}$ where Q_{i} is the control variable. The values of n_{i} and m_{i} are typically chosen such that $\omega_{\mathrm{r,i}}$ and $V_{\mathrm{r,i}}$ are within the allowed specification, defined by IEEE 1547 Standard [67].

6.2.5 Inner-current-outer-voltage Controller

The conventional inner-current-outer-voltage controller architecture is employed for the inverters [110]. For the inner-current controller, $i^{\mathrm{dq}}_{\mathrm{L,i,ref}}$ is provided as the reference signal to be tracked by the output signal, $i^{\mathrm{dq}}_{\mathrm{L,i}}$. A proportional-integral (PI) compensator is used for tracking the reference of the dq-axis inductor current. For a desired time constant, $\tau_{\mathrm{c,i}}$, the parameters of the current controller are selected as $k_{\mathrm{pc,i}} = L_{\mathrm{f,i}}/\tau_{\mathrm{c,i}}$ and $k_{\mathrm{ic,i}} = R_{\mathrm{f,i}}/\tau_{\mathrm{c,i}}$. Depending on the switching frequency, $\tau_{\mathrm{c,i}}$ is typically selected to be in the range of 0.5-2 ms [110]. Additional feed-forward signals, $v^{\mathrm{dq}}_{\mathrm{c,i}}$ and $\mp\omega L_{\mathrm{f,i}} i^{\mathrm{qd}}_{\mathrm{L,i}}$ facilitate the disturbance rejection capability. For outer-voltage controller, $\begin{bmatrix} V_{\mathrm{r,i}} & 0 \end{bmatrix}^{\top}$ is the reference signal to be tracked by the voltage signal, $v^{\mathrm{dq}}_{\mathrm{c,i}}$. A PI compensator is used to enable reference tracking. For a desired phase margin and gain cross-over frequency, the parameters of the voltage controller ($k_{\mathrm{pv,i}}$ and $k_{\mathrm{iv,i}}$) can be designed based on *symmetrical*

optimum method [110]. Similarly, additional feed-forward signals, $v_{c,i}^{dq}$ and $\mp\omega C_{f,i} v_{c,i}^{qd}$ facilitate the disturbance rejection capability for the outer voltage control loop.

6.3 Analytical Modeling of a System with Two GFM Inverter

The system, as shown in Fig. 6.4 is considered in this section for modeling and analyzing. For analysis purpose, the following remarks are made:

Remark 1 *The inner-current-outer-voltage control loop for GFM inverter is stable and has faster (*$>$ 10 *times) dynamics when compared to the power and droop controller and tracks its voltage reference with minimal (assumed zero) tracking error as suggested in [110].*

Remark 2 *All* abc-dq *conversions are adopted w.r.t. GFM 1.*

Using Remark 1 and Remark 2, following non-linear state-space equations can be obtained for the entire system of Fig. 6.4:

$$\dot{\theta}_2 = \omega_{r,2} - \omega_{r,1}, \text{ where } \theta_2 := \theta_{r,2} - \theta_{r,1}, \tag{6.2}$$

$$\tau_{S,1}\dot{\omega}_{r,1} = \omega_{nom} - \omega_{r,1} - n_i[p_1], \tag{6.3}$$

$$\tau_{S,2}\dot{\omega}_{r,2} = \omega_{nom} - \omega_{r,2} - n_2[p_2], \tag{6.4}$$

$$\tau_{S,1}\dot{V}_{r,1} = V_{nom} - V_{r,1} - m_1[q_1], \tag{6.5}$$

$$\tau_{S,2}\dot{V}_{r,2} = V_{nom} - V_{r,2} - m_2[q_2], \tag{6.6}$$

$$L_{l,1}\dot{i}^d_{o,1} = V_{r,1} - R_{l,1}i^d_{o,1} - v^d_{PCC} + \omega_{r,1}L_{l,1}i^q_{o,1}, \tag{6.7}$$

$$L_{l,1}\dot{i}^q_{o,1} = -R_{l,1}i^q_{o,1} - v^q_{PCC} - \omega_{r,1}L_{l,1}i^d_{o,1}, \tag{6.8}$$

$$i^d_L = i^d_{o,1} + i^d_{o,2}, i^q_L = i^q_{o,1} + i^q_{o,2} \tag{6.9}$$

$$\begin{aligned} v^d_{PCC} = 0.5\times[&(V_{r,1} + V_{r,2}\cos\theta_2) - (R_{l,1}i^d_{o,1} + R_{l,2}i^d_{o,2}) \\ &+ (\omega_{r,1}L_{l,1}i^q_{o,1} + \omega_{r,2}L_{l,2}i^q_{o,2})] \end{aligned} \tag{6.10}$$

$$\begin{aligned} v^q_{PCC} = 0.5\times[&(V_{r,2}\sin\theta_2) - (R_{l,1}i^q_{o,1} + R_{l,2}i^q_{o,2}) \\ &- (\omega_{r,1}L_{l,1}i^d_{o,1} + \omega_{r,2}L_{l,2}i^d_{o,2})] \end{aligned} \tag{6.11}$$

where, $\theta_{\mathrm{r,i}}$ is the GFM inverter internal phase angle, $p_{\mathrm{i}} := 1.5[V_{\mathrm{r,i}}i^{\mathrm{d}}_{\mathrm{o,i}}\cos\theta_{\mathrm{i}} + V_{\mathrm{r,i}}i^{\mathrm{q}}_{\mathrm{o,i}}\sin\theta_{\mathrm{i}}]$, and $q_{\mathrm{i}} := 1.5[-V_{\mathrm{r,i}}i^{\mathrm{q}}_{\mathrm{o,i}}\cos\theta_{\mathrm{i}} + V_{\mathrm{r,i}}i^{\mathrm{d}}_{\mathrm{o,i}}\sin\theta_{\mathrm{i}}]$. ω_{nom} and V_{nom} are nominal frequency and voltage respectively. This results in a 7^{th}-order non-linear electromagnetic model. It allows to model a GFM inverter as a voltage source with controllable phase, $\theta_{\mathrm{r,i}}$, frequency, $\omega_{\mathrm{r,i}}$, and amplitude, $V_{\mathrm{r,i}}$ [111], as shown in Fig. 6.5.

While two GFM inverters are connected to in parallel supplying a load, the system can be modeled by a non-linear system, $\dot{\underline{x}}_{\mathrm{GFM}} = \underline{G}_{\mathrm{GFM}}(\underline{x}_{\mathrm{GFM}})$, where, $\underline{G}_{\mathrm{GFM}}(.)$ consists of

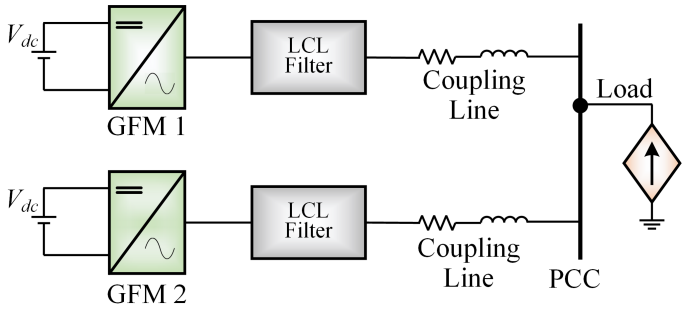

Figure 6.4. For the purpose of modeling and analysis, a system consisting of two GFM inverters is being considered. The inverter's output is directed through an LCL filter, and a load is connected to the PCC via a coupling line.

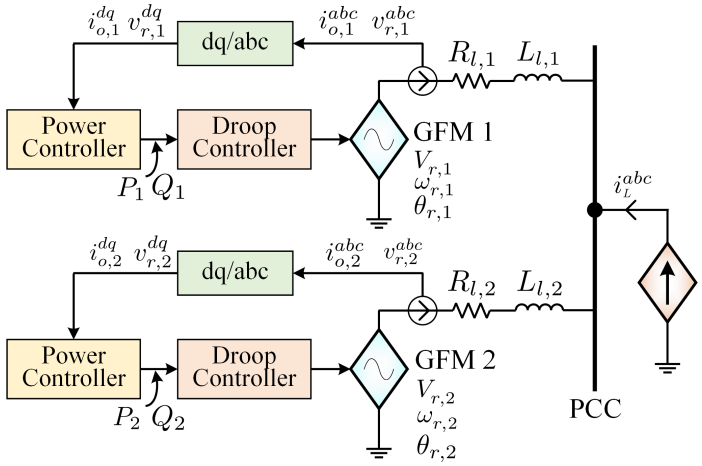

Figure 6.5. The GFM inverter is represented in the model as a voltage source that can control its phase, $\theta_{r,i}$, frequency, $\omega_{r,i}$, and amplitude. Additionally, a controlled load is connected to the PCC.

(2)-(11). Considering the system linearized around an equilibrium point, $\underline{x}_{\text{GFM}}^{\text{eq}}$, such that

$$\Delta\dot{\underline{x}}_{\text{GFM}} = A_{\text{GFM}}\Delta\underline{x}_{\text{GFM}} + B_{\text{GFM}}\Delta\underline{u}_{\text{GFM}} \tag{6.12}$$

$$\Delta\dot{\underline{y}}_{\text{GFM}} = C_{\text{GFM}}\Delta\underline{x}_{\text{GFM}} \tag{6.13}$$

where

$$A_{\text{GFM}} = \underline{F}_{\text{GFM}}(\underline{x}^{\text{eq}}_{\text{GFM}}) \tag{6.14}$$

$$B_{\text{GFM}} = \begin{bmatrix} R_{l,1} & \omega_{r,1}L_{l,1} \\ -\omega_{r,1}L_{l,1} & R_{l,1} \end{bmatrix} \tag{6.15}$$

$$C_{\text{GFM}} = \begin{bmatrix} 0 & 1 & 0 & 0 & 0 & 0 & 0 \\ 0 & 0 & 0 & 1 & 0 & 0 & 0 \end{bmatrix} \tag{6.16}$$

where, $\underline{F}_{\text{GFM}}(.)$ is the vector field of $G_{\text{GFM}}(\underline{x}_{\text{GFM}})$. Here,

$$\Delta\underline{x}_{\text{GFM}} = [\Delta\theta_2\ \Delta\omega_{r,1}\ \Delta\omega_{r,2}\ \Delta V_{r,1}\ \Delta V_{r,2}\ \Delta i^d_{o,1}\ \Delta i^q_{o,1}]^\top \tag{6.17}$$

$$\Delta\underline{y}_{\text{GFM}} = [\Delta\omega_{r,1}\ \Delta V_{r,1}]^\top \tag{6.18}$$

$$\Delta\underline{u}_{\text{GFM}} = [\Delta i^d_L\ \Delta i^q_L]^\top \tag{6.19}$$

Therefore, the multiple input multiple output linearized system can be written as:

$$\begin{bmatrix} \Delta\omega_{r,1} \\ \Delta V_{r,1} \end{bmatrix} = \underbrace{\begin{bmatrix} T_1 & T_2 \\ T_3 & T_4 \end{bmatrix}}_{T} \begin{bmatrix} \Delta i^d_L \\ \Delta i^q_L \end{bmatrix} \tag{6.20}$$

where, $T = C_{\text{GFM}}[sI - A_{\text{GFM}}]^{-1}B_{\text{GFM}}$.

6.3.1 Partitioned Modeling of Droop Controller

Due to the presence of nonlinearities in GFM inverters, modeling of GFM inverter with droop controller over the operating regions results in intricate dynamic models, and

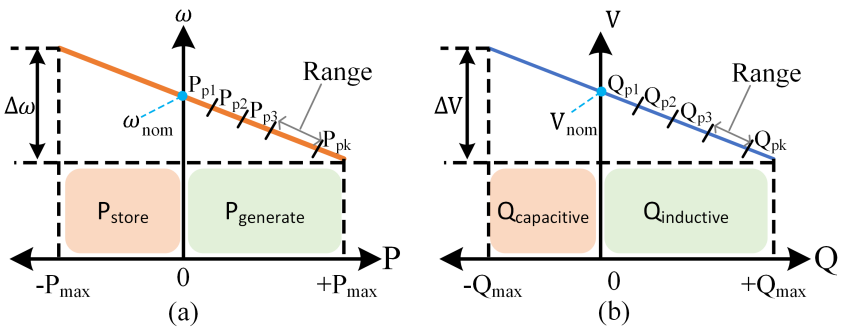

Figure 6.6. Demonstration of linear partitioning of the GFM inverter. The *P*-ω and *Q*-*V* droop curve are divided into several ranges.

the complex dynamics of the whole operating region are effectively captured by dividing the operating regions further into small linear ranges [83] as shown in Fig. 6.6(a) and Fig. 6.6(b), where $P_{p1}, P_{p2}, ..., P_{pk}$ represent ranges corresponding to load active power changes, and $Q_{q1}, Q_{q2}, ..., Q_{qk}$ represent ranges associated with load reactive power changes.

With the selected operating limits, the desired active power signal is generated according to Algorithm 1 to extract reduced-order linear dynamic models of the GFM inverter for frequency variations. Additionally, the reactive power signal is generated based on Algorithm 2 to obtain reduced-order linear dynamic models of the GFM inverter for voltage variations.

6.3.2 Flowchart to Assess GFM Inverter Dynamics

The flowchart to identify the TF of a GFM inverter from the SysId algorithm is shown in Fig. 4.4. Logarithm square-chirp probing signal is used to perturb the load as it outperformed other probing signals in model accuracy based on GoF to extract dynamics of PECs [109]. Fig. 6.7 shows the load active power variation which is varied from 0 to 20 kW for 15 seconds, after which it is increased by 10 kW in subsequent ranges until

Algorithm 1: Active Power Variation to Generate Probing Signal for Frequency Variation

Input: Operational limits $\leftarrow [P_{low}, P_{max}]$
Simulation clock time $\leftarrow t$
Initialization :
Time interval for each partition $\leftarrow T$
Lower active power starting value $P_{k1} \leftarrow P_{low}$
Higher active power for same partition P_{k2}
Difference between active power $dp \leftarrow P_{k2} - P_{k1}$
while *True* **do**
  $k \leftarrow \text{floor}(t/T)$
  $p_1 \leftarrow P_{k1} + k \times dp/2$
  $p_2 \leftarrow p_1 + dp$
  if $p_2 > P_{max}$ **then**
    $p_1 \leftarrow P_{max} - dp$
    $p_2 \leftarrow P_{max}$
  end
end

Algorithm 2: Reactive Power Variation to Generate Probing Signal for Voltage Variation

Input: Operational limits $\leftarrow [Q_{low}, Q_{max}]$
Simulation clock time $\leftarrow t$
Initialization :
Time interval for each partition $\leftarrow T$
Lower reactive power starting value $Q_{k1} \leftarrow Q_{low}$
Higher reactive power for same partition Q_{k2}
Difference between reactive power $dq \leftarrow Q_{k2} - Q_{k1}$
while *True* **do**
  $k \leftarrow \text{floor}(t/T)$
  $q_1 \leftarrow Q_{k1} + k \times dq/2$
  $q_2 \leftarrow q_1 + dq$
  if $q_2 > Q_{max}$ **then**
    $q_1 \leftarrow Q_{max} - dq$
    $q_2 \leftarrow Q_{max}$
  end
end

reaching a total of 200 kW. This power variation follows the droop curve characteristics of the GFM inverter. The frequency of the Square-chirp signal ranges from 1 Hz to 32 Hz, with values selected based on the settling time response parameters of the GFM inverter.

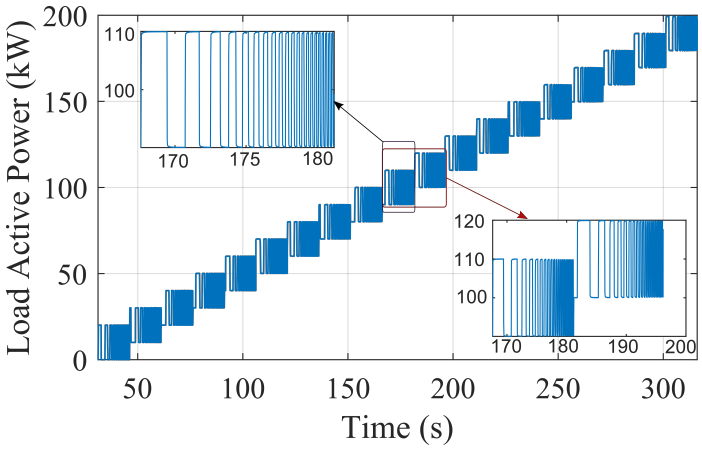

Figure 6.7. Sq-chirp probing signal, generated using Algorithm 1, was employed to excite load active power ranging from 0 to 200 kW.

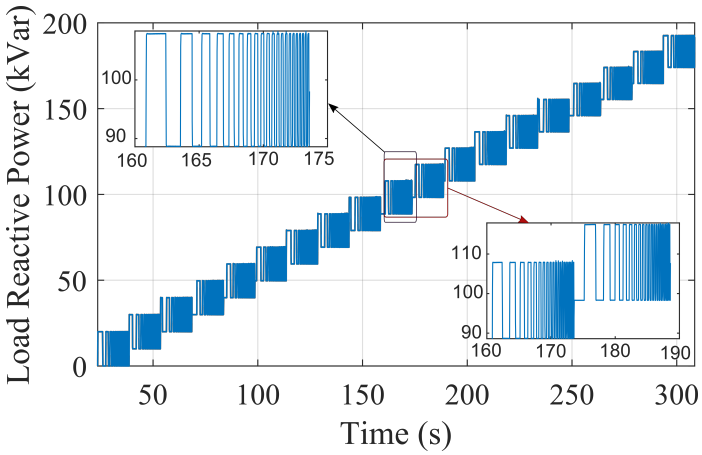

Figure 6.8. Sq-chirp probing signal, generated using Algorithm 2, was employed to excite load reactive power ranging from 0 to 200 kVAr.

Similarly, Fig. 6.8 illustrates the load reactive power variation which is varied from 0 to 20 kVAr for 15 seconds, and then increased by 10 kVAr in subsequent ranges until reaching a total of 200 kVAr. This reactive power adjustment aligns with the droop curve characteristics of the GFM inverter.

In order to determine the TF of physical dynapower GFM inverter (represented as GFM 1 on-wards), the measured inputs, including the active and reactive power supplied by the GFM 1, along with the output frequency and voltage at the terminal of the GFM 1, are logged using the Opal-RT. The collected data is divided into small ranges for analysis.

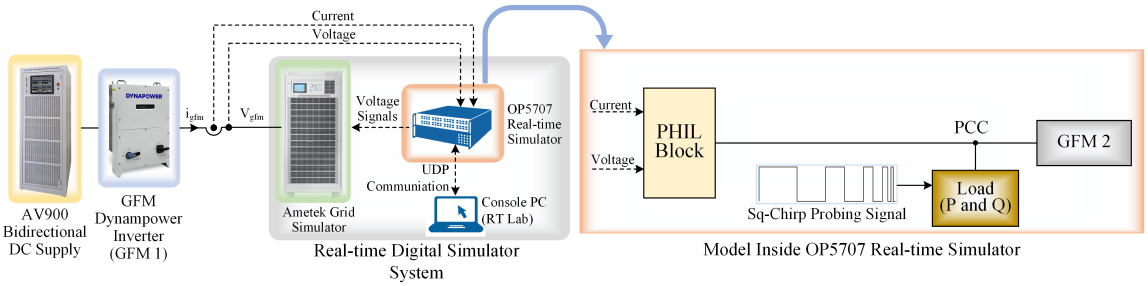

Figure 6.9. Experimental setup to assess the TF of GFM Dynapower inverter (GFM 1) as analyzed in Fig. 6.4. Load P and Q are excited by the Sq-chirp probing signal.

Then, the data is filtered using the mean filter to smooth logged data. Furthermore, the mean of both active power and reactive power, and frequency and voltage of GFM 1 measurements are eliminated to obtain more accurate TF model. This allows SysId to focus on the real variations caused by the probing signals. The dataset is divided into two parts for cross-validation: a training set for computing TF model, and a validation set for validating the resulting TF model. The number of poles and zeroes of TF model for data-driven approach are chosen based on the TF finding from analytical approach.

6.4 Experimental Setup

The hardware experimental setup is developed as shown in Fig. 6.9 to assess the TF of a commercially available three-phase 125 kVA Dynapower GFM inverter (GFM 1). A PHIL setup is employed which comprises an OP5707 RTS, an Ametek grid simulator, and GFM 1. The grid simulator utilized in this experiment was a controlled AC source amplifier with a capacity of 270 kVA. The RTS, grid simulator, and console PC were used collectively to which GFM 1 was connected. Additionally, the AV900 bidirectional DC supply, which was available in the power system integration lab at the National Renewable Energy Laboratory, was connected to the DC terminal of GFM 1. The console PC and

OP5707 RTS communicated with each other using the User Datagram Protocol (UDP).

Table 6.1. GFM Inverter, LCL Filter, and Load Parameters [1]

Parameter	Value
Rated power capacity of GFM inverter	125 kVA
Frequency droop gain for GFM inverter	0.5 Hz/125 kW
Voltage droop gain for GFM inverter	24 V/125 kVAr
Nominal frequency	60 Hz
Line-line voltage	480 V
L_f	150e-6 H
R_f	50e-3 Ω
C_f	110e-6 F
L_g	15e-6 H
R_g	50e-3 Ω
Load active power change	0 - 200 kW
Load reactive power change	0 - 200 kVAr

[1] The parameters of the GFM inverters (i.e. GFM 1 and GFM 2) are same.

Fig. 6.9 is used to assess the TF of GFM 1 which includes an Opal-RT with a virtual GFM (GFM 2) and virtual load. GFM 1 is linked to the model through PHIL. The active and reactive power of the load were perturbed using a square-chirp probing signal as shown in Fig. 6.7 and Fig. 6.8 respectively, and is used in Fig. 6.9 to excite the GFM inverters which consequently affect the frequency and voltage produced by the GFM inverters. This probing signal was generated using the algorithms described in Algorithm 1 and Algorithm 2. The settings for the Ametek grid simulator, GFM 1, GFM 2, inverter filter parameter, and load are shown in Table 6.1.

6.5 Results and Analysis

The TF of GFM 1 inverter which operates in droop mode is obtained from the SysId algorithm and the response (frequency/voltage) of GFM 1 inverter with the change in load active/reactive power are analyzed in this section.

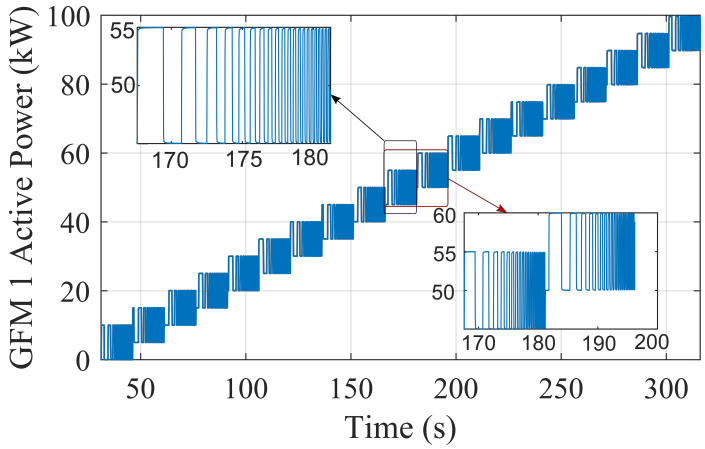

Figure 6.10. Active power supplied by GFM 1 due to perturbation of load active power.

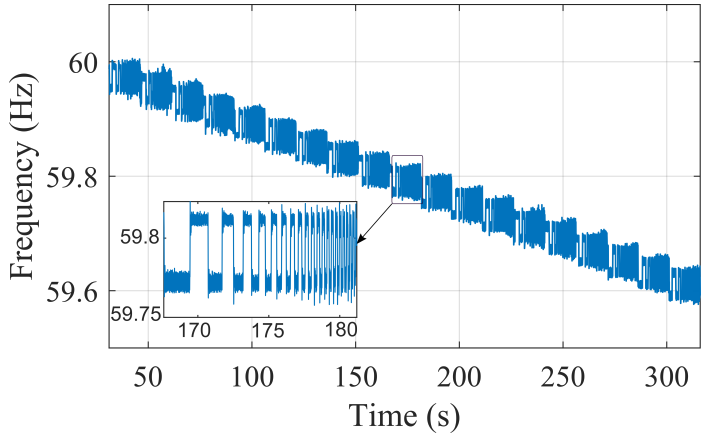

Figure 6.11. Frequency response of GFM 1 due to perturbation of load active power.

Active power supplied by the GFM 1 inverter due to change in active power of load is depicted in Fig. 6.10, while GFM 1 frequency response is illustrated in Fig. 6.11. It can be observed that as the active power of the load increases, active power supplied by the GFM 1 inverter also increases but the frequency decreases, aligning with the droop curve characteristic of the GFM inverter. Similarly, Fig. 6.12 represents the reactive power supplied by the GFM 1 inverter due to the variation in the reactive power of the load, and Fig. 6.13 showcases the response of GFM 1 voltage. It is evident that as the reactive power of the load increases, GFM 1 inverter supplied more reactive power which results in drop in the GFM 1 terminal voltage, aligning with the droop curve behavior of

the GFM inverter.

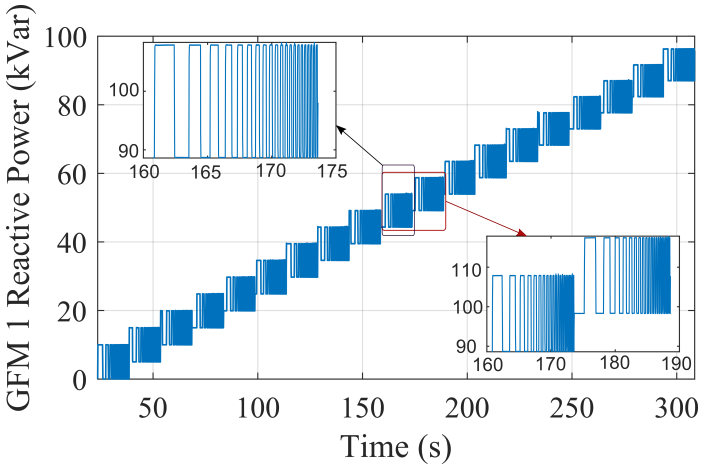

Figure 6.12. Reactive power supplied by GFM 1 due to perturbation of load reactive power.

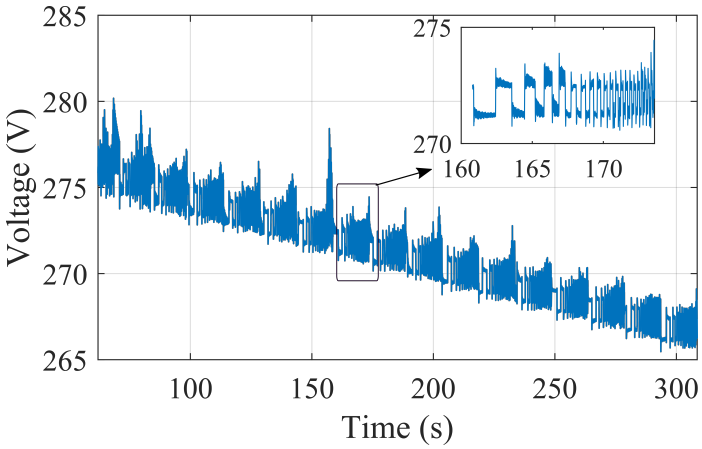

Figure 6.13. Voltage response of GFM 1 due to perturbation of load reactive power.

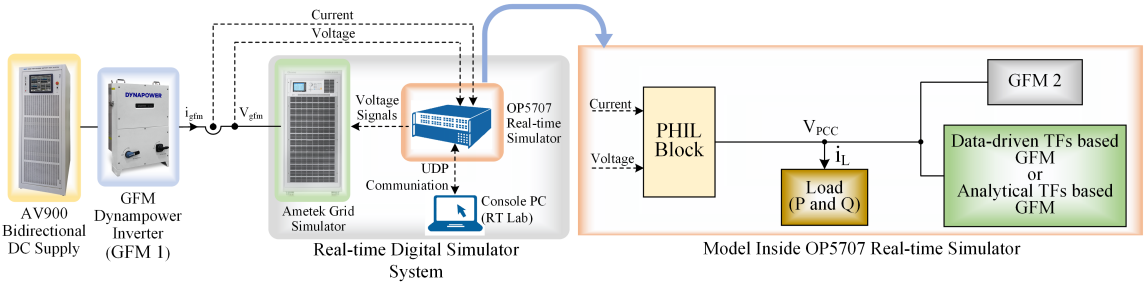

Figure 6.14. Experimental setup to validate the TFs obtained from analytical and data-driven approach of GFM 1.

Table 6.2 shows the TFs corresponding to the GFM 1 inverter. These TFs were derived from analytical and data-driven modeling approach. The TF of the GFM 1

Table 6.2. Transfer functions of GFM 1 inverter obtained from both analytical and data-driven approach.

Transfer Functions From Analytical Approach	
$T_{1\_Analytical} = \mathrm{TF}(\frac{\omega}{i_{Ld}})$	$\frac{-0.00352s^5-12.21s^4-1189s^3-3.887e04s^2-4.247e05s-4.977e04}{s^7+6789s^6+1.207e07s^5+1.494e09s^4+7.191e10s^3+1.986e12s^2+3.887e13s+3.986e14}$
$T_{2\_Analytical} = \mathrm{TF}(\frac{\omega}{i_{Lq}})$	$\frac{0.0003977s^5+0.03122s^4-809.7s^3-4.942e04s^2-7.558e05s-8.884e04}{s^7+6789s^6+1.207e07s^5+1.494e09s^4+7.191e10s^3+1.986e12s^2+3.887e13s+3.986e14}$
$T_{3\_Analytical} = \mathrm{TF}(\frac{v}{i_{Ld}})$	$\frac{0.01909s^5+1.742s^4+54.92s^3-2.927e05s^2-1.783e07s-2.711e08}{s^7+6789s^6+1.207e07s^5+1.494e09s^4+7.191e10s^3+1.986e12s^2+3.887e13s+3.986e14}$
$T_{4\_Analytical} = \mathrm{TF}(\frac{v}{i_{Lq}})$	$\frac{0.1689s^5+585.8s^4+5.253e04s^3+1.622e06s^2+1.854e07s+4.477e07}{s^7+6789s^6+1.207e07s^5+1.494e09s^4+7.191e10s^3+1.986e12s^2+3.887e13s+3.986e14}$
Transfer Functions From Data-driven Approach	
$T_{1\_DDM} = \mathrm{TF}(\frac{\omega}{i_{Ld}})$	$\frac{-104.5s^5-2869s^4-1.257e05s^3-1.773e05s^2-2.56e04s-4562}{s^7+138.7s^6+1.947e04s^5+6.389e05s^4+1.721e07s^3+2.392e07s^2+3.336e06s+6.194e05}$
$T_{2\_DDM} = \mathrm{TF}(\frac{\omega}{i_{Lq}})$	$\frac{2.539e07s^5-2.101e09s^4-2.356e10s^3-4.357e12s^2-1.233e13s-3.314e12}{s^7+421.3s^6+9.008e04s^5+8.876e06s^4+3.553e08s^3+1.165e10s^2+3.219e10s+7.277e09}$
$T_{3\_DDM} = \mathrm{TF}(\frac{v}{i_{Ld}})$	$\frac{5.506e08s^5+2.015e10s^4+2.068e11s^3+5.602e11s^2-2.938e10s+9.118e10}{s^7+1825s^6+1.866e05s^5+1.076e07s^4+9.824e07s^3+3.272e08s^2+7.241e07s+3.568e07}$
$T_{4\_DDM} = \mathrm{TF}(\frac{v}{i_{Lq}})$	$\frac{1175s^5+1.309e05s^4+4.178e06s^3+3.367e07s^2+2.84e07s+2.934e06}{s^7+281.7s^6+5.059e04s^5+3.255e06s^4+1.174e08s^3+8.502e08s^2+8.494e08s+1.935e07}$

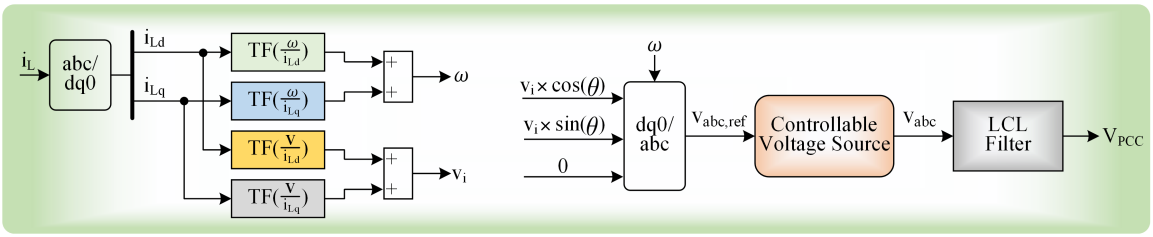

Figure 6.15. Implementation of TF obtained in the EMT simulation using Opal-RT.

inverter, as obtained, is subsequently incorporated into an EMT simulation using Opal-RT, illustrated in Fig. 6.14. This simulation is employed to verify the power distribution among the TF-based GFM, GFM 1, and GFM 2 under different load scenarios. In Fig. 6.15, TF-based model is implemented in the EMT simulation using opal-RT. Here, the load current is passed to the $abc-dq0$ block, where the direct and quadrature axis currents (i_{Ld}, i_{Lq}) are calculated. This currents is fed to TF-based model and the output of the TF-based model provides estimates for voltage and frequency (v_i, ω). Subsequently, v_i

is conveyed to the $dq0 - abc$ block to generate the reference voltage. This reference voltage is then supplied to a controllable voltage source, and its output passes through an LCL filter to produce the PCC voltage (V_{PCC}).

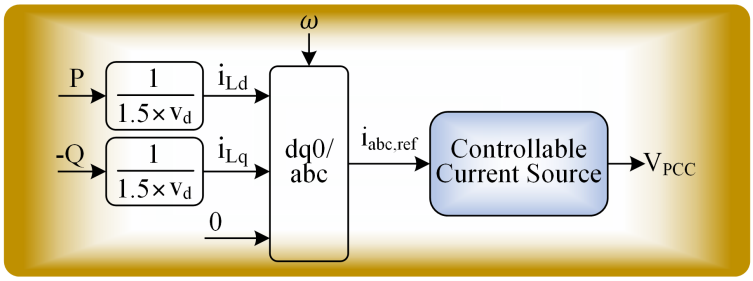

Figure 6.16. Implementation of load in the EMT simulation using Opal-RT.

Similarly, in Fig. 6.16, the load current (i_{Ld}, i_{Lq}) is calculated from active and reactive power (P and Q) of load, which is then passed to $abc - dq0$ block to generate the reference current (i_{abc_ref}). i_{abc_ref} is then passed to a controllable current source to generate the PCC voltage (V_{PCC}).

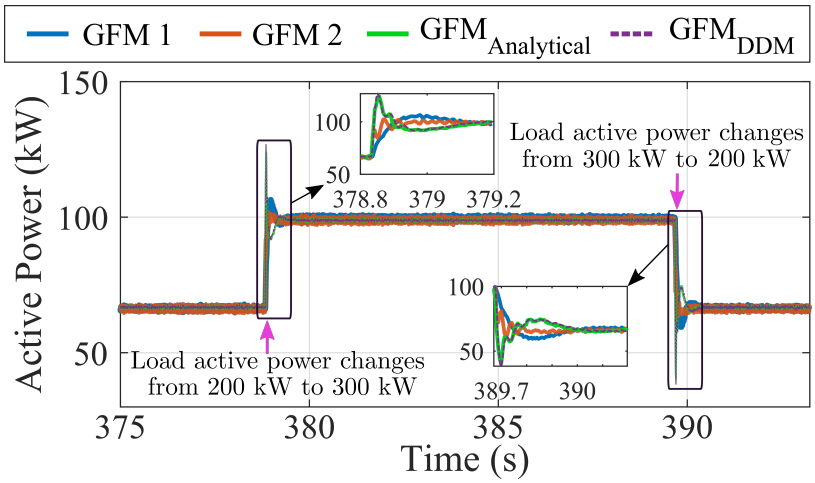

Figure 6.17. Active power shared by GFM 1, GFM 2, and TFs-based GFM obtained from the analytical and DDM approach.

To validate the TFs-based GFM, initially, the TF obtained through the analytical approach is implemented in Fig. 6.14 and then TF obtained from DDM approach is

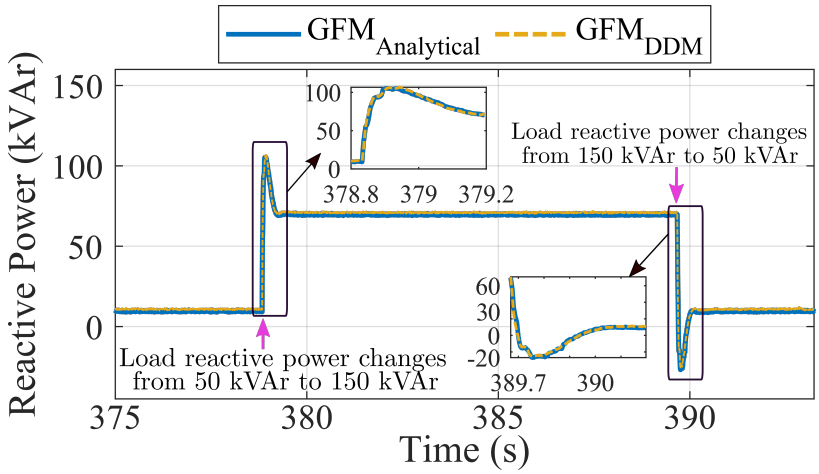

Figure 6.18. Reactive power response comparison for TFs-based GFM obtained from analytical and DDM approach.

implemented. The comparison of active power shared by GFM 1, GFM 2, and TFs-based GFM obtained from analytical and DDM approaches is depicted in Fig. 6.17. Here, the active power of the load is changed from 200 kW to 300 kW at 378.8 sec and then reverted back to 200 kW from 300 kW at 389.7 sec. The results indicate equal power sharing across all three GFMs. Initially, 66.67 kW of active power is shared, followed by 100 kW, and then again 66.67 kW of power distribution, corresponding to the load changes. Fig. 6.17 also demonstrates that the active power shared by the TFs-based GFM obtained from DDM exhibits similar dynamics compared to the analytical TFs-based GFM approach. However, the dynamics is slightly different compared to GFM 1 dynamics. This difference might be due to the challenge of capturing some of the non-linearities of the GFM 1 inverter dynamics that are not being fully captured in this large signal event, which is a limitation for the current implementation of this method that should be addressed as future work. However, both models converged in steady state with the GFM 1 and GFM 2 implementations. To compare the performance of TFs-based GFM

obtained from the analytical and DDM approaches, GoF based on NRMSE as given in Eq. 3.1 is calculated. For this, active power supplied from both the TF-based GFM models is compared with the GFM 1 active power. The GoF for the analytical approach and data-driven approach is calculated to be 89.09% and 87.97% respectively. This demonstrates that both approaches can accurately capture the dynamic response of GFM inverters under different loading conditions.

Similarly, in Fig. 6.18, we compare the reactive power responses of the TFs-based GFM obtained from the analytical and DDM approaches. The reactive power of the load is changed from 50 kVAr to 150 kVAr at 378.8 sec and then reverted back to 50 kVAr from 150 kVAr at 389.7 sec. The DDM TFs-based GFM approach exhibits similar dynamics compared to analytical TFs-based GFM approach.

6.6 Chapter Conclusions

This paper presents an analytical approach and DDM approach to obtain mathematical model of GFM inverter dynamics. A DDM modeling approach uses PHIL experiments to capture dynamic GFM data in the application of DDM techniques. A square-chirp probing signal was employed to perturb the active and reactive power of the load inside the Opal-RT model. The dynamic response of the GFM inverter, including changes in frequency and voltage, was recorded. This data was then used in system identification algorithm to identify the dynamic models of the GFM inverter. Furthermore, the mathematical model of GFM inverter dynamics obtained from analytical approach and DDM approach are then compared based on GoF. GoF for the analytical approach and DDM approach was calculated to be 89.09% and 87.97% respectively. Hence, both

approach demonstrated accuracy in capturing the dynamic response of GFM inverters under varying loading conditions.

CHAPTER 7 Conclusions and Future Work

7.1 Conclusions

A significant amount of converter-based generation is being integrated into the bulk electric power grid to fulfill the future electric demand through renewable energy sources, such as wind and PV. The dynamics of converter systems in the overall stability of the power system can no longer be neglected as in the past. Numerous efforts have been made in the literature to derive detailed dynamic models, but using detailed models becomes complicated and computationally prohibitive in large system level studies. Moreover, with the increasing replacement of synchronous generators by IBRs, instability issues in the grid is becoming more prevalent and challenging. Consequently, there is a growing focus on GFM inverters, which exhibit synchronous generator-like characteristics and can operate in weak grids without relying on rigid voltage sources or forming independent grids. Furthermore, GFM inverters can address grid instability issues, including significant frequency fluctuations caused by low inertia and uncertainty in DERs. Therefore, modeling PECs plays a vital role in studying system-level dynamics.

In Chapter 2, a concise overview of the current state-of-the-art modeling technique employed in CDPS is presented. A review of PEC model types used to analyze CDPS dynamic stability issues is also presented. A comprehensive overview of various PEC model types employed for addressing dynamic stability concerns in CDPS are presented. Challenges and benefits of using the appropriate PEC model type for studying each type of stability issue are also presented.

In Chapter 3, a MATLAB/Simulink model of a PEC featuring GSFs according to

the IEEE 1547-2018 Standard is presented. This model proves valuable for assessing power system dynamics in scenarios with high DERs penetration. The validation process confirms the accuracy of the GSFs integrated into the inverter simulation model, with NRMSE values below 2%, demonstrating close alignment with the IEEE standard characteristic curve. Through dynamic simulations, the model's effectiveness in various operating conditions was evident. The results show the improvement on grids' frequency and voltage profile using frequency-watt mode, and, volt-var and volt-watt modes respectively.

Chapter 4 focuses on developing a data-driven modeling framework for extracting PECs dynamics using a designed probing signals. It emphasizes on design parameters for the system identification algorithm to obtain precise TFs. The methodology details systematic data collection and dataset organization. By learning from actual operational data, data-driven models accurately represent the complexities of power electronics systems, contributing to accurate finding of TFs. Lastly, it guides the implementation of the TFs model into EMT simulations, ensuring practical applicability.

In Chapter 5, to accurately capture the dynamics of the GFL inverter, predefined regions in piecewise characteristics curve based on the set-point from IEEE 1547-2018 for Volt-VAr, Volt-Watt, and Freq-Watt modes were used, with each region further partitioned into small ranges. The GoF percentage was used to measure the performance of GFL inverter dynamics when the grid voltage/frequency was perturbed with probing signal and described which one would obtain a better model of a GFL inverter. The results show that the logarithmic Sq-chirp signal outperformed in model accuracy based on GoF compared to other probing signals to extract dynamics of GFL inverters. Logarithmic Sq-chirp

signal was then used to study the effect of varying irradiance in the data-driven modeling of PV inverter dynamics. The proposed analysis is carried out in two modes of operation of the inverter, i.e., Volt-Watt and Freq-Watt modes. The results show that magnitude of dynamics varies with varying irradiance in both modes of activation; however, the nature of the inverter's dynamics differs depending on the mode of activation. In addition, in order to make one model a generic dynamic model, it has to adjust its DC-gain accordingly during different periods, and DC-gain has a negative gradient linear relationship with irradiance.

Finally, in Chapter 6, a data-driven modeling of GFM inverter dynamics using PHIL techniques was developed. The proposed approach involved the real-time coupling of hardware and software components, where the physical inverter hardware was interfaced with a MATLAB simulation environment. Through this integration, data on the inverter's dynamic response was collected and analyzed. This data was then utilized to develop accurate and efficient data-driven models for GFM inverters. The paper discussed the implementation of SysId algorithm method to capture the GFM inverter characteristics. Furthermore, the analytical approach to obtain the mathematical model of GFM inverter dynamics was also studied. The effectiveness of the data-driven models was cross-validated with analytical approach through simulation studies and experiment. GoF values for the analytical and data-driven approaches are determined to be 87.45% and 86.35%, respectively. Both approaches exhibit accuracy in capturing the dynamic response of GFM inverters across various load conditions.

7.2 Limitations

The scope of this dissertation was primarily focused on establishing the fundamental framework for a data-driven modeling technique applied to both GFL and GFM inverters, achieved through the system identification algorithm. There exists potential for broader exploration by integrating concepts from machine learning methodologies like clustering, deep learning, and ANN into the system identification algorithm. These techniques could unlock concealed patterns and intricate structures inherent in the data, offering a more comprehensive understanding of inverter behaviors.

Furthermore, it's important to note that the dynamic model derived from the system identification technique has not yet been practically implemented within a large CDPS. Implementing the model in a CDPS setting presents an avenue for future research, allowing for the assessment of its performance and effectiveness within the complex interactions and dynamics inherent in such systems. This highlights a potential future direction for expanding the applicability of the developed data-driven modeling approach. Moreover, Data-driven models heavily rely on the quality and representativeness of the training dataset. Insufficient or biased data may result in model limitations. While proficient in capturing observed patterns, data-driven models might face challenges in generalizing to extreme scenarios not well-represented in the training data.

The utilization of probing signals to extract system dynamics presents certain limitations that warrant consideration. Firstly, generating probing signals tailored to each mode of operation can be a demanding task, particularly in systems featuring numerous operational modes. This requirement can lead to increased resource allocation and time

investment, potentially complicating the experimental setup and modeling process. Additionally, the minimum and maximum resolution of the probing signal is contingent upon the specific region under investigation within the system. This resolution dependency introduces complexities when dealing with dynamic behaviors across different system regions. Moreover, the potential for model switching errors arises when rapid transitions occur between distinct dynamic events within a brief time-frame. This underscores the importance of meticulously timing the probing signal to align with the system's dynamics and account for abrupt shifts. Addressing these limitations entails careful planning and potential adjustments in experimental methodologies to ensure an accurate depiction of the system's intricate dynamics.

7.3 Future Work

In terms of future directions, there are several compelling avenues to explore in enhancing the current research. Firstly, the development of an adaptive approach for model switching could greatly enhance the versatility and accuracy of the proposed technique. Exploring methodologies like functional data analysis might enable the system to dynamically adapt its model selection based on real-time data, accommodating dynamic changes in system behavior and ensuring a seamless transition between different operational modes.

Furthermore, extending this approach to larger systems with a mix of inverters utilizing different control strategies holds significant potential. This expansion would require a more comprehensive understanding of how various control schemes interact within a complex system. Incorporating legacy inverters, which might employ different

control mechanisms, introduces additional complexity. This could potentially necessitate the consideration of multi-input multi-output systems to effectively capture the interdependencies between different components and their control strategies.

By venturing into these future avenues, the research could achieve a broader applicability and provide insights into the challenges and opportunities of implementing the proposed data-driven modeling approach within more intricate and diverse power system environments.

REFERENCES

[1] C. international des grands réseaux électriques. Comité d'études C4, *Modeling and dynamic behavior of wind generation as it relates to power system control and dynamic performance*. CIGRÉ, 2007.

[2] H. Holttinen, J. Kiviluoma, D. Flynn, *et al.*, "System impact studies for near 100% renewable energy systems dominated by inverter based variable generation," *IEEE Transactions on Power Systems*, pp. 1–1, 2020. DOI: 10.1109/TPWRS.2020.3034924.

[3] S. Peyghami, P. Palensky, and F. Blaabjerg, "An overview on the reliability of modern power electronic based power systems," *IEEE Open Journal of Power Electronics*, vol. 1, pp. 34–50, 2020. DOI: 10.1109/OJPEL.2020.2973926.

[4] *Key takeaways: Inverter-based resource performance and analysis workshop*.

[5] "Intricacies in pscad/emt analysis: A discussion of intricacies in emt simulation of power electronic controllers, which can lead to varying results and poor benchmark/comparisons," Tech. Rep.

[6] U. Tamrakar, D. Shrestha, M. Maharjan, B. P. Bhattarai, T. M. Hansen, and R. Tonkoski, "Virtual inertia: Current trends and future directions," *Applied Sciences*, vol. 7, no. 7, 2017, ISSN: 2076-3417. DOI: 10.3390/app7070654. [Online]. Available: https://www.mdpi.com/2076-3417/7/7/654.

[7] U. Markovic, O. Stanojev, E. Vrettos, P. Aristidou, and G. Hug, "Understanding stability of low-inertia systems," *engrXiv preprint*, 2019. DOI: https://doi.org/10.31224/osf.io/jwzrq.

[8] B. Kroposki, C. Pink, R. DeBlasio, H. Thomas, M. Simões, and P. K. Sen, "Benefits of power electronic interfaces for distributed energy systems," *IEEE Transactions on Energy Conversion*, vol. 25, no. 3, pp. 901–908, 2010. DOI: 10.1109/TEC.2010.2053975.

[9] B. Kroposki, B. Johnson, Y. Zhang, *et al.*, "Achieving a 100% renewable grid: Operating electric power systems with extremely high levels of variable renewable energy," *IEEE Power and Energy Magazine*, vol. 15, no. 2, pp. 61–73, 2017. DOI: 10.1109/MPE.2016.2637122.

[10] E. Muljadi, N. Samaan, V. Gevorgian, J. Li, and S. Pasupulati, "Different factors affecting short circuit behavior of a wind power plant," in *2010 IEEE Industry Applications Society Annual Meeting*, 2010, pp. 1–9. DOI: 10.1109/IAS.2010.5616819.

[11] D. Gautam and V. Vittal, "Impact of DFIG based wind turbine generators on transient and small signal stability of power systems," in *2009 IEEE Power Energy Society General Meeting*, 2009, pp. 1–6. DOI: 10.1109/PES.2009.5275847.

[12] G. Tsourakis, B. Nomikos, and C. Vournas, "Effect of wind parks with doubly fed asynchronous generators on small-signal stability," *Electric Power Systems Research*, vol. 79, no. 1, pp. 190 –200, 2009, ISSN: 0378-7796. DOI: https://doi.org/10.1016/j.epsr.2008.05.018. [Online]. Available: http://www.sciencedirect.com/science/article/pii/S0378779608001697.

[13] Power System Dynamic Performance Committee, "Stability definitions and characterization of dynamic behavior in systems with high penetration of power electronic interfaced technologies," Tech. Rep., 2020. [Online]. Available: https://resourcecenter.ieee-pes.org/publications/technical-reports/PES_TP_TR77_PSDP_stability_051320.html.

[14] M. Farrokhabadi, C. A. Cañizares, J. W. Simpson-Porco, *et al.*, "Microgrid stability definitions, analysis, and examples," *IEEE Transactions on Power Systems*, vol. 35, no. 1, pp. 13–29, 2020. DOI: 10.1109/TPWRS.2019.2925703.

[15] C. Yoon, H. Bai, R. N. Beres, X. Wang, C. L. Bak, and F. Blaabjerg, "Harmonic stability assessment for multiparalleled, grid-connected inverters," *IEEE Transactions on Sustainable Energy*, vol. 7, no. 4, pp. 1388–1397, 2016. DOI: 10.1109/TSTE.2016.2551737.

[16] E. Ebrahimzadeh, F. Blaabjerg, X. Wang, and C. L. Bak, "Modeling and identification of harmonic instability problems in wind farms," in *2016 IEEE Energy Conversion Congress and Exposition (ECCE)*, 2016, pp. 1–6. DOI: 10.1109/ECCE.2016.7855258.

[17] D. Wu, G. Li, M. Javadi, A. M. Malyscheff, M. Hong, and J. N. Jiang, "Assessing impact of renewable energy integration on system strength using site-dependent short circuit ratio," *IEEE Transactions on Sustainable Energy*, vol. 9, no. 3, pp. 1072–1080, 2018. DOI: 10.1109/TSTE.2017.2764871.

[18] G. San, W. Zhang, X. Guo, C. Hua, H. Xin, and F. Blaabjerg, "Large-disturbance stability for power-converter-dominated microgrid: A review," *Renewable and Sustainable Energy Reviews*, vol. 127, p. 109 859, 2020, ISSN: 1364-0321. DOI: https://doi.org/10.1016/j.rser.2020.109859. [Online]. Available: https://www.sciencedirect.com/science/article/pii/S1364032120301532.

[19] Y. Lin, J. H. Eto, B. B. Johnson, *et al.*, *Research roadmap on grid-forming inverters*, November 2020. [Online]. Available: https://www.nrel.gov/docs/fy21osti/73476.pdf.

[20] Australian Energy Market Operator, *BLACK SYSTEM SOUTH AUSTRALIA 28 SEPTEMBER 2016*, March 2017. [Online]. Available: https://www.aemo.com.au/-/media/Files/Electricity/NEM/Market_Notices_and_Events/Power_System_Incident_Reports/2017/Integrated-Final-Report-SA-Black-System-28-September-2016.pdf.

[21] North American Electric Reliability Corporation (NERC), *900 MW Fault Induced Solar Photovoltaic Resource Interruption Disturbance Report*, February 2018. [Online]. Available: https://www.nerc.com/pa/rrm/ea/October%209%202017%20Canyon%202%20Fire%20Disturbance%20Report/900%20MW%20Solar%20Photovoltaic%20Resource%20Interruption%20Disturbance%20Report.pdf.

[22] Z. Jankovic, B. Novakovic, V. Bhavaraju, and A. Nasiri, "Average modeling of a three-phase inverter for integration in a microgrid," in *2014 IEEE Energy Conversion Congress and Exposition (ECCE)*, 2014, pp. 793–799.

[23] D. Maksimovic, A. M. Stankovic, V. Joseph Thottuvelil, and G. C. Verghese, "Modeling and Simulation of Power Electronic Converters," *Proceedings of the IEEE*, vol. 89, no. 6, pp. 898–912, 2001, ISSN: 00189219. DOI: 10.1109/5.931486.

[24] National Renewable Energy Laboratory, "Simulating distributed energy resource responses to transmission system-level faults considering IEEE 1547 performance categories on three major WECC transmission paths," Tech. Rep., Feb. 2020. [Online]. Available: https://www.nrel.gov/docs/fy20osti/73071.pdf.

[25] Electric Power Research Institute, "The new aggregated distributed energy resources (DER˙A) model for transmission planning studies: 2019 update," Tech. Rep. 3002015320, Mar. 2019.

[26] D. Ramasubramanian, Z. Yu, R. Ayyanar, V. Vittal, and J. Undrill, "Converter model for representing converter interfaced generation in large scale grid simulations," *IEEE Transactions on Power Systems*, vol. 32, no. 1, pp. 765–773, 2017. DOI: 10.1109/TPWRS.2016.2551223.

[27] D. Ramasubramanian, E. Farantatos, S. Ziaeinejad, and A. Mehrizi-Sani, "Operation paradigm of an all converter interfaced generation bulk power system," *IET Generation, Transmission Distribution*, vol. 12, no. 19, pp. 4240–4248, 2018. DOI: 10.1049/iet-gtd.2018.5179.

[28] M. Paolone, T. Gaunt, X. Guillaud, *et al.*, "Fundamentals of power systems modelling in the presence of converter-interfaced generation," *Electric Power Systems Research*, vol. 189, p. 106 811, 2020, ISSN: 0378-7796. DOI: https://doi.org/10.1016/j.epsr.2020.106811. [Online]. Available: http://www.sciencedirect.com/science/article/pii/S037877962030482X.

[29] Y. Wu, Y. Wu, J. M. Guerrero, J. C. Vasquez, and J. Li, "AC Microgrid Small-Signal Modeling: Hierarchical Control Structure Challenges and Solutions," *IEEE Electrification Magazine*, vol. 7, pp. 81–88, 2019.

[30] H. Abbood and A. Benigni, "Data-driven modeling of a commercial photovoltaic microinverter," *Modelling and Simulation in Engineering*, pp. 1–11, 2018. DOI: 10.1155/2018/5280681.

[31] C. Shah, J. D. Vasquez-Plaza, D. D. Campo-Ossa, *et al.*, "Review of dynamic and transient modeling of power electronic converters for converter dominated power systems," *IEEE Access*, vol. 9, pp. 82 094–82 117, 2021. DOI: 10.1109/ACCESS.2021.3086420.

[32] A. F. Hoke, M. Shirazi, S. Chakraborty, E. Muljadi, and D. Maksimovic, "Rapid active power control of photovoltaic systems for grid frequency support," *IEEE Journal of Emerging and Selected Topics in Power Electronics*, vol. 5, no. 3, pp. 1154–1163, 2017. DOI: 10.1109/JESTPE.2017.2669299.

[33] K. Prabakar, M. Shirazi, A. Singh, and S. Chakraborty, "Advanced photovoltaic inverter control development and validation in a controller-hardware-in-the-loop test bed," in *2017 IEEE Energy Conversion Congress and Exposition (ECCE)*, 2017, pp. 1673–1679. DOI: 10.1109/ECCE.2017.8095994.

[34] J. F. Patarroyo-Montenegro, F. Andrade, J. M. Guerrero, and J. C. Vasquez, "A linear quadratic regulator with optimal reference tracking for three-phase inverter-based islanded microgrids," *IEEE Transactions on Power Electronics*, vol. 36, no. 6, pp. 7112–7122, 2021. DOI: 10.1109/TPEL.2020.3036594.

[35] F. Guinjoan, J. Calvente, A. Poveda, and L. Martinez, "Large signal modeling and simulation of switching DC-DC converters," *IEEE Transactions on Power Electronics*, vol. 12, no. 3, pp. 485–494, 1997.

[36] G. Nirgude, R. Tirumala, and N. Mohan, "A new, large-signal average model for single-switch DC-DC converters operating in both CCM and DCM," in *2001 IEEE 32nd Annual Power Electronics Specialists Conference (IEEE Cat. No.01CH37230)*, vol. 3, 2001, pp. 1736–1741. DOI: 10.1109/PESC.2001.954370.

[37] V. M. Canalli, J. A. Cobos, J. A. Oliver, and J. Uceda, "Behavioral large signal averaged model for DC/DC switching power converters," in *PESC Record. 27th Annual IEEE Power Electronics Specialists Conference*, vol. 2, 1996, pp. 1675–1681. DOI: 10.1109/PESC.1996.548806.

[38] F. Tahami and H. M. Ahmadian, "Piecewise affine large signal modeling of PFC rectifiers," in *2007 IEEE International Symposium on Industrial Electronics*, 2007, pp. 3362–3366. DOI: 10.1109/ISIE.2007.4375155.

[39] E. Muljadi, M. Singh, and V. Gevorgian, "User guide for PV dynamic model simulation written on PSCAD platform," National Renewable Energy Laboratory, Tech. Rep. NREL Technical Report no. TP-5D00-62053, 2014.

[40] W. Jianhua, Z. Fanghua, G. Chunying, and C. Ran, "Modelling and analysis of a buck/boost bidirectional converter with developed switch model," in *8th IEEE International Conference on Power Electronics - ECCE Asia*, Jeju, South Korea, 2011. DOI: 10.1109/ICPE.2011.5944647.

[41] CIGRE Joint Working Group C4/C6.35/CIRED, "Modeling of Inverter-Based Generation for Power System Dynamic Studies," Tech. Rep., 2018.

[42] M. Farrokhabadi, S. König, C. A. Cañizares, K. Bhattacharya, and T. Leibfried, "Battery energy storage system models for microgrid stability analysis and dynamic simulation," *IEEE Transactions on Power Systems*, vol. 33, no. 2, pp. 2301–2312, 2018. DOI: 10.1109/TPWRS.2017.2740163.

[43] A. Isaacs and G. Irwin, "Recommended PSCAD Model Requirements Rev. 5," Electranix, Tech. Rep., 2018.

[44] J. Wang, B. Ji, T. Wu, and J. Chen, "Modelling and analysis of a single phase inverter system with PWM switch model," in *40th Annual Conference of the IEEE Industrial Electronics Society (IECON2014)*, Dallas, TX, USA, Oct. 2014. DOI: 10.1109/IECON.2014.7049278.

[45] A. Yazdani and R. Iravani, *Voltage-sourced converters in power systems: modeling, control, and applications*. Wiley-IEEE Press, 2010.

[46] G. N. Love and A. R. Wood, "Small signal model of a power electronic converter," *8th International Power Engineering Conference, IPEC 2007*, pp. 636–642, 2007.

[47] H. Xu, *Modeling and large signal stability analysis of a DC/AC microgrid*, 2018.

[48] North American Reliability Council, "Standard models for variable generation," Tech. Rep., May 2010. [Online]. Available: https://www.nerc.com/docs/pc/ivgtf/IVGTF_Report_PhaseII_Task1-1_Final(5.24).pdf.

[49] N. Hatziargyriou, J. V. Milanovic, C. Rahmann, *et al.*, "Definition and classification of power system stability revisited extended," *IEEE Transactions on Power Systems*, pp. 1–1, 2020. DOI: 10.1109/TPWRS.2020.3041774.

[50] P. Kundur, N. J. Balu, and M. G. Lauby, *Power system stability and control*. McGraw-Hill New York, 1994, vol. 7.

[51] Western Electricity Coordinating Council, *WECC approved dynamic model library*, 2018. [Online]. Available: https://www.wecc.org/Reliability/WECCApprovedDynamicModelsLibraryMay2018.pdf.

[52] P. Sørensen, B. Andresen, J. Fortmann, and P. Pourbeik, "Modular structure of wind turbine models in iec 61400-27-1," in *2013 IEEE Power & Energy Society General Meeting*, IEEE, 2013, pp. 1–5.

[53] P. Pourbeik, "Specification of the second generation generic models for wind turbine generators," *Electric Power Research Institute, Report*, 2013.

[54] A. Ellis, P. Pourbeik, J. J. Sanchez-Gasca, J. Senthil, and J. Weber, "Generic wind turbine generator models for WECC - a second status report," in *2015 IEEE Power Energy Society General Meeting*, Jun. 2015, pp. 1–5. DOI: 10.1109/PESGM.2015.7285645.

[55] P. Pourbeik, J. J. Sanchez-Gasca, J. Senthil, *et al.*, "Generic dynamic models for modeling wind power plants and other renewable technologies in large-scale power system studies," *IEEE Transactions on Energy Conversion*, vol. 32, no. 3, pp. 1108–1116, Sep. 2017, ISSN: 0885-8969. DOI: 10.1109/TEC.2016.2639050.

[56] Intermittent Variable Generation Taskforce, "Accommodating high levels of variable generation," North American Electric Reliability Corp.(NERC), Tech. Rep., 2009.

[57] M Sultan, J Reeve, and R Adapa, "Combined transient and dynamic analysis of HVDC and FACTS systems," *IEEE Transactions on Power Delivery*, vol. 13, no. 4, pp. 1271–1277, 1998.

[58] Q. Huang and V. Vittal, "Advanced EMT and phasor-domain hybrid simulation with simulation mode switching capability for transmission and distribution systems," *IEEE Transactions on Power Systems*, vol. 33, no. 6, pp. 6298–6308, 2018.

[59] A. A. van der Meer, M. Gibescu, M. A. van der Meijden, W. L. Kling, and J. A. Ferreira, "Advanced hybrid transient stability and emt simulation for VSC-HVDC systems," *IEEE Transactions on Power Delivery*, vol. 30, no. 3, pp. 1057–1066, 2014.

[60] A. M. Stankovic, B. C. Lesieutre, and T. Aydin, "Modeling and analysis of single-phase induction machines with dynamic phasors," *IEEE Transactions on Power Systems*, vol. 14, no. 1, pp. 9–14, 1999.

[61] Y. Liu, V. Vittal, J. Undrill, and J. H. Eto, "Transient model of air-conditioner compressor single phase induction motor," *IEEE Transactions on Power Systems*, vol. 28, no. 4, pp. 4528–4536, 2013.

[62] C. Sakinci and J. Beerten, "Generalized dynamic phasor modeling of the mmc for small-signal stability analysis," *IEEE Transactions on Power Delivery*, vol. 34, no. 3, pp. 991–1000, 2019. DOI: 10.1109/TPWRD.2019.2898468.

[63] D. Solomatine and A. Ostfeld, "Data-driven modelling: Some past experiences and new approaches," *Journal of Hydroinformatics - J HYDROINFORM*, vol. 10, Jan. 2008. DOI: 10.2166/hydro.2008.015.

[64] A. Alqahtani, M. Alsaffar, M. El-Sayed, and B. Alajmi, "Data-driven photovoltaic system modeling based on nonlinear system identification," *International Journal of Photoenergy*, vol. 2016, p. 2 923 731, Jun. 2016, ISSN: 1110-662X. DOI: 10.1155/2016/2923731. [Online]. Available: https://doi.org/10.1155/2016/2923731.

[65] J. Sjöberg, Q. Zhang, L. Ljung, *et al.*, "Nonlinear black-box modeling in system identification: A unified overview," *Automatica*, vol. 31, no. 12, pp. 1691 –1724, 1995, Trends in System Identification, ISSN: 0005-1098. DOI: https://doi.org/10.1016/0005-1098(95)00120-8. [Online]. Available: http://www.sciencedirect.com/science/article/pii/0005109895001208.

[66] F. Rojas, M. Suriyah, and T. Leibfried, "A review of converter control concepts for improving power system frequency stability: A path to 100% converter based generation," in *2019 IEEE Power Energy Society Innovative Smart Grid Technologies Conference (ISGT)*, 2019, pp. 1–5. DOI: 10.1109/ISGT.2019.8791561.

[67] "IEEE standard for interconnection and interoperability of distributed energy resources with associated electric power systems interfaces," IEEE Std. 1547-2018 (Revision of IEEE Std 1547-2003), Tech. Rep., Mar. 2018.

[68] J. Johnson, A. Summers, R. Darbali-Zamora, *et al.*, "Distribution Voltage Regulation Using Extremum Seeking Control with Power Hardware-in-the-Loop," *IEEE Journal of Photovoltaics*, vol. 8, no. 6, pp. 1824–1832, 2018.

[69] N. Ninad, E. Apablaza- Arancibia, J. Rajda, and D. Turcotte, "Laboratory Assessment of DER Inverter Grid Support Functions for Updated Canadian CSA C22.3 No.9 Interconnection Standard," in *IEEE Electrical Power and Energy Conference (EPEC)*, 2019, pp. 1–6.

[70] A. V. Timbus, M. Ciobotaru, R. Teodorescu, and F. Blaabjerg, "Adaptive Resonant Controller for Grid-connected Converters in Distributed Power Generation Systems," in 25^{th} *IEEE Applied Power Electronics Conference and Exposition*, 2006, 6 pp.

[71] M. Shcherbakov, A. Brebels, N. Shcherbakova, A. Tyukov, T. Janovsky, and V. Kamaev, "A Survey of Forecast Error Measures," *World Applied Sciences Journal*, vol. 24, pp. 171–176, Jan. 2013. DOI: 10.5829/idosi.wasj.2013.24.itmies.80032.

[72] A. H. Tan and K. R. Godfrey, *Industrial Process Identification—Perturbation Signal Design and Applications*. Springer Nature: Basel, Switzerland, 2019.

[73] V. Valdivia, A. Lazaro, A. Barrado, P. Zumel, C. Fernandez, and M. Sanz, "Black-box modeling of three-phase voltage source inverters for system-level analysis," *IEEE Transactions on Industrial Electronics*, vol. 59, no. 9, pp. 3648–3662, Oct. 2012. DOI: 10.1109/TIE.2011.2167730.

[74] L. Ljung, "System Identification: Theory for the User, 2nd ed.," *Prentice Hall*, 1999.

[75] "System identification toolbox." (), [Online]. Available: https://www.mathworks.com/help/ident/ref/compare.html (visited on 10/31/2019).

[76] "System identification toolbox." (), [Online]. Available: https://www.mathworks.com/help/ident/ref/fpe.html (visited on 10/31/2019).

[77] O. Nelles, *Nonlinear system identification: From classical approaches to neural networks, fuzzy models and Gaussian processes*. Springer, 2021.

[78] N. Guruwacharya, N. Bhujel, T. M. Hansen, *et al.*, "Modeling inverters with grid support functions for power system dynamics studies," in *2021 IEEE Power Energy Society Innovative Smart Grid Technologies Conference (ISGT)*, 2021, pp. 1–5. DOI: 10.1109/ISGT49243.2021.9372183.

[79] *Time domain specifications*. [Online]. Available: https://www.tutorialspoint.com/control_systems/control_systems_time_domain_specifications.htm.

[80] A. Novak, L. Simon, F. Kadlec, and P. Lotton, "Nonlinear system identification using exponential swept-sine signal," *IEEE Transactions on Instrumentation and Measurement*, vol. 59, pp. 2220–2229, Oct. 2009. DOI: 10.1109/TIM.2009.2031836.

[81] R. Chakraborty, H. Jain, and G.-S. Seo, "A review of active probing-based system identification techniques with applications in power systems," *International Journal of Electrical Power & Energy Systems*,

[82] N. Guruwacharya, N. Bhujel, U. Tamrakar, *et al.*, "Data-driven power electronic converter modeling for low inertia power system dynamic studies," in *2020 IEEE Power Energy Society General Meeting (PESGM)*, 2020, pp. 1–5. DOI: 10.1109/PESGM41954.2020.9281783.

[83] S. Subedi, M. Rauniyar, S. Ishaq, *et al.*, "Review of methods to accelerate electromagnetic transient simulation of power systems," *IEEE Access*, vol. 9, pp. 89 714–89 731, 2021. DOI: 10.1109/ACCESS.2021.3090320.

[84] V. Muthukrishnan, *How to find the dc gain of a transfer function (examples included)*, Feb. 2021. [Online]. Available: https://www.electrical4u.com/dc-gain-transfer-function/.

[85] R. H. Byrne, T. A. Nguyen, D. A. Copp, B. R. Chalamala, and I. Gyuk, "Energy management and optimization methods for grid energy storage systems," *IEEE Access*, vol. 6, pp. 13 231–13 260, 2018. DOI: 10.1109/ACCESS.2017.2741578.

[86] G. Venkataramanan and Bingsen Wang, "Dynamic modeling and control of three phase pulse width modulated power converters using phasors," in *IEEE* 35^{th} *Annual Power Electronics Specialists Conference*, Jun. 2004, pp. 2822–2828. DOI: 10.1109/PESC.2004.1355281.

[87] F. Milano, F. Dörfler, G. Hug, D. J. Hill, and G. Verbič, "Foundations and challenges of low-inertia systems (invited paper)," in *2018 Power Systems Computation Conference (PSCC)*, 2018, pp. 1–25. DOI: 10.23919/PSCC.2018.8450880.

[88] X. Wang, M. G. Taul, H. Wu, Y. Liao, F. Blaabjerg, and L. Harnefors, "Grid-synchronization stability of converter-based resources—an overview," *IEEE Open Journal of Industry Applications*, vol. 1, pp. 115–134, 2020. DOI: 10.1109/OJIA.2020.3020392.

[89] S. Chung, "A phase tracking system for three phase utility interface inverters," *IEEE Transactions on Power Electronics*, vol. 15, no. 3, pp. 431–438, 2000. DOI: 10.1109/63.844502.

[90] Y. Li, Y. Gu, Y. Zhu, A. Junyent-Ferré, X. Xiang, and T. C. Green, "Impedance circuit model of grid-forming inverter: Visualizing control algorithms as circuit elements," *IEEE Transactions on Power Electronics*, vol. 36, no. 3, pp. 3377–3395, 2021. DOI: 10.1109/TPEL.2020.3015158.

[91] S. D'Arco and J. A. Suul, "Equivalence of virtual synchronous machines and frequency-droops for converter-based microgrids," *IEEE Transactions on Smart Grid*, vol. 5, no. 1, pp. 394–395, 2014. DOI: 10.1109/TSG.2013.2288000.

[92] R. Rosso, X. Wang, M. Liserre, X. Lu, and S. Engelken, "Grid-forming converters: Control approaches, grid-synchronization, and future trends—a review," *IEEE Open Journal of Industry Applications*, vol. 2, pp. 93–109, 2021. DOI: 10.1109/OJIA.2021.3074028.

[93] S. Fazal, M. E. Haque, M. T. Arif, and A. Gargoom, "Droop control techniques for grid forming inverter," in *2022 IEEE PES 14th Asia-Pacific Power and Energy Engineering Conference (APPEEC)*, 2022, pp. 1–6. DOI: 10.1109/APPEEC53445.2022.10072251.

[94] M. Chandorkar, D. Divan, and R. Adapa, "Control of parallel connected inverters in standalone ac supply systems," *IEEE Transactions on Industry Applications*, vol. 29, no. 1, pp. 136–143, 1993. DOI: 10.1109/28.195899.

[95] P. R. Chowdhury, E. Shoubaki, and M. Manjrekar, "Modified voltage controlled-virtual synchronous machine controller in the application of parallel connected grid-forming inverters," in *2021 IEEE 12th International Symposium on Power Electronics for Distributed Generation Systems (PEDG)*, 2021, pp. 1–5. DOI: 10.1109/PEDG51384.2021.9494260.

[96] H.-P. Beck and R. Hesse, "Virtual synchronous machine," *2007 9th International Conference on Electrical Power Quality and Utilisation*, pp. 1–6, 2007.

[97] Q.-C. Zhong, "Virtual synchronous machines: A unified interface for grid integration," *IEEE Power Electronics Magazine*, vol. 3, no. 4, pp. 18–27, 2016. DOI: 10.1109/MPEL.2016.2614906.

[98] B. B. Johnson, M. Sinha, N. G. Ainsworth, F. Dörfler, and S. V. Dhople, "Synthesizing virtual oscillators to control islanded inverters," *IEEE Transactions on Power Electronics*, vol. 31, no. 8, pp. 6002–6015, 2016. DOI: 10.1109/TPEL.2015.2497217.

[99] M. Lu, "Virtual oscillator grid-forming inverters: State of the art, modeling, and stability," *IEEE Transactions on Power Electronics*, vol. 37, no. 10, pp. 11 579–11 591, 2022. DOI: 10.1109/TPEL.2022.3163377.

[100] Y. Bae, T.-K. Vu, and R.-Y. Kim, "Implemental Control Strategy for Grid Stabilization of Grid-Connected PV System Based on German Grid Code in Symmetrical Low-to-Medium Voltage Network," *IEEE Transactions on Energy Conversion*, vol. 28, no. 3, pp. 619–631, 2013. DOI: 10.1109/TEC.2013.2263885.

[101] B. Wen, D. Boroyevich, R. Burgos, P. Mattavelli, and Z. Shen, "Analysis of d-q small-signal impedance of grid-tied inverters," *IEEE Transactions on Power Electronics*, vol. 31, no. 1, pp. 675–687, 2016. DOI: 10.1109/TPEL.2015.2398192.

[102] D. Dong, B. Wen, D. Boroyevich, P. Mattavelli, and Y. Xue, "Analysis of phase-locked loop low-frequency stability in three-phase grid-connected power converters considering impedance interactions," *IEEE Transactions on Industrial Electronics*, vol. 62, no. 1, pp. 310–321, 2015. DOI: 10.1109/TIE.2014.2334665.

[103] J. Matevosyan, B. Badrzadeh, T. Prevost, *et al.*, "Grid-forming inverters: Are they the key for high renewable penetration?" *IEEE Power and Energy Magazine*, vol. 17, no. 6, pp. 89–98, 2019. DOI: 10.1109/MPE.2019.2933072.

[104] G. Guarderas, A. Frances, R. Asensi, and J. Uceda, "Blackbox Large-Signal Modeling of Grid-Connected DC-AC Electronic Power Converters," *Energies*, vol. 12, no. 6, 2019. DOI: 10.3390/en12060989.

[105] N. Guruwacharya, N. Bhujel, T. M. Hansen, *et al.*, "Modeling inverters with grid support functions for power system dynamics studies," in *2021 IEEE Power Energy Society Innovative Smart Grid Technologies Conference (ISGT)*, 2021, pp. 1–5. DOI: 10.1109/ISGT49243.2021.9372183.

[106] H. Abbood and A. Benigni, "Data-driven modeling of a commercial photovoltaic microinverter," *Modelling and Simulation in Engineering*, pp. 1–11, 2018. DOI: 10.1155/2018/5280681.

[107] V. Valdivia, A. Lázaro, A. Barrado, P. Zumel, C. Fernández, and M. Sanz, "Black-box modeling of three phase voltage source inverters based on transient response analysis," in *2010 Twenty-Fifth Annual IEEE Applied Power Electronics Conference and Exposition (APEC)*, Feb. 2010, pp. 1279–1286. DOI: 10.1109/APEC.2010.5433336.

[108] N. Guruwacharya, N. Bhujel, U. Tamrakar, *et al.*, "Data-driven power electronic converter modeling for low inertia power system dynamic studies," in *2020 IEEE Power Energy Society General Meeting (PESGM)*, 2020, pp. 1–5. DOI: 10.1109/PESGM41954.2020.9281783.

[109] N. Guruwacharya, H. Bhandari, S. Subedi, *et al.*, "Data-driven modeling of commercial photovoltaic inverter dynamics using power hardware-in-the-loop," in *2022 International Symposium on Power Electronics, Electrical Drives, Automation and Motion (SPEEDAM)*, 2022, pp. 924–929. DOI: 10.1109/SPEEDAM53979.2022.9842001.

[110] A. Yazdani and R. Iravani, *Voltage-sourced converters in power systems: modeling, control, and applications*. John Wiley & Sons, 2010.

[111] M. Rasheduzzaman, J. A. Mueller, and J. W. Kimball, "An accurate small-signal model of inverter-dominated islanded microgrids using *dq* reference frame," *IEEE Journal of Emerging and Selected Topics in Power Electronics*, vol. 2, no. 4, pp. 1070–1080, 2014.